POLITECNICO DI MILANO
DEPARTMENT AEROSPACE SCIENCE AND TECHNOLOGY
DOCTORAL PROGRAM IN AEROSPACE ENGINEERING

NON-IDEAL COMPRESSIBLE FLUID THERMODYNAMICS OF MIXTURES: MEASUREMENTS AND MODELING

Doctoral Dissertation of:
Luuc Keulen

Supervisor:
Prof. A. Guardone

Co-supervisor:
Prof. A. Spinelli

Co-supervisor:
Dr. E. Mansfield

Tutor:
Prof. M. Quadrio

The Chair of the Doctoral Program:
Prof. L. Vigevano

2018 – XXX

Dedicated to my father

SUMMARY

Many processes operate with working fluids made of multiple components in multiple phases (e.g. chemical reactions, distillation, thermodynamic power cycles, refrigeration cycles and heat pump cycles). To improve the design of process equipment and increase the uptake of environmentally friendly fluids, a solid understanding of mixture properties is necessary. The choice of the working fluid is driven by different requirements arising from the specific application. A great variety of substances, with different thermo-physical properties, are used in industry for various applications. These fluids range from simple fluids to heavy fluids formed by complex molecules. Among the fields where mixtures can possibly increase the efficiency are power cycles for sustainable energy conversion, an example is the organic Rankin cycle (ORC). Many of these power cycles for sustainable energy conversion operate in the non-ideal thermodynamic region, close to the liquid-vapor saturation curve and the critical point, where the actual thermodynamic behavior of gases can deviate significantly from that predicted by the ideal gas law. The understanding of non-ideal compressible fluid thermodynamics of mixtures will enable to improve existing industrial processes and machinery for ORCs. The scientific interest is not only limited to ORCs or other power cycles operating with organic substances. The scientific interest extends to a wide range of application where fluids and mixtures operate in the non-ideal thermodynamic region.

This work presents original research in the field of non-ideal compressible fluid thermodynamics of mixtures. The study is focused on mixtures of fluids with high molecular complexity, these are complex siloxanes currently used as heat transfer fluids and in ORCs and perfluorocarbons. The presented work is concentrated in three directions and aims to (i) gain more knowledge of the non-ideal thermodynamic behavior of mixtures composed of molecular complex fluids in the non-ideal gas region, (ii) the development of accurate thermodynamic models for mixtures of linear siloxanes, (iii) and determine the thermal stability and decomposition products of linear siloxanes. A better understanding of these aspects can improve the study of gasdynamic phenomena and the use of mixtures in experiments and industrial applications.

In the first part a fundamental research on the speed of sound behavior for binary mixtures of molecular complex fluids (e.g. linear siloxanes and perfluorocarbons) in the non-ideal thermodynamic region is conducted. The speed of sound behavior is

qualitatively investigated using the polytropic van der Waals model and verified using the Helmholtz energy equation of state. Non-monotonic behavior of the speed of sound is observed upon varying the composition of the mixture. The non-monotonic behavior of the speed of sound is more evident if the molecular complexity of each pure components of the mixture differ. This non-monotonic behavior is caused by the interaction between the different components in the mixture.

In the second part measurements are performed to determine the bubble-point pressures for three binary mixtures of linear siloxanes: MM with MDM, MD_2M, and MD_3M. Large uncertainties are observed for the lowest temperatures, an extensive analysis of the uncertainties is conducted and concludes that these large uncertainties are mostly caused by the effect of impurities of non-condensable gases. For each binary mixture new binary interaction parameters are fitted for the multi-fluid Helmholtz energy model using the obtained bubble-point pressure data.

To conclude, an experimental test-rig is designed and commissioned for the determination of the thermal stability limit and decomposition products of pure fluids and mixtures. An expected feature of mixtures of siloxanes is that they exhibit a higher thermal stability limit than their pure components, due to the redistribution process occurring at high temperature, where more complex molecules decompose into simpler molecules, which then recombine again into the more complex molecule. This redistribution and therefore the possible increase of the thermal stability temperature can enhance the use of complex molecular fluids for experimental and industrial applications. The thermal stability limit is determined for the pure linear siloxanes MM and MDM. For both fluids minimal decomposition products are observed using chemical analysis of the liquid and vapor phase. Though formation of other linear and cyclic siloxanes as decomposition products are observed as well as volatile gases in the vapor phase.

TABLE OF CONTENTS

CHAPTER 1

INTRODUCTION

1.1 Introduction

Global energy consumption has increased significantly over the last decades, due to growing industrialization and higher personal demand [1]. Fossil fuels currently provide 80% of the world's primary energy production [1], with coal playing a major role due to its easy accessibility and low cost. Despite regulations and limitation introduced by governments on the use of fossil fuels, their use is expected to increase and continue to meet much of world's energy demand [2].

The most serious threat caused by the use of fossil fuels is the emission of green house gases to the atmosphere. From 1970 to 2010 the total anthropogenic green house gas emission increased by 80% as reported by the the Intergovernmental Panel on Climate Change [3]. The largest share of the green house gas emission consist of carbon-dioxide (CO_2). The total emission of CO_2 increased drastically in the last century [4]. The main drivers for this increase in CO_2 emission are economic and population growth. Although the CO_2 emission will grow at a slower rate, the world CO_2 emission is projected to grow an average of 0.6% per year between 2015 and 2040 [2]. This increase in green house gases leads to many serious environmental problems such as climate change, air pollution and ozone layer depletion [3, 5, 6]. It is clear that the current situation cannot be sustained indefinitely and changes must be undertaken in order to reduce or divest from the emission of green house gases and improve the efficiency in which the energy sources are being used. As a consequence, energy savings, efficiency improvement and sustainability gain a wider level of interest.

An important focus to improve efficiency and sustainability is the choice of working fluids. Many fluid processes operate with working fluids made of multiple components in multiple phases (e.g. chemical reactions, distillation, thermodynamic power cycles, refrigeration cycles and heat pump cycles) [7, 8]. To improve the design of process equipment and increase the uptake of environmentally friendly fluids, a solid understanding of mixture properties is necessary. Better understanding of these properties can lead to significant improvement of the energy efficiency and decrease of environmental damage.

The choice of the working fluid is driven by different requirements arising from the specific application. A great variety of substances, with different thermo-physical properties, are used in industry, ranging from the simple fluids to the heavy fluids formed by complex molecules for various applications. Among the fields where mixtures can increase the efficiency are power cycles for sustainable energy conversion. It is more interesting and profitable to exploit energy sources such as low or medium temperature geothermal sources, biomass, solar energy, heat recovery from stationary engines for electricity production, and the recovery of waste energy from industrial facilities. Because of the relatively low level of temperature and sensible heat of the heat source in diverse low-temperature renewable energy power systems, it is not convenient to use the traditional plants with water vapor. These power systems for

sustainable energy conversion are based on innovative thermodynamic cycles, having the working fluid operating in the near critical region and close to the saturation curve.

An example is the organic Rankine cycle (ORC) [9]. Power cycles based on Rankine Cycle using water as working fluid are traditionally used in large power plants [9]. Due to the growing attention to energy efficiency and environmental issues, the ORC technology is now widely used for small to medium scale power generation. ORCs are applied to convert low/medium temperature heat sources (less than 500 °C) and small/medium power plants (up to 3 MW) [10]. For these applications the use of fluids (e.g. organic substances) with high molecular mass and complexity can be a better option with respect to water. The advantage of using organic compounds lies in the design and construction of the power plants, which are simpler and cheaper than steam Rankine Cycle plants for the small to medium power range [11]. They are used for many different applications were low to medium temperature energy sources are available, from industrial waste heat recovery to renewable energy applications, such as solar, biomass and geothermal energy [12–16]. The main feature of ORCs is the use of organic substances (e.g. hydrocarbons, perfluorocarbons or siloxanes) which allows the ability to choose the optimal working fluid depending on the operating temperature and power demand [17–19]. Other power cycle alternatives for sustainable energy conversion are the super- and transcritical CO_2 cycles [20–25], and Organic Stirling cycles [26, 27].

The advantage is that these cycles operate at different thermodynamic conditions, close to or above the critical point or in the non-ideal compressible fluid region. Another advantage is that these cycles can operate with various working fluids and are suitable for the use of mixtures. The use of a mixture instead of pure compound as working fluid can significantly improve the efficiency of the cycle [7, 8], this is elaborated in more detail in Section 1.2. The use of mixtures in refrigerant systems and heat pumps have been widely studied in the past few decades [28, 29]. The interest in the use of mixtures in power cycles has increased in recent years; a detailed review about the use of mixtures as working fluid in power generation systems is given by Modi et al. [30] and a specific review for ORCs by Abadi et al. [31].

These characteristics, operating at different thermodynamic conditions and the use of various working fluids, offer advantages such as expansion across a limited number of turbine stages, reduced compression work and a better match between the heating and cooling trajectory with the working fluid. The use of mixtures may also allow for modifying, in a virtually continuous way, the thermo-physical properties of the working fluid by changing the composition of the mixture, so to match the application requirements. A brief overview for the use of mixtures in power cycles is given in Section 1.2. Furthermore, these cycles could potentially allow for the exploitation of non-classical gasdynamic phenomena, as demonstrated for ORC by Brown et al. [32] and for high temperature heat pumps by Zamfirescu et al. [33]. More details about non-classical gasdynamic phenomena are given in Section 1.3. A

major problem that limits the use of these applications is lack of knowledge on the thermo-physical properties of diverse organic fluids in the thermodynamic regions of interest, where there are strong non-ideal effects. Also the thermal stability of the working fluid, which affect the maximum operating temperature, is among the physical characteristics with fundamental importance.

The most challenging aspect for the design of power cycles operating in or near the non-ideal compressible fluid region (e.g. ORC) is the fluid dynamic design of efficient turbo machinery components, namely the compressor and turbine. The design and performance assessment of (turbo-)expanders is usually based on the ideal-gas law to describe the fluids thermodynamic properties. This choice roots in the assumption that the deviation of the real thermodynamic behavior from ideal-gas behavior is small, which would result in equally small deviations in the predicted flow field and calculated performance parameters. In ORC applications, (turbo-)expanders are often operated at pressure and temperature close to their liquid-vapor critical-point values. This is the so-called non-ideal compressible fluid thermodynamic region, close to the liquid-vapor saturation line and to the critical point, where the actual thermodynamic behavior of gases can deviate significantly from that predicted by the ideal gas law. These deviations, in turn, lead to departure of fluid dynamic quantities from their ideal-gas counterparts, which are termed non-ideal compressible fluid effects, more details are given in Section 1.3. More complex thermodynamic models must be used to complement the fluid dynamics analysis of a non-ideal compressible fluid process. Non-ideal fluid flows received attention only recently from the scientific community, as is shown by the literature available on this topic [34–39]. For mixtures the research on non-ideal effects is even more limited where the only literature available is done by Colonna et al. [40] and Guardone et al. [41].

The understanding of non-ideal compressible fluid thermodynamics of mixtures will enable improved industrial processes and machinery for ORCs. Besides the academic interests related to the improvement of thermodynamic models and a better understanding of the non-ideal behavior of mixtures, the scientific interest is not limited to ORC or other power cycles operating with organic substances. Examples of applications that may benefit from a better understanding of non-ideal compressible thermodynamics of mixtures are applications in which fluid dynamic processes occur in highly non-ideal thermodynamic regions, such as refrigerant and heat pump cycles, pharmaceutical processes in which the flow at the exit of nozzles in supercritical conditions is used to nucleate pharmaceutical components [42], transportation of high-pressure fuels and chemicals [43], in transonic and hypersonic wind tunnels operating in the non-ideal compressible fluid regime [44], and the use of mixtures with CO_2 within supercritical Brayton cycles [25, 45].

This work presents original research in the field of non-ideal compressible fluid thermodynamics of mixtures. The study is focused on mixtures of fluids with high molecular complexity, such as complex siloxanes currently used as heat transfer fluids and in ORCs, and perfluorocarbons. Modern thermodynamic models indicate that

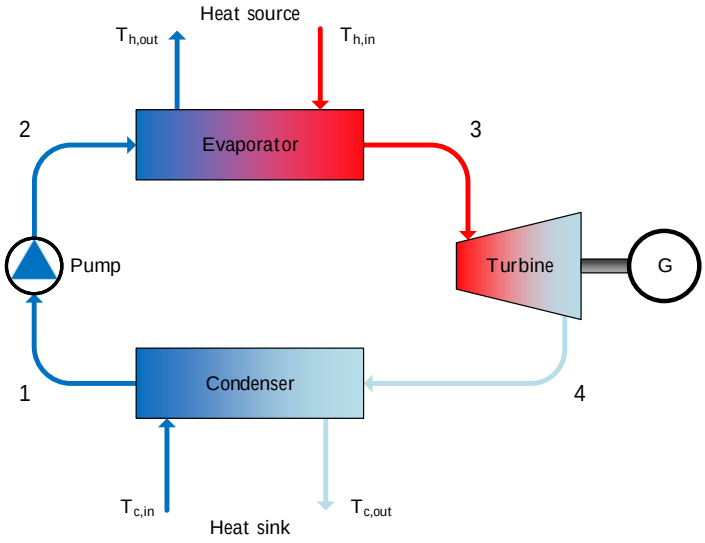

Figure 1.1: Schematic design of an organic Rankine cycle system.

non-ideal and non-classical gas dynamic phenomena can occur in the vapor phase, close to the liquid-vapor saturation curve in fluids with high molecular complexity [46]. Better knowledge of the non-ideal thermodynamic behavior of the mixtures in non-ideal compressible fluid region and development of accurate thermodynamic models for mixtures of siloxanes can improve the study of gasdynamic phenomena and the use of mixtures of siloxanes in experiments and industrial applications which is not considered until now due to the lack and complexity of the their thermodynamics.

Another aim of this work is the thermal stability of linear siloxanes and their mixtures. An expected feature of mixtures of siloxanes is that they exhibit a higher thermal stability limit than their pure components, due to the redistribution process occurring at high temperature, where more complex molecules decompose into simpler molecules, which then recombine again into the more complex molecule [47, 48]. This redistribution and therefore the possible increase of the thermal stability temperature can enhance the use of complex molecular fluids for experimental and industrial applications.

1.2 Mixtures in organic Rankine power cycles

Mixtures can be used to improve the energy efficiency of ORCs [8, 49–51]. In Fig. 1.1 a schematic design of an ORC system is shown, which consists of four main com-

ponents: evaporator, expander, condenser, and pump. In this case the basic ORC is considered without recuperation and zeotropic mixtures. The working fluid is low temperature liquid at the pump inlet and then pressurized by the pump ($1 \rightarrow 2$) and is directed to the evaporator where the working fluid is heated, evaporated and (optionally) superheated (depending on the application) by the heat source ($2 \rightarrow 3$). The high temperature and pressurized vapor then enters the turbine where the thermal energy is converted into mechanical power ($3 \rightarrow 4$). The mechanical power is converted to electrical power via a generator connected to the turbine. The cycle is completed by condensation of the low pressure vapor exiting the turbine outlet in the condenser by the heat source, where it is condensed into saturated or subcooled liquid ($4 \rightarrow 1$) [52].

The advantage of using mixtures as working fluids lies within the matching of the temperature profile of the working fluid and the heat source and sink in the evaporator and condenser. Real heat transfer processes which are driven by a finite temperature difference are generally irreversible. When the irreversibility or entropy increase of the heat transfer is large, the potential of extracting useful work from the heat source is decreased. The entropy production can be reduced by matching the temperature profile of the working fluid with the heat source and sink. The lowest entropy production in the evaporator and condenser occurs when the temperature change of the working fluid is the same as that of the heat or cold source, this is known as glide matching [53].

Pure component fluids may suffer from loss of efficiency, because in most applications the temperature of the heat source and sink vary during heat transfer while the temperature of the working fluid remains constant which is ideally isobaric and isothermal during phase change in the evaporator and condenser. The phase change for pure components in the s–T plane is shown in Fig. 1.2a, where point $2 \rightarrow 3$ is the evaporation $4 \rightarrow 1$ the condensation. This causes bad temperature matching between the working fluid and heat source and may cause large pinch points at one end of the evaporator and condenser, leading to an increase of process irreversibility and thus lower efficiency [7, 49]. Alternatively, supercritical ORCs which operate above the critical point, so no evaporation occurs in the cycle, can have better matches with the heat source. However the supercritical ORC operate at very high pressure, adding system costs and safety issues.

The advantage in the use of mixtures is during the phase change which is ideally isobaric but not isothermal for mixtures. Fig. 1.2a shows the phase transition in the s–T plane for mixtures, where point $2 \rightarrow 3$ is the evaporation $4 \rightarrow 1$ the condensation. The difference between the saturation temperature on the liquid side and vapor side ($2 \rightarrow 3$ and $4 \rightarrow 1$) in an isobaric process is called the temperature glide. Fig. 1.2b shows that a better match between temperature profile of the working fluid and the heat source and sink can be obtained for a mixture. The working fluid mixtures properties can be optimized to provide a good match between the temperature glide of the working fluid and the heat source and sink [8, 54]. This optimization of the temperature profile leads to a decrease of the process irreversibility and increase of

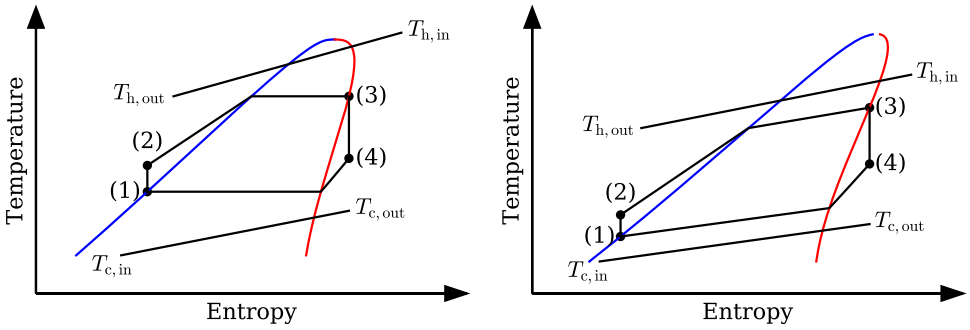

(a) Pure working fluid.

(b) Mixture working fluid.

Figure 1.2: Schematic Entropy vs. Temperature diagram of an arbitrary fluid for the organic Rankine cycle shown in Fig. 1.1. The blue line represents the liquid side saturation curve (–) and the red line the vapor side saturation curve (–). The points correspond to the schematic organic Rankine cycle in Fig. 1.1.

the cycle efficiency.

Though the use of mixtures can increase the efficiency of the cycle, there are also limitations. It is known that the heat transfer coefficient of mixtures is generally lower compared to pure fluids. This leads to larger heat exchangers areas required for ORCs using mixtures, which increases the overall cost of the system. Another limitation is that during operation the composition of the mixture can change due to leakages and degassing of the system. This change in composition of the mixture can lead to different thermodynamic properties from which the cycle is designed for and a decrease in cycle efficiency.

The use of mixtures can also have advantages in other power cycles with organic fluids where phase changes occur. Also mixtures are already widely used in refrigerant cycles to better match the temperature profile of the working fluid with the heat source and sink [28, 29]. In Kalina power cycles, mixtures are key to the working principle of the cycles (for more details see the review by Zhang et al. [55]). Another examples is the super critical CO_2 Brayton cycle. Due to the low critical temperature of pure CO_2 only low temperature heat sinks are of interest. Though by using a mixture of CO_2 and a second component the critical point can be increased so heat sinks at higher temperatures are also suitable without a significant efficiency loss [45].

1.3 non-ideal compressible fluid region for mixtures

Gas expansions are common processes in numerous industrial applications. Examples can be found in the power, oil and gas, chemical, process and refrigeration industries. Fluids are expanded in order to generate mechanical power (e.g., in turbines,

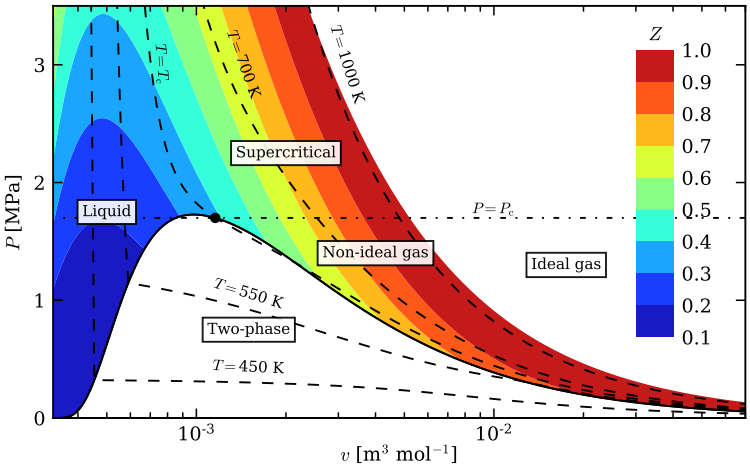

Figure 1.3: Specific volume vs. Pressure diagram for binary mixture of MM–MD_4M with percentage mole fraction for MM of 50 mol%. Deviations of volumetric properties from ideal gas law are indicated by the compressibility factor $Z = Pv/RT$. The isotherms are shown by the dashed black lines (– –), the critical isobar by the dashed dot line (-.), and the black bullet indicates the mixtures critical point (•). Generated with the Helmholtz energy equation of state implemented in REFPROP [56] and state-of-the-art coefficients are derived by Thol et al. [57] for MM and König et al. [58] for MD_4M . The applied mixture model is the GERG-2008 mixture formulation [59] with estimated mixing parameters.

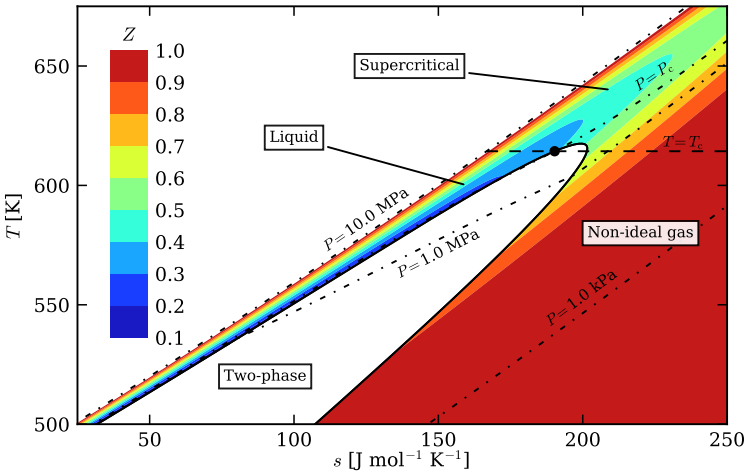

Figure 1.4: Specific entropy vs. Temperature diagram for binary mixture of MM–MD_4M with percentage mole fraction for MM of 50 mol%. Deviations of isentropic properties from ideal gas law are indicated by the compressibility factor $Z = Pv/RT$. The isobars are shown by the dashed dot black lines (-.), the critical isotherm by the dashed line (– –), and the black bullet indicates the mixtures critical point (•). Generated with the Helmholtz energy equation of state and estimated mixing parameters [56].

rockets, mixers, wind tunnels for aerodynamic testing and for material removal). In general terms, the process conditions, namely, the initial thermodynamic state and expansion ratio, together with the fluid characteristics determine the dynamics of an expansion.

Properties for fluids operating at high temperature and low pressure can be estimated using the polytropic ideal gas law with good accuracy as long as the fluid states are not close to the liquid-vapor saturation curve. For the polytropic ideal gas law the compressibility factor is equal to unity and the isochoric and isobaric specific heat are constant,

$$Z = \frac{Pv}{RT} = 1, \quad c_v = \text{constant}, \quad c_p = \text{constant}, \tag{1.1}$$

where Z is the compressibility factor, P the pressure, T the temperature, v the specific volume, R the universal gas constant, and c_v and c_p the isochoric and isobaric specific heat respectively. However, for fluids operating in thermodynamic states close to the saturation curve, molecular interactions become more significant and the polytropic ideal gas law is no longer applicable. For mixtures the interaction between different types of molecules also has to be taken into account, adding a degree of difficulty in comparison with pure fluid thermodynamics. The thermodynamic region close to the saturation curve is called the non-ideal compressible fluid region and the actual behavior of gases deviates significantly from the predicted properties by the polytropic ideal gas law.

Non-ideal gases have different volumetric behavior than gases in the ideal-gas region. More complex equations of state have to be used to describe the non-ideal compressible fluid region as well as the liquid-vapor region, more details about these more complex equations of state are given in Chapter 2. For the non-ideal compressible fluid region the compressibility factor is not equal to unity. The volumetric property and entropic property deviation from fluids in the non-ideal compressible fluid region in comparison with the ideal-gas region is given by the deviation from the compressibility factor from unity. The compressibility factor deviations are shown in Figs. 1.3 and 1.4 for volumetric and entropic properties respectively. Also the caloric behavior in the non-ideal compressible fluid region differs from the ideal-gas region, and the isochoric and isobaric specific heat can not be taken as constants. This difference between the non-ideal compressible fluid and ideal-gas region results in the variation of properties (e.g. along an isentrope and isotherm) is much larger in the non-ideal compressible fluid region. The region for temperatures above the critical temperature ($T > T_c$) and pressures above the critical pressure ($P > P_c$) is the supercritical region.

In turn deviation in the fluid dynamic properties occurs between fluids operating in the non-ideal compressible fluid and ideal-gas region due to the thermodynamic deviations. These fluid dynamic properties in the non-ideal compressible fluid region are known as non-ideal or non-ideal compressible fluid effects. Fluids composed of

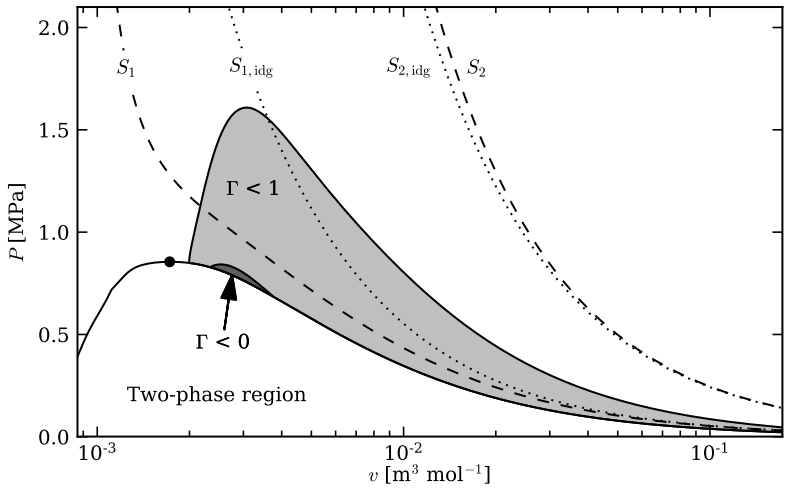

Figure 1.5: Specific volume vs. Pressure diagram for binary mixture of MD_3M–MD_4M with percentage mole fraction for MD_3M of 10 mol%. The non-ideal gasdynamic region ($\Gamma < 1$) is indicated by the light gray area, the dark gray area indicates the non-classical gasdynamic region ($\Gamma < 0$). The dashed black lines show the isentropic lines, the dotted black lines show the ideal gas isentropic lines, and the mixtures critical point is given by the black bullet. Generated with the Helmholtz energy equation of state implemented in REFPROP [56].

molecules with high molecular complexity exhibit qualitatively different fluid dynamic behavior which can be observed in a limited thermodynamic region close to the saturation curve [46, 60, 61], which is called the non-ideal compressible fluid region, due to the non-ideal dependency of the speed of sound on the density in the non-ideal compressible fluid region of complex fluids. The condition for non-ideal behavior is indicated by the thermodynamic property, the fundamental derivative of gas dynamic introduced by [62] and defined as

$$\Gamma = 1 - \frac{v}{c}\left(\frac{\partial c}{\partial v}\right)_s = \frac{v^3}{2c^2}\left(\frac{\partial^2 P}{\partial v^2}\right)_s, \tag{1.2}$$

where ρ is the density, c the speed of sound, and s the entropy. Γ is a direct derivate of the speed of sound, so non-ideal behavior of the speed of sound directly affects Γ. The necessary condition for fluids to exhibit non-ideal fluid dynamic effects is that Γ is smaller than one ($\Gamma < 1$). When Γ is much larger than one ($\Gamma >> 1$), the fluid exhibits ideal-gas fluid dynamic behavior. In Fig. 1.5 the non-ideal compressible fluid region is indicated by the light gray area. The most remarkable effect in this region is the increase of the speed of sound upon isentropic expansion, which can lead to non-monotone behavior of the Mach number along an isentropic expansion [63]. In comparison, for an isentropic ideal-gas expansion the Mach number increases monotonically. Fluids composed of even more complex molecules, the

so-called Bethe-Zel'dovich-Thompson (BZT) fluids, can exhibit non-classical gasdynamic behavior phenomena which possibly include rarefaction shock waves [32, 64–66]. This non-classical effects are admissible when Γ is smaller than zero ($\Gamma < 0$). The thermodynamic region where these non-classical gasdynamic effects may occur is indicated in Fig. 1.5 by the dark gray area. Several attempts have been made to observe non-classical gasdynamic phenomena, but to date no experimental evidence is available. The notable experiment by Borisov et al. [67] is later refuted due to additional knowledge and simulations [68–71]. The experimental attempts by Fergason et al. [72] failed due to thermal decomposition of the fluid. The experiment showed that the thermal stability of the suitable organic fluids to exhibit non-classical gasdynamic effects is a limited factor. This is because the thermodynamic region in which non-classical effects can occur ($\Gamma < 0$) is very close to the thermal stability limit of the organic fluids. More recently experiments are conducted by Mathijssen et al. [73] in the non-ideal compressible fluid region, although non-classical effects are not observed at this moment promising preliminary results are obtained for future research. At the compressible fluid dynamics for renewable energy applications laboratory (CREA) at the Politecnico di Milano measurements are performed on the Test Rig for Organic Vapors (TROVA). The TROVA is a novel blow down wind tunnel, designed and commissioned for experiments in the non-ideal compressible fluid region and possible observation of non-classical effects of expanding flows [74]. Promising preliminary results are obtained by Spinelli et al. [75, 76] for the linear siloxane fluid MDM in the non-ideal thermodynamic region.

Thermodynamic properties of mixtures operating in the ideal-gas region scale linearly with the mole fraction of each component, under the assumption of ideal mixing by the components. For mixtures operating in the non-ideal compressible fluid region this is different, the thermodynamic properties do not scale linearly with the mole fraction of each component. The non linear behavior is due to the interaction between different molecules in the mixtures. The critical temperature, pressure and specific volume are typical properties which exhibit this non ideal behavior upon mixing of different components. This also holds for most of the thermodynamic properties in the non-ideal compressible fluid region, this non-ideal behavior upon mixing also includes the speed of sound and so Γ being a derived thermodynamic property [40]. As shown by Guardone et al. [41], Γ exhibits non-monotone behavior with respect to the molar fraction in binary mixtures upon mixing of different components.

The use of mixtures allow for the thermodynamic properties of the fluid to be adapted in a virtually continuous way, which in turn can enhance the position and extent the region in which non-ideal and even non-classical effects occur. Another advantage for the use of mixtures of molecular complex fluids is the increase in the thermal-stability limit. It is shown that mixtures of linear siloxanes exhibit a higher thermal stability limit [47, 48], this is due to the rearrangements of molecules. At higher temperatures the more complex molecules decompose into small quantities of

their simpler molecules. Over time this decomposition leads to a reduction in the change of thermodynamic properties and the fluids can possibly operate above their thermal stability limit.

1.4 Thesis outline

This thesis is divided into two parts. The first part focuses on the fundamentals of the thermodynamics of mixtures and the speed of sound in the non-ideal thermodynamic regions for mixtures of fluids with high molecular complexity. The second part is related to experimental research on pure linear siloxanes and binary mixtures of linear siloxanes. Firstly, measurements are performed on vapor-liquid equilibrium and subsequently modeling of new mixture models for linear siloxanes is conducted. Finally a thermal stability test-rig is designed and commissioned to determine the thermal stability limit and decomposition products of pure fluids and mixtures. Measurements are performed on the thermal stability of pure linear siloxanes. In this work only binary mixtures are taken into consideration, because the focus lies on expanding the knowledge and understanding of the interaction between two components. Adding more components will add extra uncertainties and effects which are not the focus of this research.

Chapter 2 gives a brief introduction into the thermodynamics of mixtures. This is done due to the difference from pure fluids and the increased complexity of the thermodynamics of mixtures. First, the vapor-liquid equilibrium behavior of mixtures is explained and the numerical tools used for the calculation are elaborated. Secondly the theory behind the determination of the critical point of mixtures is explained as well as the methodology to determine the mixtures critical point. Finally the thermodynamic models for multicomponent fluids used in this work are elaborated which consist of the polytropic van der Waals equation of state, the Peng-Robinson equation of state, and the multiparameter Helmholtz energy equation of state.

Chapter 3 presents a fundamental research on the speed of sound behavior for binary mixtures of molecular complex fluids in the non-ideal thermodynamic region. The speed of sound behavior is qualitatively investigated using the polytropic van der Waals model. For the evaluation, the speed of sound is made dimensionless to show the different contribution of the ideal gas part, repulsive forces, and attractive forces and the relation to the pure component properties. Subsequently the speed of sound behavior for binary mixtures of perfluorocarbons is analyzed using the polytropic van der Waals model to compare with the linear siloxane mixtures. The Helmholtz energy equation of state is used to verify the speed of sound behavior for the binary mixtures of linear siloxanes and perfluorocarbons. Finally, the Helmholtz energy equation of state is used to investigate the fundamental derivative of gas dynamics behavior for binary mixtures of linear siloxanes.

Chapter 4 reports new vapor-liquid equilibrium measurements of binary mixtures of linear siloxanes and the modeling of new binary interaction parameters for the Helmholtz energy equation of state. The measurements and modeling are performed at the National Institute of Standards and Technology (NIST). The measurements performed are bubble-point pressure measurements of binary mixtures of linear siloxanes. Firstly the various components of the apparatus and their specifications are described. Secondly the mixture preparation is elaborated as well as the procedure for the measurement of the bubble-point pressures. Subsequently the data analysis consisting of the analysis of the vapor quality in the equilibrium cell and the thorough uncertainty analysis is discussed. Next, the results and discussion of the bubble-point measurements are given and in addition an analysis of the impact of air impurity on the bubble-point pressure is conducted. Finally, the modeling of new binary interaction parameters for the Helmholtz energy model is performed using the measured bubble-point pressures.

Chapter 5 deals with the design and commissioning of an experimental test-rig to determine the thermal stability and decomposition products of pure fluids and mixtures. The method and experimental apparatus in this research uses statistical analysis to determine decomposition based on the deviation in vapor pressure of the stressed fluid from the unstressed reference fluid. When thermal decomposition is observed, chemical analysis of the liquid and vapor phase of the decomposed fluid is conducted to determine the decomposition products. Firstly the equipment and measurement procedure are described in detail. Followed by the data analysis, which include pressure deviation during thermal stress test, deviation of stressed fluid vapor pressure from reference fluid vapor pressure, and chemical analysis. Finally results of the thermal stability and decomposition products of pure hexamethyldisiloxane (MM) and octamethyltrisiloxane (MDM) are reported.

References

[1] International Energy Agency. *CO_2 Emissions from Fuel Combustion 2017*. IEA, 2017. ISBN: 978-92-64-27818-9.

[2] U.S. Energy Information Administration. *Annual Energy Outlook 2017*. 2017. URL: https://www.eia.gov/outlooks/aeo/ (visited on).

[3] R. K. Pachauri and L. A. Meyer, eds. *Climate Change 2014: Synthesis Report*. Contribution of Working Groups I, II and III to the Fifth Assessment Report of the Intergovernmental Panel on Climate Change. Intergovernmental Panel on Climate Change, 2014. ISBN: ISBN 978-92-9169-143-2.

[4] T. A. Boden, G. Marland, and R. J. Andres. *Regional, and National Fossil-Fuel CO_2 Emissions*. 2017. DOI: 10.3334/CDIAC/00001_V2017.

[5] S. Michaelidas and E. Efstathios. "Environmental and Ecological Effects of Energy Production and Consumption". In: Springer Berlin Heidelberg, 2012, pp. 33–63. ISBN: 978-3-642-20951-2. DOI: 10.1007/978-3-642-20951-2_2.

[6] United Nations. *United Nations Environment*. 2017. URL: http://web.unep.org/.

[7] E. Macchi and M. Astolfi, eds. *Organic Rankine Cycle (ORC) Power Systems*. 1st ed. Woodhead Publishing, 2017.

[8] G. Angelino and P. Colonna. "Multicomponent Working Fluids For Organic Rankine Cycles (ORCs)". In: *Energy* 23.6 (1998), pp. 449–463. DOI: 10.1016/S0360-5442(98)00009-7.

[9] P. Colonna, E. Casati, C. Trapp, T. Mathijssen, J. Larjola, T. Turunen-Saaresti, and A. Uusitalo. "Organic Rankine Cycle Power Systems: From the Concept to Current Technology, Applications, and an Outlook to the Future". In: *J. Eng. Gas Turbines Power* 137.10 (2015). DOI: 10.1115/1.4029884.

[10] D. M. Ginosar, L. M. Petkovic, and D. P. Guillen. "Thermal Stability of Cyclopentane as an Organic Rankine Cycle Working Fluid". In: *Energy & Fuels* 25.9 (2011), pp. 4138–4144. DOI: 10.1021/ef200639r.

[11] O. Badr, S. D. Probert, and P. W. O'Callaghan. "Selecting a working fluid for a Rankine-cycle engine". In: *Appl. Energy* 21.1 (1985), pp. 1–42. DOI: 10.1016/0306-2619(85)90072-8.

[12] C. Invernizzi and P. Iora. "Heat recovery from a micro - gas turbine by vapour jet refrigeration systems". In: *Appl. Therm. Eng.* 25.8–9 (2005), pp. 1233–1246. DOI: 10.1016/j.applthermaleng.2004.08.008.

[13] C. Invernizzi, P. Iora, and P. Silva. "Bottoming micro - Rankine cycles for micro - gas turbines". In: *Appl. Therm. Eng.* 27.1 (2007), pp. 100–110.

[14] A. Franco. "Power production from a moderate temperature geothermal resource with regenerative Organic Rankine Cycles". In: *Energy for Sustainable Development* 15.4 (2011), pp. 411–419. DOI: 10.1016/j.esd.2011.06.002.

[15] M. Wang, J. Wang, Y. Zhao, P. Zhao, and Y. Dai. "Thermodynamic analysis and optimization of a solar-driven regenerative organic Rankine cycle (ORC) based on flat-plate solar collectors". In: *Appl. Therm. Eng.* 50.1 (2013), pp. 816–825. DOI: 10.1016/j.applthermaleng.2012.08.013.

[16] V. Minea. "Power generation with {ORC} machines using low-grade waste heat or renewable energy". In: *Appl. Therm. Eng.* 69.1-2 (2014), pp. 143–154. DOI: 10.1016/j.applthermaleng.2014.04.054.

[17] J. Bao and L. Zhao. “A review of working fluid and expander selections for organic Rankine cycle”. In: *Renewable Sustainable Energy Rev.* 24.Supplement C (2013), pp. 325–342. ISSN: 1364-0321. DOI: 10.1016/j.rser.2013.03.040.

[18] J. S. Brown, R. Brignoli, and T. Quine. “Parametric investigation of working fluids for organic Rankine cycle applications”. In: *Appl. Therm. Eng.* 90.Supplement C (2015), pp. 64–74. ISSN: 1359-4311. DOI: 10.1016/j.applthermaleng.2015.06.079.

[19] J. Hærvig, K. Sørensen, and T. J. Condra. “Guidelines for optimal selection of working fluid for an organic Rankine cycle in relation to waste heat recovery”. In: *Energy* 96.Supplement C (2016), pp. 592–602. ISSN: 0360-5442. DOI: 10.1016/j.energy.2015.12.098.

[20] G. Angelino. “Carbon Dioxide Condensation Cycles for Power Generation”. In: *J. Eng. Power* 90.3 (1968), pp. 287–295. DOI: 10.1115/1.3609190.

[21] E. Feher. “The supercritical thermodynamic power cycle”. In: *Energy Conversion* 8.2 (1968), pp. 85–90. ISSN: 0013-7480. DOI: 10.1016/0013-7480(68)90105-8.

[22] V. Dostal, P. Hejzlar, and M. J. Driscoll. “The Supercritical Carbon Dioxide Power Cycle: Comparison to Other Advanced Power Cycles”. In: *Nucl. Technol.* 154.3 (2006), pp. 283–301. DOI: 10.13182/NT06-A3734.

[23] Y. M. Kim, C. G. Kim, and D. Favrat. “Transcritical or supercritical CO_2 cycles using both low- and high-temperature heat sources”. In: *Energy* 43.1 (2012). 2nd International Meeting on Cleaner Combustion (CM0901-Detailed Chemical Models for Cleaner Combustion), pp. 402–415. ISSN: 0360-5442. DOI: 10.1016/j.energy.2012.03.076.

[24] Y. Chen, P. Lundqvist, A. Johansson, and P. Platell. “A comparative study of the carbon dioxide transcritical power cycle compared with an organic rankine cycle with R123 as working fluid in waste heat recovery”. In: *Appl. Therm. Eng.* 26.17 (2006), pp. 2142–2147. ISSN: 1359-4311. DOI: 10.1016/j.applthermaleng.2006.04.009.

[25] J. Sarkar. “Review and future trends of supercritical CO_2 Rankine cycle for low-grade heat conversion”. In: *Renewable Sustainable Energy Rev.* 48.Supplement C (2015), pp. 434–451. ISSN: 1364-0321. DOI: 10.1016/j.rser.2015.04.039.

[26] G. Angelino and C. Invernizzi. “Potential performance of real gas Stirling cycle heat pumps”. In: *Int. J. Refrig* 19.6 (1996), pp. 390–399. ISSN: 0140-7007. DOI: 10.1016/S0140-7007(96)00022-9.

[27] G. Angelino and C. Invernizzi. “Real gas effects in Stirling engines”. In: *Collection of Technical Papers. 35th Intersociety Energy Conversion Engineering Conference and Exhibit (IECEC) (Cat. No.00CH37022)*. Vol. 1. 2000, 69–75 vol.1. DOI: https://dx.doi.org/10.1109/IECEC.2000.870630.

[28] R. Radermacher and Y. Hwang, eds. *Vapor Compression Heat Pumps with Refrigerant Mixtures*. 1st ed. CRC Press, 2005. ISBN: 9780849334894.

[29] G. Venkatarathnam. *Cryogenic Mixed Refrigerant Processes*. 1st ed. Springer-Verlag New York, 2008. ISBN: 978-0-387-78513-4. DOI: 10.1007/978-0-387-78514-1.

[30] A. Modi and F. Haglind. “A review of recent research on the use of zeotropic mixtures in power generation systems”. In: *Energy Convers. Manage.* 138.Supplement C (2017), pp. 603–626. ISSN: 0196-8904. DOI: 10.1016/j.enconman.2017.02.032.

[31] G. B. Abadi and K. C. Kim. “Investigation of organic Rankine cycles with zeotropic mixtures as a working fluid: Advantages and issues”. In: *Renewable Sustainable Energy Rev.* 73.Supplement C (2017), pp. 1000–1013. ISSN: 1364-0321. DOI: 10.1016/j.rser.2017.02.020.

[32] B. P. Brown and B. M. Argrow. "Application of Bethe-Zel'dovich-Thompson Fluids in Organic Rankine Cycle Engines". In: *J. Propul. Power* 16.6 (2000), pp. 1118–1124. DOI: https://dx.doi.org/10.2514/2.5686.

[33] C. Zamfirescu and I. Dincer. "Performance investigation of high-temperature heat pumps with various BZT working fluids". In: *Thermochim. Acta* 488.1 (2009), pp. 66–77. ISSN: 0040-6031. DOI: 10.1016/j.tca.2009.01.028.

[34] P. Colonna and S. Rebay. "Numerical simulation of dense gas flows on unstructured grids with an implicit high resolution upwind Euler solver". In: *Int. J. Numer. Methods Fluids* 46.7 (2004), pp. 735–765. ISSN: 1097-0363. DOI: 10.1002/fld.762.

[35] P. Cinnella and P. M. Congedo. "Numerical Solver for Dense Gas Flows". In: *AIAA* 43.11 (2005), pp. 2458–2461. DOI: https://dx.doi.org/10.2514/1.16335.

[36] P. M. Congedo, C. Corre, and P. Cinnella. "Numerical investigation of dense-gas effects in turbomachinery". In: *Computers & Fluids* 49.1 (2011), pp. 290–301. ISSN: 0045-7930. DOI: 10.1016/j.compfluid.2011.06.012.

[37] P. Colonna, J. Harinck, S. Rebay, and A. Guardone. "Real-Gas Effects in Organic Rankine Cycle Turbine Nozzles". In: *J. Propul. Power* 24.2 (2008), pp. 282–294. DOI: https://dx.doi.org/10.2514/1.29718.

[38] A. P. S. Wheeler and J. Ong. "The Role of Dense Gas Dynamics on ORC Turbine Performance". In: *Turbo Expo: Power for Land, Sea, and Air* Volume 2: Aircraft Engine; Coal, Biomass and Alternative Fuels; Cycle Innovations.55133 (2013). DOI: https://dx.doi.org/10.1115/GT2013-95858.

[39] A. Guardone and D. Vimercati. "Exact solutions to non-classical steady nozzle flows of Bethe-Zel'dovich-Thompson fluids". In: *J. Fluid Mech.* 800 (2016), pp. 278–306. DOI: https://dx.doi.org/10.1017/jfm.2016.392.

[40] P. Colonna and P. Silva. "Dense Gas Thermodynamic Properties of Single and Multicomponent Fluids for Fluid Dynamics Simulations". In: *J. Fluids Eng* 125.3 (2003), pp. 414–427. DOI: https://dx.doi.org/10.1115/1.1567306.

[41] A. Guardone, P. Colonna, E. Casati, and E. Rinaldi. "Non-classical gas dynamics of vapour mixtures". In: *J. Fluid Mech.* 741 (2014), pp. 681–701. DOI: https://dx.doi.org/10.1017/jfm.2013.13.

[42] B. Subramaniam, R. A. Rajewski, and K. Snavely. "Pharmaceutical Processing with Supercritical Carbon Dioxide". In: *J. Pharm. Sci.* 86.8 (1997), pp. 885–890. ISSN: 0022-3549. DOI: 10.1021/js9700661.

[43] W. W. Bober and W. L. Chow. "Non-ideal Isentropic Gas Flow Through Converging-Diverging Nozzles". In: *J. Fluids Eng.* 112.4 (1990), pp. 455–460. DOI: 10.1115/1.2909425.

[44] J. B. Anders. "Heavy gas wind-tunnel research at Langley Research Center". In: *ASME Paper 93-FE-5* (1993).

[45] S. Lasala, D. Bonalumi, E. Macchi, R. Privat, and J. N. Jaubert. "The design of CO_2-based working fluids for high-temperature heat source power cycles". In: *Energy Procedia* 129.Supplement C (2017). 4th International Seminar on ORC Power Systems, September 13-15th 2017, Politecnico Di Milano Bovisa Campus, Milano, Italy, pp. 947–954. ISSN: 1876-6102. DOI: 10.1016/j.egypro.2017.09.125.

[46] P. Colonna and A. Guardone. "Molecular interpretation of nonclassical gas dynamics of dense vapors under the van der Waals model". In: *Phys. Fluids* 18.5, 056101 (2006). DOI: https://dx.doi.org/10.1063/1.2196095.

[47] G. Angelino and C. Invernizzi. “Cyclic Methylsiloxanes as Working Fluids for Space Power Cycles”. In: *J. Sol. Energy Eng.* 115.3 (1993), pp. 130–137. DOI: https://dx.doi.org/10.1115/1.2930039.

[48] P. R. Dvornic. “High temperature stability of cyclosiloxanes”. In: *Silicon Compounds: Silanes and Silicones: A Survey of Properties and Chemistry*. Morrisville, PA : Gelest, Inc, 2008, pp. 441–454.

[49] M. Chys, M. van den Broek, B. Vanslambrouck, and M. D. Paepe. “Potential of zeotropic mixtures as working fluids in organic Rankine cycles”. In: *Energy* 44.1 (2012). Integration and Energy System Engineering, European Symposium on Computer - Aided Process Engineering 2011, pp. 623–632. ISSN: 0360-5442. DOI: 10.1016/j.energy.2012.05.030.

[50] J. L. Wang, L. Zhao, and X. D. Wang. “A comparative study of pure and zeotropic mixtures in low-temperature solar Rankine cycle”. In: *Appl. Energy* 87.11 (2010), pp. 3366–3373. ISSN: 0306-2619. DOI: 10.1016/j.apenergy.2010.05.016.

[51] F. Heberle, M. Preißinger, and D. Brüggemann. “Zeotropic mixtures as working fluids in Organic Rankine Cycles for low-enthalpy geothermal resources”. In: *Renewable Energy* 37.1 (2012), pp. 364–370. ISSN: 0960-1481. DOI: 10.1016/j.renene.2011.06.044.

[52] M. J. Moran and H. N. Shapiro. *Fundamentals of Engineering Thermodynamics*. 5th ed. John Wiley & Sons, Inc., 2007. ISBN: 978-0-470-03037-0.

[53] G. S. C. Prasad, C. S. Kumar, S. S. Murthy, and G. Venkatarathnam. “Performance of an organic Rankine cycle with multicomponent mixtures”. In: *Energy* 88.Supplement C (2015), pp. 690–696. ISSN: 0360-5442. DOI: 10.1016/j.energy.2015.05.102.

[54] M. Kolahi, M. Yari, S. M. S. Mahmoudi, and F. Mohammadkhani. “Thermodynamic and economic performance improvement of ORCs through using zeotropic mixtures: Case of waste heat recovery in an offshore platform”. In: *Case Studies in Thermal Engineering* 8 (2016), pp. 51–70. DOI: 10.1016/j.csite.2016.05.001.

[55] X. Zhang, M. He, and Y. Zhang. “A review of research on the Kalina cycle”. In: *Renewable Sustainable Energy Rev.* 16.7 (2012), pp. 5309–5318. ISSN: 1364-0321. DOI: 10.1016/j.rser.2012.05.040.

[56] E. W. Lemmon, I. H. Bell, M. L. Huber, and M. O. McLinden. *NIST Standard Reference Database 23: Reference Fluid Thermodynamic and Transport Properties - REFPROP, Version 10*. 2018.

[57] M. Thol, F. Dubberke, G. Rutkai, T. Windmann, A. Köster, R. Span, and J. Vrabec. “Fundamental equation of state correlation for hexamethyldisiloxane based on experimental and molecular simulation data”. In: *Fluid Phase Equilib.* 418.Supplement C (2016). Special Issue covering the Nineteenth Symposium on Thermophysical Properties, pp. 133–151. ISSN: 0378-3812. DOI: 10.1016/j.fluid.2015.09.047.

[58] König and M. Thol. “Helmholtz equation of state for Dodecamethylpentasiloxane (MD_3M) and Tetradecamethylhexasiloxane (MD_4M)”. To be published. 2017.

[59] O. Kunz and W. Wagner. “The GERG-2008 Wide-Range Equation of State for Natural Gases and Other Mixtures: An Expansion of GERG-2004”. In: *Journal of Chemical & Engineering Data* 57.11 (2012), pp. 3032–3091. DOI: 10.1021/je300655b.

[60] M. S. Cramer and L. M. Best. “Steady, isentropic flows of dense gases”. In: *Physics of Fluids A: Fluid Dynamics* 3.1 (1991), pp. 219–226. DOI: 10.1063/1.857855.

[61] M. S. Cramer and R. N. Fry. “Nozzle flows of dense gases”. In: *Physics of Fluids A: Fluid Dynamics* 5.5 (1993), pp. 1246–1259. DOI: 10.1063/1.858610.

[62] W. D. Hayes. *Gasdynamic Discontinuities*. Princeton University Press, 1960. URL: http://www.jstor.org/stable/j.ctt183pmwn.

[63] J. Harinck. "Super- and Transcritical Fluid Expansions for Next-Generation Energy Conversion Systems". PhD thesis. Technical University of Delft, Dec. 2010. ISBN: 9789090249148.

[64] H. A. Bethe. "On the Theory of Shock Waves for an Arbitrary Equation of State". In: *Classic Papers in Shock Compression Science*. New York, NY: Springer New York, 1998, pp. 421–495. ISBN: 978-1-4612-2218-7. DOI: 10.1007/978-1-4612-2218-7_11.

[65] P. Colonna, A. Guardone, and N. R. Nannan. "Siloxanes: A new class of candidate Bethe-Zel'dovich-Thompson fluids". In: *Phys. Fluids* 19.8 (2007), p. 086102. DOI: 10.1063/1.2759533.

[66] A. Kluwick. "Non-Ideal Compressible Fluid Dynamics: A Challenge for Theory". In: *J. Phys. Conf. Ser.* 821.1 (2017), p. 012001. URL: http://stacks.iop.org/1742-6596/821/i=1/a=012001.

[67] A. A. Borisov, A. A. Borisov, S. S. Kutateladze, and V. E. Nakoryakov. "Rarefaction shock wave near the critical liquid–vapour point". In: *J. Fluid Mech.* 126 (1983), pp. 59–73. DOI: https://dx.doi.org/10.1017/S002211208300004X.

[68] M. S. Cramer and R. Sen. "Shock formation in fluids having embedded regions of negative nonlinearity". In: *The Physics of Fluids* 29.7 (1986), pp. 2181–2191. DOI: https://dx.doi.org/10.1063/1.865555.

[69] S. S. Kutateladze, V. E. Nakoryakov, and A. A. Borisov. "Rarefaction Waves in Liquid and Gas-Liquid Media". In: *Annu. Rev. Fluid Mech.* 19.1 (1987), pp. 577–600. DOI: 10.1146/annurev.fl.19.010187.003045.

[70] P. A. Thompson. "Liquid-Vapor Adiabatic Phase Changes and Related Phenomena". In: *Nonlinear Waves in Real Fluids*. Vienna: Springer Vienna, 1991, pp. 147–213. ISBN: 978-3-7091-2608-0. DOI: https://dx.doi.org/10.1007/978-3-7091-2608-0_6.

[71] S. H. Fergason, T. L. HO, B. M. Argrow, and G. Emanuel. "Theory for producing a single-phase rarefaction shock wave in a shock tube". In: *J. Fluid Mech.* 445 (2001), pp. 37–54. DOI: https://dx.doi.org/10.1017/S0022112001005444.

[72] S. Fergason, A. Guardone, and B. Argrow. "Construction and Validation of a Dense Gas Shock Tube". In: *J. Thermophys. Heat Transfer* 17.3 (2003), pp. 326–333. DOI: https://dx.doi.org/10.2514/2.6789.

[73] T. Mathijssen, M. Gallo, E. Casati, N. R. Nannan, C. Zamfirescu, A. Guardone, and P. Colonna. "The flexible asymmetric shock tube (FAST): a Ludwieg tube facility for wave propagation measurements in high-temperature vapours of organic fluids". In: *Exp. Fluids* 56.10 (2015), p. 195. DOI: 10.1007/s00348-015-2060-1.

[74] S. A., M. Pini, V. Dossena, P. Gaetani, and F. Casella. "Design, Simulation, and Construction of a Test Rig for Organic Vapors". In: *Engineering for Gas Turbines and Power* 135.4 (2013). DOI: 10.1115/1.4023114.

[75] A. Spinelli, G. Cammi, M. Zocca, S. Gallarini, F. Cozzi, P. Gaetani, V. Dossena, and A. Guardone. "Experimental observation of non-ideal expanding flows of Siloxane MDM vapor for ORC applications". In: *Energy Procedia* 129.Supplement C (2017). 4th International Seminar on ORC Power Systems, September 13-15th 2017 Politecnico di Milano Bovisa Campus Milano, Italy, pp. 1125–1132. DOI: 10.1016/j.egypro.2017.09.237.

[76] A. Spinelli, F. Cozzi, G. Cammi, M. Zocca, P. Gaetani, V. Dossena, and A. Guardone. "Preliminary characterization of an expanding flow of siloxane vapor MDM". In: *J. Phys. Conf. Ser.* 821.1 (2017), p. 012022. URL: http://stacks.iop.org/1742-6596/821/i=1/a=012022.

CHAPTER 2

THERMODYNAMICS OF MULTICOMPONENT MIXTURES

2.1 Introduction

This section gives a brief introduction into the thermodynamics of mixtures. The governing equations rely on an equation of state model for the fluid, the equation of state relates the thermodynamic quantities within the conservation equations, notably temperature T, pressure P, and density ρ or specific volume v. The simplest equation of state is the ideal gas model with constant specific heat. For many applications the ideal gas law suffices, though it is not able to predict vapor-liquid equilibrium as well as accurate thermodynamic properties in the vicinity of the saturation curve or the liquid state. Van der Waals extended the ideal gas law by adding co-volume and intermolecular forces [1], this equation of state defined by van der Waals is capable of describing liquid and vapor states. After van der Waals, more complex equations of state followed and the accuracy of equations of state greatly improvement. The equations of state were also extended to describe thermodynamic properties of multicomponent fluids. In this section the thermodynamics of multicomponent fluids is elaborated as well as the multicomponent equations of state used in this work.

First, the vapor-liquid equilibrium behavior of mixtures is explained and the numerical tools used for the calculation are elaborated. Secondly the theory behind the determination of the critical point of mixtures is explained as well as the methodology to determine the mixtures critical point. Finally the thermodynamic models for multicomponent fluids used in this work are elaborated which consist of the polytropic van der Waals equation of state, the Peng-Robinson equation of state, and the multiparameter Helmholtz energy equation of state.

2.2 Vapor-liquid equilibrium binary mixture

Accurate and robust calculations of the vapor-liquid equilibrium (VLE) curve of multicomponent mixtures is important for the use of models predicting the mixture properties. Calculating the vapor-liquid equilibrium of a mixture from an equation of state is more complicated than for a pure component and becomes even more difficult near the critical region. This is because besides equality of temperature and pressure in both coexisting phases, chemical potential for all components in the mixture should be the same in both coexisting phases. These conditions can be expressed as

$$T_\mathrm{l} = T_\mathrm{v} \quad \text{and} \quad P_\mathrm{l} = P_\mathrm{v}, \tag{2.1}$$

where T is the temperature, P the pressure and l and v represent the liquid and vapor phase respectively. The condition for equilibrium of chemical potential is given as [2, 3]

$$\mu_i^\mathrm{l}(T,P,x_i) = \mu_i^\mathrm{v}(T,P,y_i) \quad i = 1,2...C, \tag{2.2}$$

here x_i is the liquid molar composition and y_i is the vapor molar composition. The chemical potential of component i is defined as μ_i and C is the total number of components of the mixture.

The phase equilibrium problem from Eqs. (2.1) and (2.2) is shown in Fig. 2.1. The pressure for an isothermal process, or temperature for an isobaric process, are not constant during the transition from the liquid to the vapor phase, unlike a pure fluid. Following the isobar at 5 bar from (1)–(2)–(3), it can be seen that the temperature differs from the vapor and liquid saturation line. If the mixture is in the two-phase region the coexisting liquid and vapor phase have the same temperature and pressure, but different composition between the vapor and liquid phase. The coexisting liquid and vapor phase are joined by a horizontal tie line, as is seen at point 2 in Fig. 2.1 with an overall molar fraction, $z_{\mathrm{MM}} = 0.5$, of the first component hexamethyldisiloxane (MM) and overall molar fraction, $z_{\mathrm{MD_4M}} = 0.5$, of the second component tetradecamethylhexasiloxane ($\mathrm{MD_4M}$). The liquid phase composition of the first component MM is, $x_{\mathrm{MM}} \approx 0.25$ and the vapor phase composition, $y_{\mathrm{MM}} \approx 0.75$. During the phase transition the liquid and vapor phase compositions are continuously changing from the liquid side to the vapor side or visa versa. This continuously change in composition results in a changing temperature for an isobaric process and changing pressure for isothermal process during the phase transition. The change in composition and temperature during an isobaric phase transition process is shown in Fig. 2.1. For a mixture the liquid side of the saturation curve is called the bubble point curve and the vapor side of the saturation curve is the dew point curve. In Fig. 2.1 the dew point curve is indicated with the red line and the bubble point curve with the blue line. The dew point curve and bubble point curve are also present in the P-T plane for a mixture, for pure fluids the temperature and pressure are constant during the phase transition which results in a single line. Adding mixtures into the P-T diagram will introduce bubble and dew curves, this results in a phase envelope for mixtures in the P-T-z plane. Fig. 2.2 shows a cross-section representation of the phase envelope in the P-T plane. By changing the composition the shape of the saturation curve, including the bubble and dew curve, of the mixtures changes.

In this research the method of Michelsen [8] is used to accurately calculate the phase envelope for VLE implemented in FluidProp [9] and the scientific program REFPROP [4]. This method also gives satisfactory results for VLE calculation near the critical region.

2.3 Critical point of a multicomponent mixture

Determination of the critical points in pure fluids and mixtures are important in investigating phase behavior and VLE calculations.

As is well known, pure components only have one critical point, defined in terms of the critical temperature T_{c}, pressure P_{c}, and specific volume v_{c}. The stability criteria used to compute the pure component critical point are based on mechanical

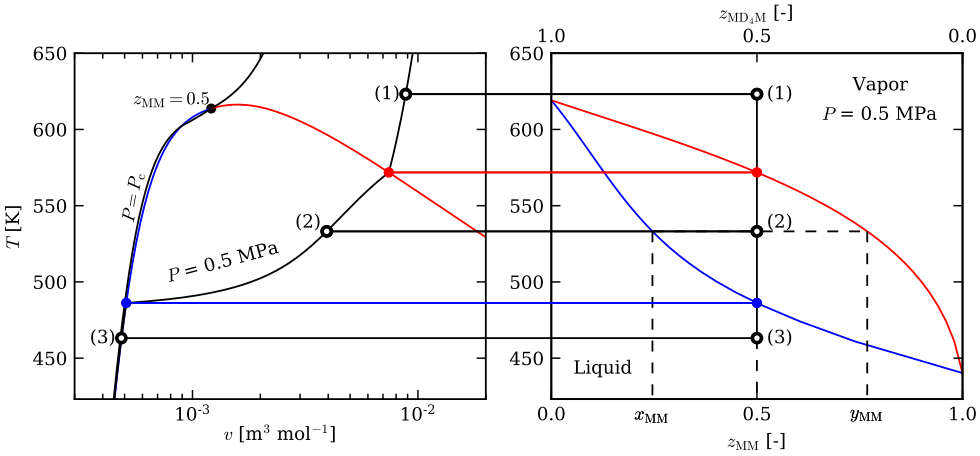

Figure 2.1: Exemplary thermodynamic diagram for binary mixture MM–MD_4M with composition MM: $z_{MM} = 0.5$ and MD_4M: $z_{MD_4M} = 0.5$. The T-v diagram is for the equimolar composition. The blue line is the bubble curve (–) and the red line the dew curve (–). The solid black bullet is the critical point (•). Line (1)–(2)–(3) gives an isobaric process for a mixture with equimolar overall composition. Generated with the Helmholtz energy equation of state implemented in REFPROP [4] and state-of-the-art coefficients are derived by Thol et al. [5] for MM and König et al. [6] for MD_4M. The applied mixture model is the GERG-2008 mixture formulation [7] with estimated mixing parameters.

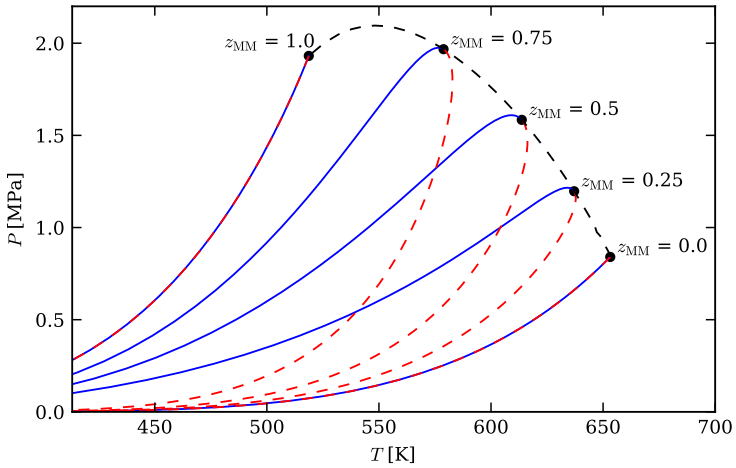

Figure 2.2: P-T thermodynamic diagram showing constant composition cross-sections of the phase envelope for the binary mixture MM–MD_4M for composition z_{MM} = 0, 0.25, 0.5, 0.75, 1. The solid blue line is the bubble curve (–) and the dashed red line the dew curve (–). The red/blue lines are the pure components saturation lines (– –). The bullet indicate the mixture critical points (•) and the dashed black line is the critical locus (– –). Generated with the Helmholtz energy equation of state implemented in REFPROP [4].

stability[2, 3] where

$$\left(\frac{\partial P}{\partial v}\right)_T = 0 \quad \text{and} \quad \left(\frac{\partial^2 P}{\partial v^2}\right)_T = 0, \tag{2.3}$$

here P is the pressure, T the temperature, and v the specific volume.

For mixtures it is possible to have a single solution, multiple solutions or no solution at all for the critical point [8, 10]. Several methods are available in the literature for the calculation of the mixture critical point [3]. The most thermodynamic consistent method for the determination of the true critical point of the mixture is called the rigorous method [3, 10]. The rigorous method is based on the criterion established for a binary mixture by Gibbs [11]:

$$\left(\frac{\partial^2 G}{\partial z_1^2}\right)_{T,P} = 0 \quad \text{and} \quad \left(\frac{\partial^3 G}{\partial z_1^3}\right)_{T,P} = 0, \tag{2.4}$$

where G is the molar Gibbs energy, T is the temperature, P is the pressure, and z_1 is the mole fractions of the first component in the mixture.

The first major attempt for multicomponent mixtures was done by Peng et al. [12]. The pure component critical point is based on isothermal compressibility, for mixtures the critical point criterion involves derivatives of energy functions with respect to number of moles of the components.

The criticality conditions defining the location of the critical point can be expressed through the use of Legendre transform [13] The advantage of the Legendre transform is that it allows the user to straightforwardly express the critical conditions as determinants of matrices. There are several equivalent sets of independent variables in the transformation, and as demonstrated by Akasaka [14], the use of the amount of substance (number of moles) of the components (as opposed to other more readily handled independent variables) as independent variables yields a more well-scaled set of matrices. This in turn allows for a more reliable solution method.

The Gibbs criterion can be expressed in the alternative form by the Legendre transform [13]. The criticality conditions that must be fulfilled at the critical point for n-component mixtures are $\mathfrak{L}_i = 0$ and $\mathfrak{M}_i = 0$ and have the form of the following two determinants [10, 14]

$$\mathfrak{L}_i = \begin{vmatrix} y^{(i)}_{i+1,i+1} & \cdots & y^{(i)}_{i+1,n+1} \\ y^{(i)}_{i+2,i+1} & \cdots & y^{(i)}_{i+2,n+1} \\ \vdots & \ddots & \vdots \\ y^{(i)}_{n+1,i+1} & \cdots & y^{(i)}_{n+1,n+1} \end{vmatrix} = 0, \qquad \mathfrak{M}_i = \begin{vmatrix} y^{(i)}_{i+1,i+1} & \cdots & y^{(i)}_{i+1,n+1} \\ y^{(i)}_{i+2,i+1} & \cdots & y^{(i)}_{i+2,n+1} \\ \vdots & \ddots & \vdots \\ y^{(i)}_{n,i+1} & \cdots & y^{(i)}_{n,n+1} \\ \dfrac{\partial \mathfrak{L}_i}{\partial x_{i+1}} & \cdots & \dfrac{\partial \mathfrak{L}_i}{\partial x_{n+1}} \end{vmatrix} = 0, \tag{2.5}$$

where the entries of the matrices $y^{(i)}$ is the i-th Legendre transform and $y^{(i)}_{k,l}$ is defined as

$$y^{(i)}_{k,l} = \frac{\partial^2 y^{(i)}}{\partial x_k \partial x_l}, \tag{2.6}$$

here x and y indicate independent variables, not a mole fractions.

By expressing the criticality conditions in Legendre form it is possible to make a preferable form of the critical criterion. If the basic function $y^{(0)}$ is taken as the internal energy E the Legendre transforms can be expressed as [15]

$$y^{(0)} = E = f_0(S,\, V,\, n_i), \tag{2.7}$$

$$y^{(1)} = H = f_1(S,\, P,\, n_i), \tag{2.8}$$

$$y^{(1)} = A = f_1(T,\, V,\, n_i), \tag{2.9}$$

$$y^{(2)} = G = f_2(T,\, P,\, n_i), \tag{2.10}$$

where S is the entropy, V is the volume, H is the enthalpy, A the Helmholtz energy, and n_i the number of moles of component i. By changing the order of the independent variables in the basic function $y^{(0)}$ the entries in the matrices can be written as partial differential equation with respect to the number of moles of the components [15].

Since typical equations of state have T, v, and $\bar{z}$ as independent variables, the criterion established by Gibbs in Eq. (2.4) are not practical. To make the Gibbs criteria suitable for use, the partial derivatives of the molar Gibbs energy are now expressed in terms of the partial derivatives of the molar Helmholtz energy with respect to the number of moles of the components using the Legendre transform. The determinants Eq. (2.5) can now be expressed with the Helmholtz energy as

$$\mathfrak{L}_1 = \begin{vmatrix} A_{11} & \dots & A_{1C} \\ A_{21} & \dots & A_{2C} \\ \vdots & \ddots & \vdots \\ A_{C1} & \dots & A_{CC} \end{vmatrix} = 0, \qquad \mathfrak{M}_1 = \begin{vmatrix} A_{11} & \dots & A_{1C} \\ A_{21} & \dots & A_{2C} \\ \vdots & \ddots & \vdots \\ A_{(C-1)1} & \dots & A_{(C-1)C} \\ \dfrac{\partial \mathfrak{L}_1}{\partial n_1} & \dots & \dfrac{\partial \mathfrak{L}_1}{\partial n_C} \end{vmatrix} = 0, \tag{2.11}$$

where the entries in the matrices are described by Heidemann et al. [16] and given by

$$A_{ij} = \frac{1}{RT}\left(\frac{\partial^2 A}{\partial n_j \partial n_i}\right)_{T,V} = \left(\frac{\partial \ln f_i}{\partial n_j}\right)_{T,V,n_i}, \tag{2.12}$$

and

$$A_{ijk} = \frac{1}{RT}\left(\frac{\partial^3 A}{\partial n_j \partial n_i \partial n_k}\right)_{T,V} = \left(\frac{\partial^2 \ln f_i}{\partial n_k \partial n_j}\right)_{T,V,n_i}, \tag{2.13}$$

here f_i is the fugacity of the i-th component. The same results are obtained in Eqs. (2.12) and (2.13) whatever the order of differentiation is

$$\left(\frac{\partial \ln f_i}{\partial n_j}\right)_{T,V,n_i} = \left(\frac{\partial \ln f_j}{\partial n_i}\right)_{T,V,n_j}, \tag{2.14}$$

and

$$\left(\frac{\partial^2 \ln f_i}{\partial n_k \partial n_j}\right)_{T,V,n_i} = \left(\frac{\partial^2 \ln f_j}{\partial n_k \partial n_i}\right)_{T,V,n_j} = \left(\frac{\partial^2 \ln f_k}{\partial n_i \partial n_j}\right)_{T,V,n_k}, \tag{2.15}$$

which reduces computational effort through efficient calculation of the entries in the matrix by calculating the upper triangular part of the matrix and mirroring the data into the lower part of the matrix.

Various methods have been developed for solving the criticality conditions based on the rigorous method. The first method applied in this research for the direct calculation of the critical point is developed by Heidemann et al. [16] who applied the criticality conditions based on the Helmholtz energy derivatives of the rigorous method. The critical points are assumed to be stable and the mixtures have only one critical point. Another method used in this research implemented in REFPROP [4] is developed by Michelsen [17]. More advanced methods that find all critical points and asses the critical point stability are described by Gernert et al. [18] and Bell et al. [10]. The book of Michelsen et al. [19] provides an overview of the state-of-the-art of calculation of critical points.

2.4 Thermodynamic models

In this work three thermodynamic models for pure fluids and multicomponent mixtures are used; the polytropic van der Waals equation of state, Peng-Robinson equation of state, and the Helmholtz energy equation of state. The equations of state are elaborated in this section.

2.4.1 Polytropic van der Waals equation of state

The van der Waals equation of state (VdW-EOS) is the simplest cubic equation of state and gives quantitative inadequate predictions of thermodynamic properties but qualitative good.

The pressure and internal energy equation of state stated by van der Waals are [2]

$$P(T,v) = \frac{RT}{v-b} - \frac{a}{v^2}, \tag{2.16}$$

$$e(T,v) = \int_{T_0}^{T} c_v^{\mathrm{o}}(T)dT - \frac{a}{v}, \tag{2.17}$$

and the compressibility factor Z is defined as,

$$Z = \frac{Pv}{RT}. \tag{2.18}$$

In the above equations $R = 8.3144598$ J mol^{-1} K^{-1} is the universal gas constant, P the pressure, T the temperature, and v the specific volume. The fluid-dependent parameter a is related to the long range attractive intermolecular forces and b accounts for the short range repulsive intermolecular forces. The VdW-EOS can be derived from statistical mechanics, using an intermolecular potential and having a repulsive and an attractive contribution [20].

Using the stability conditions at the critical point for pure fluids, given in Section 2.3, the fluid-dependent parameters a and b can be expressed by the universal gas constant R, critical pressure P_c, and temperature T_c [2].

$$a = \frac{27}{64}\frac{R^2 T_c^2}{P_c}, \quad b = \frac{1}{8}\frac{RT_c}{P_c}. \tag{2.19}$$

The molar specific internal energy is given by e, where c_v^o is the ideal gas isochoric specific heat. In the case of the VdW-EOS, following from the thermodynamic relation $c_v = (\partial e/\partial T)_v$, the isochoric specific heat is only a function of temperature T and therefore, the function $c_v(T) = \int_{T_0}^{T} c_v^o(T)dT$ is the same in the ideal gas state and in non-ideal states. In this work the polytropic VdW-EOS is used, the polytropic assumptions implies that the isochoric specific heat c_v is constant. The correctness of this approximation in the evaluation of thermodynamic properties in the ideal-gas state has been discussed by Thompson et al. [21] and Guardone et al. [22].

According to the energy equipartition principle [23, 24] the isochoric specific heat and number of active degrees of freedom for the polytropic VdW-EOS are related. Considering only translational, rotational, and vibrational degrees of freedom the number of total available degrees of freedom depends on the number of atoms constituting the molecule. At a given temperature, each fully activated degree of freedom contributes $R/2$ to the overall value of the isochoric specific heat, this gives the following relation between the active degrees of freedom and the isochoric specific heat [25] for the polytropic VdW-EOS

$$c_v = c_v^o = \frac{NR}{2}, \tag{2.20}$$

here N the number of active degrees of freedom. Under the polytropic VdW-EOS the isochoric specific heat is constant and therefrom the active degrees of freedom of the fluid is determined. For the polytropic assumption the specific heat and so the active degrees of freedom are calculated at a given temperature.

Attractive forces, repulsive forces and number of degrees of freedom can be related in a complicated way to molecular complexity. The molecular weight and number of active degrees of freedom increase with molecular complexity. The attractive

and repulsive force contribution a and b respectively provide a measure of the intermolecular forces per unit molar. Deviation of the compressibility factor Z from unity and therefore from ideal gas behavior is due to the action of attractive and repulsive forces.

For mixtures the fluid properties also depend on the composition $\bar{z}$, as extra independent variable. The polytropic VdW-EOS for mixtures with composition dependent parameters having the subscript m becomes,

$$P_{\mathrm{m}}(T,v,\bar{z}) = \frac{RT}{v-b_{\mathrm{m}}(\bar{z})} - \frac{a_{\mathrm{m}}(\bar{z})}{v^2}, \tag{2.21}$$

$$e_{\mathrm{m}}(v,\bar{z}) = c^{\mathrm{o}}_{v,\mathrm{m}}(\bar{z}) - \frac{a_{\mathrm{m}}(\bar{z})}{v}. \tag{2.22}$$

The parameters a_{m} and b_{m} from the mixture VdW-EOS are calculated from the van der Waals one-fluid mixing rule. The complete mixture equation of state from the van der Waals equation of state with one-fluid mixing rules will be abbreviated by VdW-OF.

The van der Waals one-fluid mixing rule is a combination of the pure components parameters a and b from Eq. (2.19) and mixture composition $\bar{z}$, in molar quantities. Leland et al. [26–28] were able to re-derive the van der Waals one-fluid mixing rules from statistical mechanics theory of radial distribution functions. The statistical mechanics arguments state that the attractive force mixing rule is proportional to the molecular volume times the molecular energy and the repulsive force to molecular volume. As a result, the re-derived mixing rules are in the same form as proposed by van der Waals [29].

$$a_{\mathrm{m}}(\bar{z}) = \sum_{j=1}^{C}\sum_{i=1}^{C} z_i z_j a_{ij}, \tag{2.23}$$

$$b_{\mathrm{m}}(\bar{z}) = \sum_{j=1}^{C}\sum_{i=1}^{C} z_i z_j b_{ij}. \tag{2.24}$$

The cross parameters a_{ij} and b_{ij}, also known as unlike interaction parameters and subscript i and j indicate the pure component indices within the mixture. The cross parameters are related to the Lorentz-Berthelot combining rules [26].

$$a_{ij} = (1-k_{ij})\sqrt{a_i a_j}, \tag{2.25}$$

$$b_{ij} = (1-l_{ij})\frac{(b_i+b_j)}{2}, \tag{2.26}$$

where k_{ij} and l_{ij} are the binary interaction parameters, obtained by fitting measured phase equilibrium and volumetric data.

The binary interaction parameters k_{ij} and l_{ij} are neglected for the polytropic van der Waals model. The binary interaction parameters are neglected due to their direct relation to experimental data. In this research, the basic polytropic van der Waals model is used, which is characterized by a direct relation between the equation of state parameters and the molecular force features. Therefore, the following a_{m} and b_{m} parameters are found for a binary mixture,

$$a_{\mathrm{m}}(\bar{z}) = z_1^2 a_1 + 2z_1 z_2 \sqrt{a_1 a_2} + z_2^2 a_2, \tag{2.27}$$

$$b_{\mathrm{m}}(\bar{z}) = z_1 b_1 + z_2 b_2. \tag{2.28}$$

The binary mixture molecular weight M_{m}, is calculated as a weighted average between the pure components molecular weights M,

$$M_{\mathrm{m}}(\bar{z}) = \sum_{i=1}^{C} z_i M_i, \tag{2.29}$$

and for a binary mixture this gives

$$M_{\mathrm{m}}(\bar{z}) = z_1 M_1 + z_2 M_2. \tag{2.30}$$

The ideal gas isochoric specific heat for mixtures using the polytropic van der Waals model is calculated as the weighted average between the pure components ideal gas isochoric specific heats from Eq. (2.20) [2] and is defined as

$$c^{\mathrm{o}}_{v,\mathrm{m}}(\bar{z}) = \sum_{i=1}^{C} z_i c^{\mathrm{o}}_{v,i} = \sum_{i} z_i \frac{N_i R}{2}. \tag{2.31}$$

Because the active number of degrees of freedom N, is derived from the ideal gas isochoric specific heat Eq. (2.20), the binary mixture active degrees of freedom, N_{m}, is also calculated as the weighted average between the pure components

$$N_{\mathrm{m}}(\bar{z}) = \sum_{i=1}^{C} z_i N_i, \tag{2.32}$$

and for a binary mixtures this results in

$$N_{\mathrm{m}}(\bar{z}) = z_1 N_1 + z_2 N_2. \tag{2.33}$$

2.4.2 Peng-Robinson equation of state

The Peng-Robinson equation of state (PR-EOS) [30] is a modified cubic equation of state based on the van der Waals equation of state. To this day the Peng-Robinson equation of state is still widely used due to its reasonable prediction, simplicity, and

computationally efficiency compared with the Helmholtz energy equation of state [31]. The pressure as a function of temperature and specific volume of the Peng-Robinson equation of state for pure and multicomponent fluids is defined as

$$P_{\mathrm{m}}(T,v,\bar{z}) = \frac{RT}{v-b_{\mathrm{m}}(\bar{z})} - \frac{a_{\mathrm{m}}(T,\bar{z})}{v(v+b_{\mathrm{m}}(\bar{z}))+b_{\mathrm{m}}(\bar{z})(v-b_{\mathrm{m}}(\bar{z}))}, \tag{2.34}$$

$$e_{\mathrm{m}}(T,v,\bar{z}) = c^{\mathrm{o}}_{v,\mathrm{m}}(T,\bar{z}) + \frac{T\left(\frac{da_{\mathrm{m}}(T,\bar{z})}{dT}\right) - a_{\mathrm{m}}(T,\bar{z})}{2\sqrt{2}b_{\mathrm{m}}(\bar{z})} \ln\left[\frac{b_{\mathrm{m}}(\bar{z})(1+\sqrt{2})-v}{b_{\mathrm{m}}(\bar{z})(1-\sqrt{2})-v}\right], \tag{2.35}$$

where P is the pressure, $R = 8.3144598$ J mol^{-1} K^{-1} is the universal gas constant, T is the temperature and v is the specific volume. The fluid parameter a depends on the temperature and is given by

$$a(T) = 0.45724\frac{R^2T_{\mathrm{c}}^2}{P_{\mathrm{c}}}\alpha(T), \tag{2.36}$$

$$\sqrt{\alpha} = 1+\kappa\left(1-\sqrt{\frac{T}{T_{\mathrm{c}}}}\right), \tag{2.37}$$

$$\kappa = 0.37464 + 1.54226\omega - 0.26992\omega^2, \tag{2.38}$$

where the coefficient ω is the acentric factor and depends on the fluid under consideration, T_{c} is the critical temperature, and P_{c} is the critical temperature of the fluid. The fluid parameter b is given by

$$b = 0.07780\frac{RT_{\mathrm{c}}}{P_{\mathrm{c}}}. \tag{2.39}$$

The Peng-Robinson equation is extended to mixtures by introducing mixing rules, which make the fluid parameters a and b composition dependent. In this work the van der Waals one-fluid mixing rules are implemented and the composition dependent parameters a and b are in the form

$$a_{\mathrm{m}}(T,\bar{z}) = \sum_{j=1}^{C}\sum_{i=1}^{C} z_i z_j a_{ij}(T), \tag{2.40}$$

$$b_{\mathrm{m}}(\bar{z}) = \sum_{j=1}^{C}\sum_{i=1}^{C} z_i z_j b_{ij}, \tag{2.41}$$

where z is the molar composition of the mixture and the cross parameters a_{ij} and b_{ij} are obtained from a set of combining rules. The subscript i and j indicate the pure component indices within the mixture and C is the total number of components in

the mixture. The cross parameters can be related to the Lorentz-Berthelot combining rules [26] and are given by

$$a_{ij}(T) = (1-k_{ij})\sqrt{a_i(T)a_j(T)}, \tag{2.42}$$

$$b_{ij} = (1-l_{ij})\frac{b_i+b_j}{2}, \tag{2.43}$$

where a_i, a_j, b_i, and b_j are the pure component fluid parameters calculated from Eqs. (2.36) and (2.39). k_{ij} and l_{ij} are the binary interaction parameters obtained by fitting measured phase equilibrium and volumetric data. In this work the binary interaction parameter l_{ij} is set to zero for the Peng-Robinson equation of state.

The ideal gas isochoric specific heat for mixtures using the Peng-Robinson equation of state is calculated as the weighted average between the pure components ideal gas isochoric specific heats [2] as

$$c^{\mathrm{o}}_{v,\mathrm{m}}(T,\bar{z}) = \sum_{i=1}^{C} z_i \left[\int_{T_0}^{T} c^{\mathrm{o}}_{v,i}(T)dT\right] \tag{2.44}$$

2.4.3 Helmholtz energy equation of state

The Helmholtz energy equation of state in non-dimensional form is described by Span [31]. The state-of-the-art definition of the Helmholtz energy equation of state for pure components and mixtures is given by the GERG-2008 [7] as

$$\frac{a(T,\rho,\bar{z})}{RT} = \alpha(\tau,\delta,\bar{z}) = \alpha^{\mathrm{o}}(\tau,\delta,\bar{z}) + \alpha^{\mathrm{r}}(\tau,\delta,\bar{z}), \tag{2.45}$$

where a is the molar Helmholtz energy, $R = 8.3144598$ J mol^{-1} K^{-1} is the universal molar gas constant, T the temperature, ρ the molar density and $\bar{z}$ the molar composition. The dimensionless Helmholtz energy, α, is the sum of an ideal part α^{o} and a residual part α^{r} where τ is the reciprocal reduced mixture temperature and δ the reduced mixture density.

$$\tau = \frac{T_{\mathrm{r}}(\bar{z})}{T}, \quad \delta = \frac{\rho}{\rho_{\mathrm{r}}(\bar{z})}. \tag{2.46}$$

From the Helmholtz energy equation of state all other thermodynamic properties can be derived. For more information on calculating other thermodynamic properties from derivatives of the Helmholtz energy, see the work of Span [31].

The dimensionless form of the Helmholtz free energy for the ideal-gas state contribution of the mixture is given by

$$\alpha^{\mathrm{o}}(\tau,\delta,\bar{z}) = \sum_{i=1}^{C} z_i \left[\alpha^{\mathrm{o}}_i(\tau_i,\delta_i) + \ln z_i\right], \tag{2.47}$$

where C is the number of components in the mixture, α_i^{o} the dimensionless form of the Helmholtz energy ideal-gas state of component i, and z_i the mole fraction of the mixture component i. The term $z_i \ln z_i$ accounts for the entropy of mixing.

The residual part α^{r} of the dimensionless Helmholtz energy model of a multicomponent fluid is given by

$$\alpha^{\mathrm{r}}(\tau,\delta,\bar{z}) = \sum_{i=1}^{C} z_i \alpha_i^{\mathrm{r}}(\delta,\tau) + \Delta\alpha^{\mathrm{r}}(\delta,\tau,\bar{z}), \tag{2.48}$$

where α_i^{r} is the residual part of the reduced Helmholtz energy model of component i and $\Delta\alpha^{\mathrm{r}}$ the departure function.

The temperature dependent ideal-gas contribution of the dimensionless Helmholtz energy equation of state is derived from the ideal gas isobaric heat capacity c_p^{o} correlation with reduced variables

$$\frac{c_p^{\mathrm{o}}}{R} = n_0^* + \sum_{k=1}^{K_{\mathrm{Pol}}} n_k^* T^{t_k^*} + \sum_{k=1}^{K_{\mathrm{PE}}} m_k \left(\frac{\theta_k}{T}\right)^2 \frac{e^{(\theta_k/T)}}{\left(e^{(\theta_k/T)}-1\right)^2}, \tag{2.49}$$

by integrating the isobaric specific heat correlation twice with respect to τ and introducing

$$c_0 = n_0^* - 1,\ c_k = -n_k^* / \left(t_k^* \left(t_k^* + 1\right)\right) \cdot T_{\mathrm{r}}^{t_k},\ t_k = -t_k^*, \text{ and } \vartheta_k = \theta_k / T_{\mathrm{r}}, \tag{2.50}$$

the dimensionless form of the Helmholtz energy ideal-gas state of component i in the mixture from (2.47) becomes

$$\alpha_i^{\mathrm{o}}(\delta_i,\tau_i) = c_i^{\mathrm{II}} + c_i^{\mathrm{I}}\tau_i + c_{0,i}\ln\tau_i + \sum_{\mathrm{k}=1}^{K_{\mathrm{Pol},i}} c_{i,k}\tau_i^{t_{i,k}} + \sum_{k=1}^{K_{\mathrm{PE},i}} m_{i,k} \ln\left[1 - e^{\left(-\vartheta_{i,k}\tau_i\right)}\right] + \ln\delta_i, \tag{2.51}$$

here c^{I} and c^{II} are the integration constants and can be chosen arbitrarily, τ_i and δ_i are the reduced temperature and density of component i respectively. The reducing parameters for the ideal-gas contribution are the critical parameters, $\rho_{\mathrm{c},i}$ and $T_{\mathrm{c},i}$ of the pure components in the mixture. The coefficients $c_{0,i}$, $c_{i,k}$, and $m_{i,k}$ as well as the exponents $t_{i,k}$, and $\vartheta_{i,k}$ depend on the components under consideration in the mixture.

The residual part of the reduced Helmholtz energy of the mixture is given by

$$\alpha^{\mathrm{r}}(\delta,\tau,\bar{z}) = \sum_{i=1}^{C} z_i \alpha_i^{\mathrm{r}}(\delta,\tau) + \sum_{i=1}^{C-1}\sum_{j=i+1}^{C} z_i z_j F_{ij} \alpha_{ij}^{\mathrm{r}}(\delta,\tau). \tag{2.52}$$

The reduced residual Helmholtz energy of each component in the mixture depends on the reduced variables δ and τ, the departure function $\Delta\alpha^{\mathrm{r}}(\delta,\tau,\bar{z})$, which is the double summation in Eq. (2.52), depends on the reduced variables and the composition of the mixture $\bar{z}$. The purpose of the departure function is to improve the

accuracy of the mixture model of non-ideal mixtures in situation where fitting the parameters of the reducing functions to experimental data does not provide a sufficiently accurate result. This means the departure function is not always developed for the Helmholtz energy equation of state for mixtures. The departure function is set to zero, when fitting the reducing functions give sufficiently accurate results or there is not enough experimental data available.

The residual part of component i in the mixture is

$$\begin{aligned}\alpha_i^{\mathrm{r}}(\delta,\tau) &= \alpha_{\mathrm{Pol},i}^{\mathrm{r}}(\delta,\tau)+\alpha_{\mathrm{Exp},i}^{\mathrm{r}}(\delta,\tau)+\alpha_{\mathrm{GBS},i}^{\mathrm{r}}(\delta,\tau)\\ &= \sum_{k=1}^{K_{\mathrm{Pol},i}} n_{i,k}\delta^{d_{i,k}}\tau^{t_{i,k}} + \sum_{k=K_{\mathrm{Pol},i}+1}^{K_{\mathrm{Pol},i}+K_{\mathrm{Exp},i}} n_{i,k}\delta^{d_{i,k}}\tau^{t_{i,k}}e^{\left(-\delta^{c_{i,k}}\right)}\\ &+ \sum_{k=K_{\mathrm{Pol},i}+K_{\mathrm{Exp},i}+1}^{K_{\mathrm{Pol},i}+K_{\mathrm{Exp},i}+K_{\mathrm{GBS},i}} n_{i,k}\delta^{d_{i,k}}\tau^{t_{i,k}}e^{\left[-\eta_{i,k}\left(\delta-\varepsilon_{i,k}\right)^2-\beta_{i,k}\left(\delta-\gamma_{i,k}\right)^2\right]},\end{aligned} \tag{2.53}$$

the respective values for the coefficients $n_{i,k}$ and the exponents $d_{i,k}$, $t_{i,k}$, $c_{i,k}$, $\eta_{i,k}$, $\varepsilon_{i,k}$, and $\gamma_{i,k}$ depend on the fluid under consideration.

The function α_{ij}^{r}, which is part of the departure function $\Delta\alpha^{\mathrm{r}}$ only depends on the reduced mixture variables τ and δ and is given by

$$\alpha_{ij}^{\mathrm{r}}(\delta,\tau) = \sum_{k=1}^{K_{\mathrm{Pol},ij}} n_{ij,k}\delta^{d_{ij,k}}\tau^{t_{ij,k}} + \sum_{k=K_{\mathrm{Pol},ij}+1}^{K_{\mathrm{Pol},ij}+K_{\mathrm{Exp},ij}} n_{ij,k}\delta^{d_{ij,k}}\tau^{t_{ij,k}}e^{\left[-\eta_{ij,k}\left(\delta-\varepsilon_{ij,k}\right)^2-\beta_{ij,k}\left(\delta-\gamma_{ij,k}\right)\right]}, \tag{2.54}$$

where α_{ij}^{r} is developed for either a specific binary mixture or a certain group of binary mixtures, with the coefficients $n_{ij,k}$ and exponents $d_{ij,k}$, $t_{ij,k}$, $\eta_{ij,k}$, $\varepsilon_{ij,k}$, and $\gamma_{ij,k}$ depending on the binary mixture under consideration. The factor F_{ij} is set to unity if the departure function is developed for a specific binary mixture, F_{ij} is fitted to binary specific data for each mixture in the group of generalized binary mixtures. When there is no departure function developed, the factor F_{ij} is equal to zero.

The reduced mixture parameters τ and δ are calculated from Eq. (2.46) through the composition-dependent reducing function for mixture density and temperature. The reducing parameters for the mixture density, T_{r} and $1/\rho_{\mathrm{r}}$ can then be given in common form

$$\frac{1}{\rho_{\mathrm{r}}(\bar{z})} = \sum_{i=1}^{C} z_i\frac{1}{\rho_{\mathrm{c},i}} + \sum_{i=1}^{C-1}\sum_{j=1}^{C} 2x_ix_j\beta_{v,ij}\gamma_{v,ij}\cdot\frac{x_i+x_j}{\beta_{v,ij}^2x_i+x_j}\cdot\frac{1}{8}\left(\frac{1}{\rho_{\mathrm{c},i}^{1/3}}+\frac{1}{\rho_{\mathrm{c},j}^{1/3}}\right)^3, \tag{2.55}$$

and the mixture temperature

$$T_{\mathrm{r}}(\bar{z}) = \sum_{i=1}^{C} z_iT_{\mathrm{c},i} + \sum_{i=1}^{C-1}\sum_{j=1}^{C} 2x_ix_j\beta_{T,ij}\gamma_{T,ij}\cdot\frac{x_i+x_j}{\beta_{T,ij}^2x_i+x_j}\cdot\left(T_{\mathrm{c},i}T_{\mathrm{c},j}\right)^{0.5}. \tag{2.56}$$

The binary parameters $\beta_{v,ij}$ and $\gamma_{v,ij}$ in Eq. (2.55) and $\beta_{T,ij}$ and $\gamma_{T,ij}$ in Eq. (2.56) are fitted to data for binary mixtures.

References

[1] J. D. van der Waals. “Over de Continuiteit van den Gas- en Vloeistoftoestand”. PhD thesis. University of Leiden, 1873.

[2] S. I. Sandler. *Chemical, Biochemical, and Engineering Thermodynamics*. 4th ed. Wiley, 2006.

[3] B. E. Poling, J. M. Prausnitz, and J. O’Connel. *The Properties of Gases and Liquids*. 5th ed. McGraw-Hill, 2000.

[4] E. W. Lemmon, I. H. Bell, M. L. Huber, and M. O. McLinden. *NIST Standard Reference Database 23: Reference Fluid Thermodynamic and Transport Properties - REFPROP, Version 10*. 2018.

[5] M. Thol, F. Dubberke, G. Rutkai, T. Windmann, A. Köster, R. Span, and J. Vrabec. “Fundamental equation of state correlation for hexamethyldisiloxane based on experimental and molecular simulation data”. In: *Fluid Phase Equilib.* 418.Supplement C (2016). Special Issue covering the Nineteenth Symposium on Thermophysical Properties, pp. 133–151. ISSN: 0378-3812. DOI: 10.1016/j.fluid.2015.09.047.

[6] König and M. Thol. “Helmholtz equation of state for Dodecamethylpentasiloxane (MD_3M) and Tetradecamethylhexasiloxane (MD_4M)”. To be published. 2017.

[7] O. Kunz and W. Wagner. “The GERG-2008 Wide-Range Equation of State for Natural Gases and Other Mixtures: An Expansion of GERG-2004”. In: *Journal of Chemical & Engineering Data* 57.11 (2012), pp. 3032–3091. DOI: 10.1021/je300655b.

[8] M. L. Michelsen. “Calculation of phase envelopes and critical points for multicomponent mixtures”. In: *Fluid Phase Equilib.* 4.1 (1980), pp. 1–10. ISSN: 0378-3812. DOI: 10.1016/0378-3812(80)80001-X.

[9] P. Colonna and T. P. van der Stelt. *Fluidprop: A program for estimation of thermophysical properties of fluids*. Software. 2004. URL: http://www.FluidProp.com.

[10] I. H. Bell and A. Jäger. “Calculation of critical points from Helmholtz-energy-explicit mixture models”. In: *Fluid Phase Equilib.* 433 (2017), pp. 159–173. ISSN: 0378-3812. DOI: 10.1016/j.fluid.2016.10.030. URL: http://www.sciencedirect.com/science/article/pii/S0378381216305349.

[11] J. W. Gibbs. “On the Equilibrium of Heterogeneous substances”. In: *Am. J. Sci.* 3rd ser. 16 (1878). DOI: 10.2475/ajs.s3-16.96.441.

[12] D. Y. Peng and D. B. Robinson. “A rigorous method for predicting the critical properties of multicomponent systems from an equation of state”. In: *AIChE J.* 23.2 (1977), pp. 137–144. ISSN: 1547-5905. DOI: 10.1002/aic.690230202.

[13] R. C. Reid and B. L. Beegle. “Critical point criteria in legendre transform notation”. In: *AIChE J.* 23.5 (1977), pp. 726–732. ISSN: 1547-5905. DOI: 10.1002/aic.690230515.

[14] R. Akasaka. “Calculation of the critical point for mixtures using mixture models based on Helmholtz energy equations of state”. In: *Fluid Phase Equilib.* 263.1 (2008), pp. 102–108. ISSN: 0378-3812. DOI: 10.1016/j.fluid.2007.10.007. URL: http://www.sciencedirect.com/science/article/pii/S0378381207006553.

[15] J. W. Tester and M. Modell. *Thermodynamics and Its Applications*. 3rd ed. Prentice Hall, 1997.

[16] R. A. Heidemann and A. M. Khalil. “The Calculation of Critical Points”. In: *AIChE J.* 26.5 (1980), pp. 769–779. ISSN: 1547-5905. DOI: 10.1002/aic.690260510.

[17] M. L. Michelsen. "Calculation of critical points and phase boundaries in the critical region". In: *Fluid Phase Equilib.* 16.1 (1984), pp. 57–76. ISSN: 0378-3812. DOI: 10.1016/0378-3812(84)85021-9. URL: http://www.sciencedirect.com/science/article/pii/0378381284850219.

[18] J. Gernert, A. Jäger, and R. Span. "Calculation of phase equilibria for multi-component mixtures using highly accurate Helmholtz energy equations of state". In: *Fluid Phase Equilib.* 375 (2014), pp. 209–218. ISSN: 0378-3812. DOI: 10.1016/j.fluid.2014.05.012.

[19] M. L. Michelsen and J. M. Mollerup. *Thermodynamic Models: Fundamentals and Computational Aspects*. 2nd ed. Tie-Line Publications, 2007.

[20] D. A. McQuarrie. *Statistical Mechanics*. 1st. University Science Books, 1976. ISBN: 1891389157. URL: http://www.worldcat.org/isbn/1891389157.

[21] P. A. Thompson and K. C. Lambrakis. "Negative shock waves". In: *J. Fluid Mech.* 60.1 (1973), pp. 187–208. DOI: 10.1017/S002211207300011X.

[22] A. Guardone and B. M. Argrow. "Nonclassical gasdynamic region of selected fluorocarbons". In: *Phys. Fluids* 17.11 (2005), p. 116102. DOI: 10.1063/1.2131922.

[23] H. B. Callen. *Thermodynamics and an Introduction to Thermostatistics*. 2nd ed. Wiley, 1985.

[24] G. Emanuel. *Advanced Classical Thermodynamics*. AIAA Inc., 1987.

[25] P. Colonna and A. Guardone. "Molecular interpretation of nonclassical gas dynamics of dense vapors under the van der Waals model". In: *Phys. Fluids* 18.5, 056101 (2006). DOI: 10.1063/1.2196095.

[26] T. W. Leland and P. S. Chappelear. "The Corresponding States Principle A Review of Current Theory and Practice". In: *Industrial & Engineering Chemistry* 60.7 (1968), pp. 15–43. DOI: 10.1021/ie50703a005.

[27] T. W. Leland, J. S. Rowlinson, and G. A. Sather. "Statistical Thermodynamics of Mixtures of Molecules of Different Sizes". In: *Trans. Faraday Soc.* 64 (0 1968), pp. 1447–1460. DOI: 10.1039/TF9686401447.

[28] T. W. Leland, J. S. Rowlinson, G. A. Sather, and I. D. Watson. "Statistical thermodynamics of two-fluid models of mixtures". In: *Trans. Faraday Soc.* 65 (0 1969), pp. 2034–2043. DOI: 10.1039/TF9696502034.

[29] T. Y. Kwak and G. A. Mansoori. "Van der waals mixing rules for cubic equations of state. Applications for supercritical fluid extraction modelling". In: *Chem. Eng. Sci.* 41.5 (1986), pp. 1303–1309. ISSN: 0009-2509. DOI: 10.1016/0009-2509(86)87103-2.

[30] D. Y. Peng and D. B. Robinson. "A New Two-Constant Equation of State". In: *Industrial & Engineering Chemistry Fundamentals* 15.1 (1976), pp. 59–64. DOI: 10.1021/i160057a011.

[31] R. Span. *Multiparameter equations of state : an accurate source of thermodynamic property data*. Berlin; New York: Springer, 2000. ISBN: 9783540673118. URL: http://www.worldcat.org/search?qt=worldcat_org_all&q=3540673113.

CHAPTER 3

SPEED OF SOUND OF BINARY MIXTURES AND RELATION TO PURE COMPONENT PROPERTIES

The content of this chapter is in preparation for publication:

L. Keulen and A. Guardone. “Speed of sound of binary mixtures and relation to pure component properties”. In preparation for submission to: *Fluid Phase Equilibria*. 2018.

3.1 Introduction

A fundamental research on the speed of sound behavior of binary mixtures is conducted. The speed of sound is intimately connected with other thermodynamic properties and is essential in developing equations of state [1]. This means understanding the speed of sound of mixtures is of paramount importance, for the design of the power cycle as well as understanding the thermodynamic properties of the mixture working fluid. The speed of sound is a key thermodynamic property for the design of turbines, due to the possibility of shock-waves within the turbine.

This research focuses on the speed of sound of binary mixtures of linear siloxanes and perfluorocarbons. A detailed theoretical research is conducted on the speed of sound behavior of these mixtures based on the work by Guardone et al. [2] for pure components. The goal is to obtain a better qualitative understanding about the speed of sound of binary mixtures using molecular interpretation under the van der Waals model.

Linear siloxanes and perfluorocarbons also have a high interest due to their possibility to exhibit non-ideal fluid dynamics effects and possibly being Bethe-Zel'dovich Thompson fluids, which are expected to exhibit non-classical gas dynamics behavior in the single-phase vapor region near the vapor-liquid saturation curve [3]. The property that governs this behavior is the fundamental derivative of gas dynamics, which is a derivative of the speed of sound [4]. Guardone et al. [2] already investigated the possible non-classical behavior of vapor mixtures.

In this research the speed of sound behavior for binary mixtures of linear siloxanes and perfluorocarbons is investigated. Firstly, in Section 3.2 the speed of sound behavior for binary mixtures of linear siloxanes is qualitatively investigated using the polytropic van der Waals model. The speed of sound is made dimensionless to show the different contribution of the ideal gas part, repulsive forces, and attractive forces and the relation to the pure component properties for binary mixtures of linear siloxanes. Subsequently in Sections 3.3 and 3.4 the speed of sound behavior at the critical point for binary mixtures of linear siloxanes and perfluorocarbons is analyzed using the polytropic van der Waals model. In Section 3.5 the most accurate and state-of-the-art thermodynamic model, the Helmholtz energy model, is used to verify the speed of sound behavior for the binary mixtures of linear siloxanes and perfluorocarbons. Finally, in Section 3.6 the speed of sound is evaluated along the dew curve and critical isotherm for binary mixtures of linear siloxanes and perfluorocarbons.

3.2 Speed of sound for binary mixtures using polytropic van der Waals model

The polytropic van der Waals equation of state (VdW-EOS) described in Section 2.4.1 is used to evaluate the speed of sound of binary mixtures. In this study, the attention is shifted from the thermodynamic viewpoint to the molecular or microscopic one and

elaborate an explanation directly in terms of the basic molecular characteristics of the mixture, including vibrational degrees of freedom, intermolecular attractive/repulsive forces and interaction between components in the mixture. To this purpose, the polytropic van der Waals model, which is characterized by a direct relation between the equation of state parameters and the molecular features, is used to explain the physical mechanism acting at a molecular level on the speed of sound of molecular complex fluids. The polytropic van der Waals model is implemented into FluidProp [5] for the calculations in this work.

As it is well known, the thermodynamic (zero frequency) speed of sound approaches zero at the critical point [6]. Though thermodynamic models, being analytic functions, calculate the speed of sound at the critical point which gives a qualitative prediction of the speed of sound behavior of fluids. Because a qualitative investigation is conducted in this work, in the following the speed of sound values at the critical point are used to describe the speed of sound behavior upon mixing.

The expression for the speed of sound as a function of temperature and specific volume is derived from its definition

$$c^2(s,v) = -v^2 \left(\frac{\partial P}{\partial v}\right)_s = -v^2 \left[\left(\frac{\partial P}{\partial v}\right)_T - \frac{T}{c_v}\left(\frac{\partial P}{\partial T}\right)_v^2\right]. \tag{3.1}$$

Using the polytropic VdW model for pure components the speed of sound is derived as [7],

$$c^2(T,v) = \left[1+\frac{2}{N}\right] R_s T \left[\frac{v}{v-b}\right]^2 - \frac{2a}{v}\frac{1}{M}, \tag{3.2}$$

where $R_s = R/M$ is the specific gas constant.

The VdW-OF model for mixtures gives the following expression with composition dependent parameters for the speed of sound,

$$c_m^2(T,v,\bar{z}) = \left[1+\frac{2}{N_m}\right] R_m T \left[\frac{v}{v-b_m}\right]^2 - \frac{2a_m}{v}\frac{1}{M_m}, \tag{3.3}$$

where $R_m = \frac{R}{M_m}$ is the mixture specific gas constant.

The speed of sound, c, can be expressed as the sum of the contributions from the ideal gas speed of sound, c_{id}, and for the corrections related to the effects of both van der Waals forces, repulsive, δc_{rep} and attractive, δc_{att} defined by Colonna et al. [8] for pure components and defined for mixtures as follows

$$c_m^2 = c_{m,id}^2 + \delta c_{m,rep}^2 + \delta c_{m,att}^2. \tag{3.4}$$

The contributions of the ideal gas, attractive and repulsive forces are given as

$$c^2_{\mathrm{m,id}}(T,\bar{z}) = \left[1+\frac{2}{N_\mathrm{m}}\right] R_\mathrm{m} T > 0, \tag{3.5}$$

$$\delta c^2_{\mathrm{m,rep}}(T,v,\bar{z}) = c^2_{\mathrm{m,id}}(T,\bar{z}) b_\mathrm{m} \frac{2v-b_\mathrm{m}}{(v-b_\mathrm{m})^2} > 0, \tag{3.6}$$

$$\delta c^2_{\mathrm{m,att}}(v,\bar{z}) = -\frac{2a_\mathrm{m}}{v}\frac{1}{M_\mathrm{m}} < 0. \tag{3.7}$$

From Eqs. (3.5) to (3.7) it can be seen that the speed of sound for mixtures differs from the ideal gas model, in which the speed of sound is a function of temperature and composition only. Similarly to the pure fluid case, if the repulsive and attractive forces are accounted for the speed of sound also depends on the specific volume. The different contributions to the speed of sound in Eqs. (3.5) to (3.7) are shown in Fig. 3.1. Various compositions along the critical isotherm are plotted for a binary mixture of MM–MD_4M.

The ideal gas contribution is a function of temperature and composition. From the kinetic theory of gases the ideal gas contribution is related to molecular interaction associated with elastic collision between the pure components of the mixture. The molecular interaction increases with temperature for pure components and is independent of the specific volume. The ideal gas contribution scales with the mixing rules for molecular weight (Eq. (2.30)) and number of active degrees of freedom (Eq. (2.33)). The mixture molecular weight and active degrees of freedom are related to the linear combination of the active degrees of freedom and molecular weight of the pure components given in Eqs. (2.30) and (2.33). Thus the ideal gas contribution varies with composition, but it is constant along isotherms for fixed composition. Also the ideal gas contribution is always positive, because N_m, R_m and T cannot be negative. The ideal gas contribution to the speed of sound increases with increasing molecular complexity and weight of the mixture.

The repulsive force contribution is given by the ideal gas part and a repulsive component which depends on the constant b_m for mixtures (Eq. (2.28)) which is related to short range forces. This combination makes the repulsive contribution a function of temperature, specific volume and composition and has a positive contribution to the speed of sound. At given temperatures and specific volume the repulsive force contribution is higher than the ideal gas contribution, for all compositions. If the specific volume decreases the contribution increases. The limiting case, $v_\mathrm{r} \to b_\mathrm{r}$, corresponds to the highest possible density where no further compression is possible. The compressibility factor is zero and the speed of sound goes to infinity. The repulsive contribution to the speed of sound increases with increasing molecular complexity and weight of the mixture.

The attractive force contribution depends on the mixture constant a_m related to long range forces and is a function of specific volume and composition. The attrac-

tive force increases the compressibility of a fluid and therefore the speed of sound under the influence of attractive forces is lower than that of an ideal gas in the same thermodynamic state. The attractive force has a negative contribution to the speed of sound as seen in Fig. 3.1. Namely, the compressibility is increased by the occurrence of attractive forces. The attractive contribution to the speed of sound decreases with increasing molecular complexity and weight of the mixture.

Combining these three contributions gives the total speed of sound shown in Fig. 3.1. For pure components a minimum value of the speed of sound is attained at the critical point, where the compressibility diverges to infinity. This is due to the stability conditions stated for the pure component critical point, $(\partial P/\partial v)_T = 0$ and $(\partial^2 P/\partial v^2)_T = 0$. For mixtures this is not the case because the stability condition for the mixture critical point is different, see Section 2.3. At the mixture critical point the speed of sound is not zero and the compressibility does not go to infinity.

As seen in the insertion in Fig. 3.1, a detailed view of the critical region and critical points, the speed of sound does not reach the maximum value for the less complex pure component, but a maximum is observed for a combination of the pure components. This indicates a non-monotonic behavior of the speed of sound for changing composition. This behavior is remarkable because more complex molecules have a lower speed of sound [8], but a combination causes an increase of the speed of sound indicating the influence of the interaction between the two pure component molecules. This behavior of the binary mixture will be further analyzed in the following sections.

3.2.1 Non-dimensional form of the speed of sound for binary mixtures

The speed of sound equation is now made non-dimensional to analyze the influence of molecular complexity and composition. Temperature, pressure and specific volume are made non-dimensional by their mixture critical point properties as follows,

$$T_{\mathrm{r,m}} = \frac{T}{T_{\mathrm{c,m}}}, \quad P_{\mathrm{r,m}} = \frac{P}{P_{\mathrm{c,m}}}, \quad v_{\mathrm{r,m}} = \frac{v}{v_{\mathrm{c,m}}}, \tag{3.8}$$

where the critical properties are calculated using the stability criteria for mixtures given in Section 2.3 and implementation of the method developed by Heidemann et al. [9].

The mixture EOS parameters a_{m} and b_{m} are reduced as follows,

$$a_{\mathrm{r,m}} = \frac{a_{\mathrm{m}}}{P_{\mathrm{c,m}} v_{\mathrm{c,m}}^2}, \qquad b_{\mathrm{r,m}} = \frac{b_{\mathrm{m}}}{v_{\mathrm{c,m}}}. \tag{3.9}$$

Under the van der Waals approximation for pure components the reduced attractive and repulsive force parameters in Eq. (3.9) are hence constant, $a_{\mathrm{r}} = 3$ and $b_{\mathrm{r}} = 1/3$, and therefore independent from the fluid under consideration. For the mixture parameters this does not hold. The parameters depend on the composition and

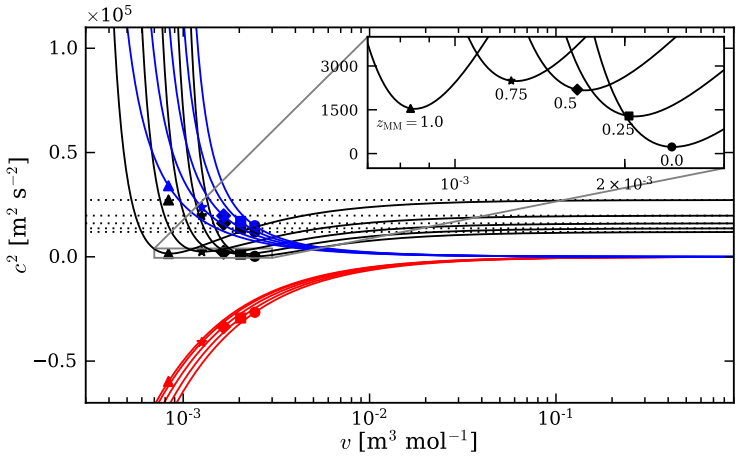

Figure 3.1: Speed of sound along the critical isotherm as a function of the specific volume for a MM–MD$_4$M binary mixture with composition of z_{MM} = 0 (●), 0.25 (■), 0.5 (⧫), 0.75 (★), 1 (▲). Calculated with the polytropic van der Waals equation of state for mixtures with $k_{ij} = 0$ and $l_{ij} = 0$. The repulsive contribution is the blue line (–), the attractive contribution is the red line (–), the black dotted line (···) is the ideal gas contribution and the black line (–) is the speed of sound. The insert is a detailed view of the critical region and critical points.

the pure fluids relations, due to the van der Waals mixing rules, Eqs. (2.27) and (2.28) and mixture critical point criteria explained in Section 2.2.

The speed of sound for mixtures is made non-dimensional using the critical temperature and the mixture specific gas constant

$$c^2_{\mathrm{r,m}} = \frac{c^2_{\mathrm{m}}(T,v,z)}{R_{\mathrm{m}} T_{\mathrm{c,m}}}. \tag{3.10}$$

The reduced form therefore reads

$$c^2_{\mathrm{r,m}} = \left[1 + \frac{2}{N_{\mathrm{m}}}\right] T_{\mathrm{r,m}} \left[\frac{v_{\mathrm{r,m}}}{v_{\mathrm{r,m}} - b_{\mathrm{r,m}}}\right]^2 - \frac{2a_{\mathrm{r,m}}}{v_{\mathrm{r,m}}} Z_{\mathrm{c,m}}. \tag{3.11}$$

Therefore the ideal gas, repulsive and attractive contributions are given by

$$c^2_{\mathrm{r,m,id}}(T_{\mathrm{r,m}}, \bar{z}) = \left[1 + \frac{2}{N_{\mathrm{m}}}\right] T_{\mathrm{r,m}} > 0, \tag{3.12}$$

$$\delta c^2_{\mathrm{r,m,rep}}(T_{\mathrm{r,m}}, v_{\mathrm{r,m}}, \bar{z}) = c^2_{\mathrm{r,m,id}}(T_{\mathrm{r,m}}, z) b_{\mathrm{r,m}} \frac{2v_{\mathrm{r,m}} - b_{\mathrm{r,m}}}{(v_{\mathrm{r,m}} - b_{\mathrm{r,m}})^2} > 0, \tag{3.13}$$

$$\delta c^2_{\mathrm{r,m,att}}(v_{\mathrm{r,m}}, \bar{z}) = -\frac{2a_{\mathrm{r,m}}}{v_{\mathrm{r,m}}} Z_{\mathrm{c,m}} < 0. \tag{3.14}$$

These relations allow the comparison of the properties of different substances and compositions at the same reduced conditions. The contributions of the dimensional speed of sound are illustrated in Fig. 3.2 along the critical isotherm. A detailed view of the critical region and critical point behavior with changing composition of the various contributions is shown in Fig. 3.3.

As seen in Section 3.2.1 the reduced speed of sound also has a maximum at combination of the pure components, which indicates the non-monotonic behavior of the speed of sound of mixtures.

From Eq. (3.12) it is seen that the ideal contribution depends on the reduced temperature. The reduced temperature, $T_{\mathrm{r,m}}$, depends on the composition through the mixtures critical temperature, $T_{\mathrm{c,m}}$, which varies with composition. The ideal gas and repulsive force contribution scale with the factor $[1+2/N_{\mathrm{m}}]$, which decreases if the molecular complexity increases, shown in Section 3.2.1. This is because the ideal gas contribution is connected with the internal energy of the translation, rotational, and vibrational modes, which are related to the molecular complexity. The more complex the molecule is, the greater the capacity to absorb energy and less energy is transfered to the translation, rotational, and vibrational modes which are responsible for sound propagation [4].

The second component of the repulsive force introduces a non-monotonic behavior with changing composition dependent on $b_{\mathrm{r,m}}$, as seen in Section 3.2.1.

From Eq. (3.14) it is seen that the attractive force contribution depends on the critical compressibility factor, $Z_{\mathrm{c,m}}$, and attractive parameter $a_{\mathrm{r,m}}$.

A detailed examination of the non-monotonic speed of sound behavior with changing composition is elaborated in the next section.

3.3 Binary mixture properties of linear siloxanes using polytropic van der Waals model

The mixture speed of sound depends on the critical properties, active degrees of freedom as well as attractive and repulsive parameters. The attractive and repulsive mixture parameters can be directly related to the pure component properties, through the mixing rules. For the critical properties it is more complicated because it also depend on the mixture stability conditions described in Section 2.3. Based on the research of Guardone et al. [2] on non-classical gas dynamics of vapor mixtures, binary mixtures of linear siloxanes are investigated to describe the non-monotonic behavior of the mixtures speed of sound.

3.3.1 Relation to pure component properties

In case of the VdW-OF EOS the mixture parameters a_{m} and b_{m} depend only on the pure component critical point properties and the composition. The van der Waals one fluid mixing rules are calculated from constants of an equation of state (critical

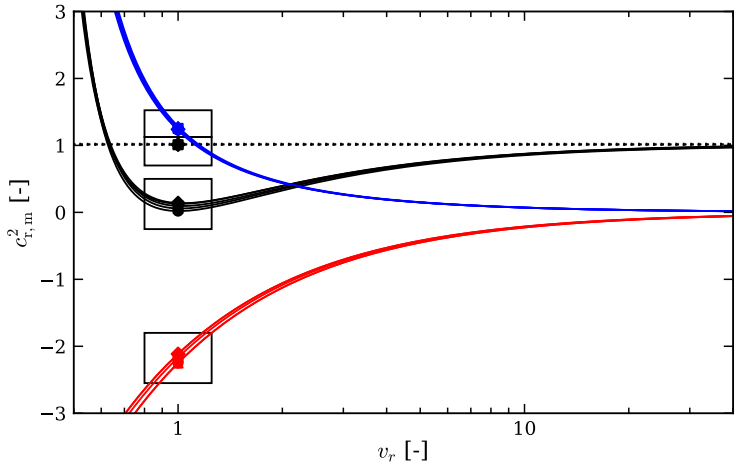

Figure 3.2: Dimensionless speed of sound along the critical isotherm as a function of the reduced specific volume for a MM–MD$_4$M binary mixture with composition z_{MM} = 0 (●), 0.25 (■), 0.5 (♦), 0.75 (★), 1 (▲). Calculated with the van der Waals equation of state for mixtures with $k_{ij} = 0$ and $l_{ij} = 0$. The repulsive contribution is blue (–), the attractive contribution is red (–), the black dotted line is the ideal gas contribution (···) and the black line is the speed of sound (–). The inserts are shown in Fig. 3.3.

properties and composition) and not from any thermodynamic state function which may appear in an equation of state [10]. This means that mixture parameters can all be related to the constant pure component properties, $T_{\mathrm{c},i}$, $P_{\mathrm{c},i}$, M_i and N_i using the variable composition z_i. For the analyses of the different contributions of the pure component properties in binary mixtures several parameters are introduced. The first parameters are related to the critical temperature and pressure as

$$\delta = \frac{T_{\mathrm{c},2}}{T_{\mathrm{c},1}}, \qquad \pi = \frac{P_{\mathrm{c},2}}{P_{\mathrm{c},1}}. \tag{3.15}$$

The parameters δ and π are defined as the ratio of the critical temperature and pressure respectively, from the second component over the first component. The first component with index 1 is chosen as the fluid with the lower molecular complexity in comparison with the second component. The following parameters are related to the fluid parameters a and b as

$$\alpha(\delta,\pi) = \frac{a_2}{a_1} = \frac{T^2_{\mathrm{c},2}}{T^2_{\mathrm{c},1}}\frac{P_{\mathrm{c},1}}{P_{\mathrm{c},2}} = \frac{\delta^2}{\pi}, \tag{3.16}$$

$$\beta(\delta,\pi) = \frac{b_2}{b_1} = \frac{T_{\mathrm{c},2}}{T_{\mathrm{c},1}}\frac{P_{\mathrm{c},1}}{P_{\mathrm{c},2}} = \frac{\delta}{\pi}. \tag{3.17}$$

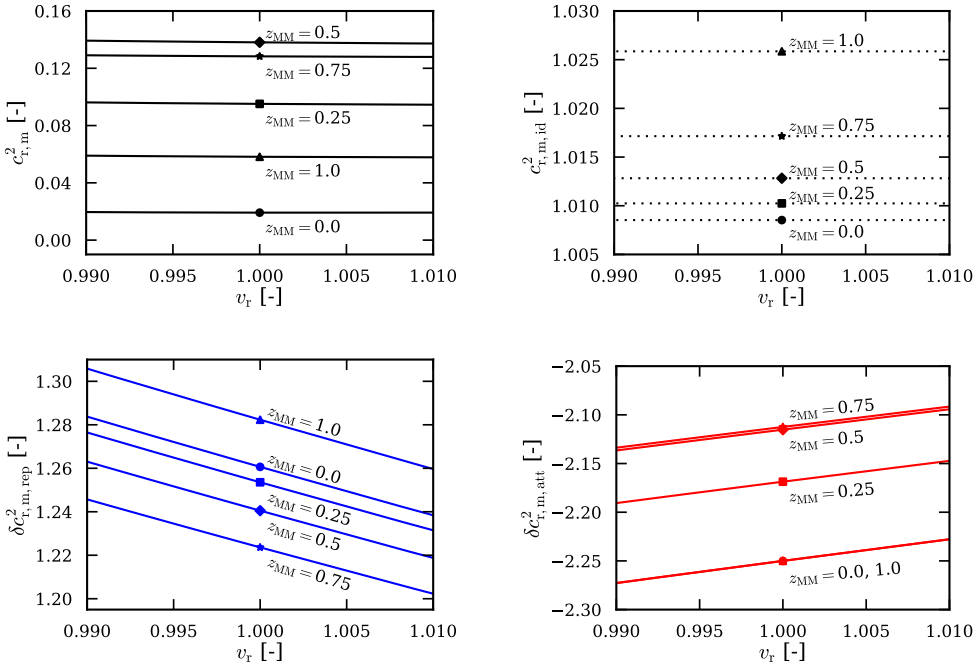

Figure 3.3: Detailed view of the reduced speed of sound, ideal gas, repulsive and attractive contributions around the critical point shown in Fig. 3.2. For a MM–MD_4M binary mixture with composition z_{MM} = 0 (•), 0.25 (■), 0.5 (⧫), 0.75 (★), 1 (▲).

The parameters α and β are defined as the ratio of the second component over the first component from a_i and b_i respectively. α and β can be reduced to the parameters δ and π.

The last parameters are defined from the molecular weight and the number of active degrees of freedom as

$$\eta = \frac{M_2}{M_1}, \qquad \mu = \frac{N_2}{N_1}, \tag{3.18}$$

Table 3.1 shows the pure component properties of the linear siloxanes evaluated in this research. With increasing complexity of the linear siloxane molecule the critical temperature increases and the critical pressure decreases. Table 3.1 shows that the molar attractive and repulsive forces increase with heavier molecules. This holds only within a family of fluids with similar molecular arrangement.

The binary mixture parameters defined in Eqs. (3.15) to (3.18) are listed in Table 3.2 for linear siloxanes. It is clear that with a larger molecular complexity difference between the pure components, the more the parameters differ from unity. In the

Table 3.1: Linear siloxane properties from REFPROP [11] and FluidProp [5]. Critical temperature T_c and pressure P_c, molecular weight M, active degrees of freedom N determined by evaluating the ideal gas isochoric specific heat at the critical temperature $N = 2c_v^o(T_c)/R$, and van der Waals coefficients, attractive a_{mol} and repulsive b_{mol}.

Fluid	Chemical formula	T_c °C	P_c MPa	M g mol^{-1}	N -	a_{mol} Pa m^6 mol^{-2}	b_{mol} m^3 mol^{-1}	Ref.
MM	$C_6H_{18}OSi_2$	245.55	1.93	162.38	78.35	4.06	$2.79 \cdot 10^{-4}$	[12]
MDM	$C_8H_{24}O_2Si_3$	292.21	1.44	236.53	115.92	6.48	$4.09 \cdot 10^{-4}$	[13]
MD_2M	$C_{10}H_{30}O_3Si_4$	326.25	1.14	310.69	149.93	9.16	$5.45 \cdot 10^{-4}$	[13]
MD_3M	$C_{12}H_{36}O_4Si_5$	355.81	0.96	384.84	194.14	12.00	$6.80 \cdot 10^{-4}$	[14]
MD_4M	$C_{14}H_{42}O_5Si_6$	380.05	0.84	458.99	234.42	14.81	$8.08 \cdot 10^{-4}$	[14]
MD_5M	$C_{16}H_{48}O_6Si_7$	398.65	0.70	533.15	274.88	18.78	$9.97 \cdot 10^{-4}$	[15]
MD_6M	$C_{18}H_{54}O_7Si_8$	415.75	0.68	607.30	306.93	20.36	$1.05 \cdot 10^{-3}$	[15]

Table 3.2: Binary mixture parameters of linear siloxane mixtures.

1\2	MM	MDM	MD_2M	MD_3M	MD_4M	MD_5M	MD_6M
MM	$\delta = 1.00$ $\mu = 1.00$ $\pi = 1.00$ $\eta = 1.00$ $\alpha = 1.00$ $\beta = 1.00$	$\delta = 1.09$ $\mu = 1.47$ $\pi = 0.73$ $\eta = 1.46$ $\alpha = 1.62$ $\beta = 1.49$	$\delta = 1.16$ $\mu = 1.91$ $\pi = 0.61$ $\eta = 1.91$ $\alpha = 2.20$ $\beta = 1.90$	$\delta = 1.21$ $\mu = 2.39$ $\pi = 0.51$ $\eta = 2.37$ $\alpha = 2.86$ $\beta = 2.36$	$\delta = 1.26$ $\mu = 2.99$ $\pi = 0.45$ $\eta = 2.83$ $\alpha = 3.50$ $\beta = 2.78$	$\delta = 1.30$ $\mu = 3.41$ $\pi = 0.39$ $\eta = 3.28$ $\alpha = 4.26$ $\beta = 3.29$	$\delta = 1.33$ $\mu = 3.92$ $\pi = 0.35$ $\eta = 3.74$ $\alpha = 5.05$ $\beta = 3.81$
MDM		$\delta = 1.00$ $\mu = 1.00$ $\pi = 1.00$ $\eta = 1.00$ $\alpha = 1.00$ $\beta = 1.00$	$\delta = 1.06$ $\mu = 1.29$ $\pi = 0.83$ $\eta = 1.31$ $\alpha = 1.35$ $\beta = 1.28$	$\delta = 1.11$ $\mu = 1.62$ $\pi = 0.70$ $\eta = 1.63$ $\alpha = 1.76$ $\beta = 1.58$	$\delta = 1.16$ $\mu = 2.03$ $\pi = 0.62$ $\eta = 1.94$ $\alpha = 2.16$ $\beta = 1.87$	$\delta = 1.19$ $\mu = 2.32$ $\pi = 0.54$ $\eta = 2.25$ $\alpha = 2.63$ $\beta = 2.21$	$\delta = 1.22$ $\mu = 2.67$ $\pi = 0.48$ $\eta = 2.57$ $\alpha = 3.12$ $\beta = 2.55$
MD_2M			$\delta = 1.00$ $\mu = 1.00$ $\pi = 1.00$ $\eta = 1.00$ $\alpha = 1.00$ $\beta = 1.00$	$\delta = 1.05$ $\mu = 1.25$ $\pi = 0.84$ $\eta = 1.24$ $\alpha = 1.30$ $\beta = 1.24$	$\delta = 1.09$ $\mu = 1.57$ $\pi = 0.74$ $\eta = 1.48$ $\alpha = 1.60$ $\beta = 1.46$	$\delta = 1.12$ $\mu = 1.79$ $\pi = 0.65$ $\eta = 1.72$ $\alpha = 1.94$ $\beta = 1.73$	$\delta = 1.15$ $\mu = 2.06$ $\pi = 0.57$ $\eta = 1.95$ $\alpha = 2.30$ $\beta = 2.00$
MD_3M				$\delta = 1.00$ $\mu = 1.00$ $\pi = 1.00$ $\eta = 1.00$ $\alpha = 1.00$ $\beta = 1.00$	$\delta = 1.04$ $\mu = 1.25$ $\pi = 0.88$ $\eta = 1.19$ $\alpha = 1.23$ $\beta = 1.18$	$\delta = 1.07$ $\mu = 1.43$ $\pi = 0.77$ $\eta = 1.39$ $\alpha = 1.49$ $\beta = 1.40$	$\delta = 1.10$ $\mu = 1.64$ $\pi = 0.68$ $\eta = 1.58$ $\alpha = 1.77$ $\beta = 1.61$
MD_4M					$\delta = 1.00$ $\mu = 1.00$ $\pi = 1.00$ $\eta = 1.00$ $\alpha = 1.00$ $\beta = 1.00$	$\delta = 1.03$ $\mu = 1.14$ $\pi = 0.87$ $\eta = 1.16$ $\alpha = 1.22$ $\beta = 1.18$	$\delta = 1.05$ $\mu = 1.31$ $\pi = 0.77$ $\eta = 1.32$ $\alpha = 1.44$ $\beta = 1.37$
MD_5M						$\delta = 1.00$ $\mu = 1.00$ $\pi = 1.00$ $\eta = 1.00$ $\alpha = 1.00$ $\beta = 1.00$	$\delta = 1.03$ $\mu = 1.15$ $\pi = 0.89$ $\eta = 1.14$ $\alpha = 1.19$ $\beta = 1.00$
MD_6M							$\delta = 1.00$ $\mu = 1.00$ $\pi = 1.00$ $\eta = 1.00$ $\alpha = 1.00$ $\beta = 1.00$

next sections it will be shown that this has a direct influence on the mixture properties with various compositions.

3.3.2 Van der Waals mixture parameters

The reduced mixture parameters, $a_{r,m}$ and $b_{r,m}$, from Eq. (3.9) are plotted in Fig. 3.4 as a function of the composition z_i for different binary mixtures combinations of MM–MD_jM where $i, j = 1..6$ with varying compositions. With changing composition the attractive and repulsive force parameters are non-monotonic and decreasing. The reduced attractive parameter has a larger variation with composition from the pure component than the repulsive parameter. Also both parameters are shifting to the less complex component with increasing molecular complexity between the components.

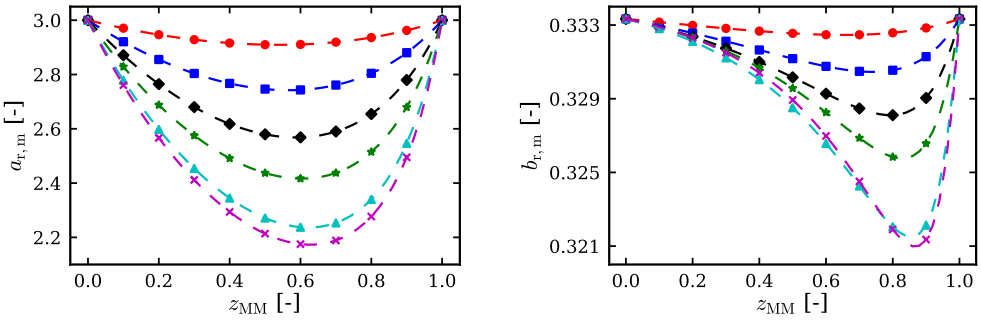

Figure 3.4: Reduced form of attractive ($a_{r,m}$) and repulsive ($b_{r,m}$) mixture parameters from the van der Waals equation of state for mixtures with $k_{ij} = 0$ and $l_{ij} = 0$. Evaluated for binary mixture combinations of MM with MDM (●), MD_2M (■), MD_3M (♦), MD_4M (★), MD_5M (▲), and MD_6M (×) and compositions varying from $z_{\mathbf{MM}} = 0...1$.

These figures already imply the non-monotonic behavior of the mixtures speed of sound observed in Section 3.2.

3.3.3 Mixture critical point properties

The mixtures critical properties are shown in Fig. 3.5. These properties are calculated using the stability criteria for mixtures given in Section 2.3 and implementation of the method developed by Heidemann et al. [9]. A non-linear behavior with changing composition is observed for the critical temperature, pressure and specific volume. The non-linearity for temperature and pressure is increasing with a larger molecular complexity difference between the components. The largest effect is observed for the mixture critical compressibility factor. The curve of the critical compressibility factor also shows great significance with the reduced attractive parameter curve from Fig. 3.4. Because the critical point of a mixture does not obey the mechanical stability criteria as for pure components, the critical compressibility factor is not constant with changing composition.

For a mixture of linear siloxanes, the critical compressibility factor increases non-monotonically. Also with increasing difference between the molecular complexity of the pure components the critical compressibility factor exhibits an increase in non-monotonic behavior. This increase shows that the critical compressibility factor is closer to unity and ideal gas behavior, which indicates that the attractive forces are less dominant. This is seen by the decrease of $a_{r,m}$ in Fig. 3.4. This also implicates that the decrease of the attractive force is dominant over the decrease of the repulsive force for linear siloxanes. Due to the high non-monotonic behavior of the critical compressibility factor will have a significant effect on the mixture speed of sound.

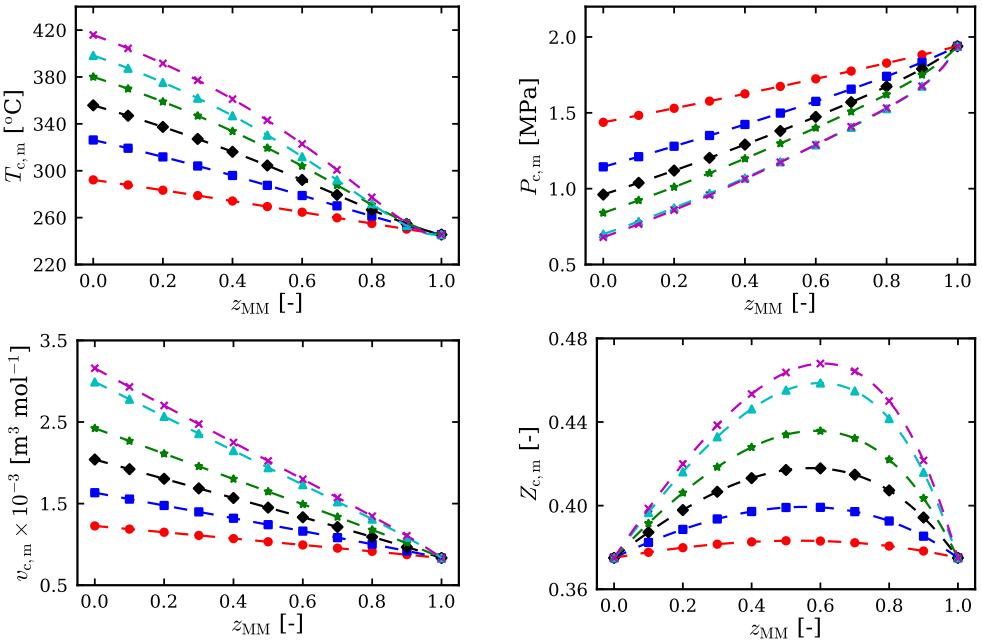

Figure 3.5: Critical properties, temperature T_c, pressure P_c, specific volume v_c and compressibility factor Z_c. Evaluated for binary mixture combinations of MM with MDM (●), MD_2M (■), MD_3M (⧫), MD_4M (★), MD_5M (▲), and MD_6M (×) and compositions varying from $z_{\mathbf{MM}} = 0...1$. Calculated with the van der Waals equation of state for mixtures with $k_{ij} = 0$ and $l_{ij} = 0$.

3.3.4 Speed of sound properties

The reduced speed of sound and contributions are calculated at the mixture critical point and shown in Fig. 3.6. The reduced speed of sound is calculated on the critical point because the reduced properties, $T_{r,m}$ and $v_{r,m}$ will be unity. So the reduced speed of sound is related to the critical compressibility factor, attractive parameter, repulsive parameter and active degrees of freedom. The reduced speed of sound has a high non-monotonic behavior with changing composition. The ideal gas contribution scales with $[1+2/N_m]$ which decreases with increasing molecular complexity and only depends on the linear relation of the active degrees of freedom in Eq. (2.33).

The repulsive contribution depends on the ideal gas contribution and the non-monotonic part depending on $b_{r,m}$. Seen in Fig. 3.6 for the repulsive contribution to the speed of sound the graph is shifted by the ideal gas contribution. The second part of the repulsive contribution follows the non-monotonicity of the reduced repulsive parameter, $b_{r,m}$ from Fig. 3.4. The attractive contribution is a combination of the reduced attractive parameter and the compressibility factor. This combination causes

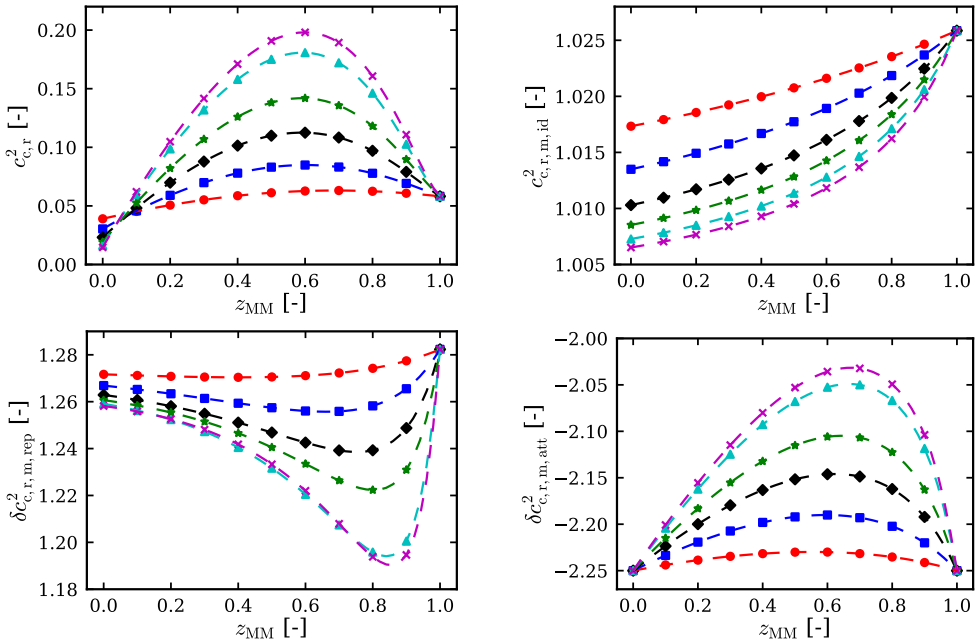

Figure 3.6: Reduced speed of sound with ideal gas, repulsive and attractive contribution evaluated at the critical point. Evaluated for binary mixture combinations of MM with MDM (●), MD_2M (■), MD_3M (♦), MD_4M (★), MD_5M (▲), and MD_6M (×) and compositions varying from $z_{\mathbf{MM}} = 0...1$. Calculated with the van der Waals equation of state for mixtures with $k_{ij} = 0$ and $l_{ij} = 0$.

an increase of the attractive speed of sound contribution.

Fig. 3.7 presents the percentage contribution of the ideal gas, repulsive, and attractive force contribution to the overall speed of sound of linear siloxane mixtures. The percentage contribution clearly shows the large influence of the attractive contribution on the speed of sound, around 49%. The ideal gas and repulsive force contribution, contribute around 23% and 28% to the overall speed of sound respectively. This shows that the large non-monotonicity is mostly due to the attractive force contribution which is directly related to the critical compressibility factor, $Z_{c,m}$, and attractive contribution, $a_{r,m}$.

3.4 Binary mixture properties of perfluorocarbons using polytropic van der Waals model

The binary mixture properties of perfluorocarbons are investigated using the polytropic van der Waals model to verify the non-monotonic behavior of the speed of

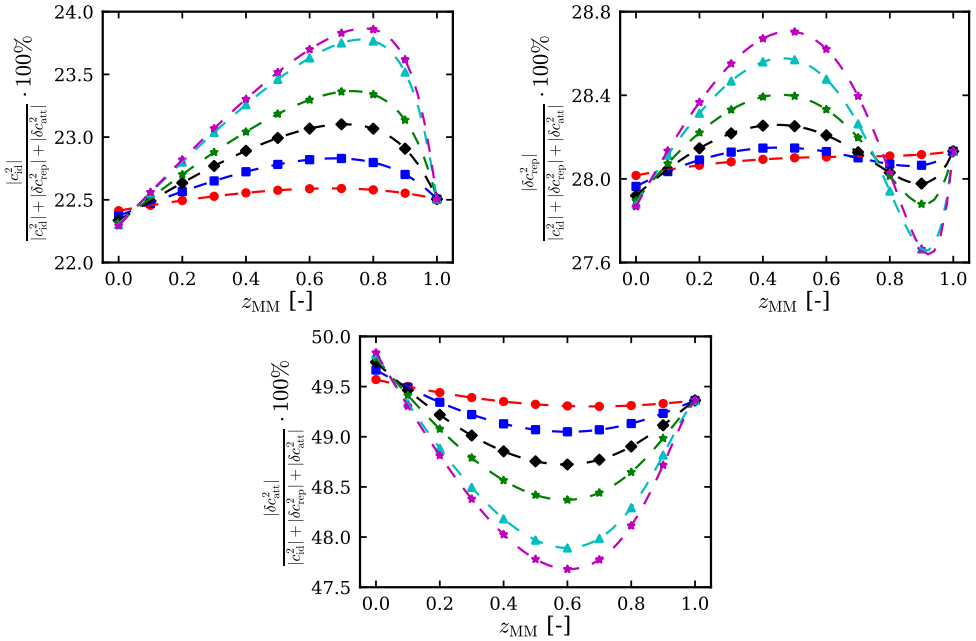

Figure 3.7: Percentage contribution of the ideal gas, repulsive, and attractive contributions on the speed of sound at the critical point. Evaluated for binary mixture combinations of MM with MDM (●), MD_2M (■), MD_3M (♦), MD_4M (★), MD_5M (▲), and MD_6M (×) and compositions varying from $z_{\mathbf{MM}} = 0...1$. Calculated with the van der Waals equation of state for mixtures with $k_{ij} = 0$ and $l_{ij} = 0$.

sound and the relation to the critical properties. Table 3.3 shows the pure components properties of the perfluorocarbons investigated The perfluorocarbons are selected based on the property that they can exhibit non-ideal compressible fluid effects in the gas phase. The pure fluid properties show similar behavior as the linear siloxanes; with increasing complexity, the critical temperature increases and the critical pressure decreases. The molar attractive and repulsive forces increase as the molecular mass increases, as is the case for fluids of the same family.

3.4.1 Critical point properties perfluorocarbon mixtures

The reduced mixture parameters, $a_{\mathrm{r,m}}$ and $b_{\mathrm{r,m}}$ are plotted in Fig. 3.8 for different binary mixtures of perfluorocarbons. With changing composition the attractive and repulsive force parameters are non-monotonic. The attractive force, $a_{\mathrm{r,m}}$, shows the same decreasing non-monotonic behavior as for the linear siloxane mixtures. The repulsive forces, $b_{\mathrm{r,m}}$, on the other hand shows a non-monotonic increase for mixtures, this is opposite from what is observed for linear siloxanes in Fig. 3.4 where the repulsive force non-monotonically decreases for a mixture.

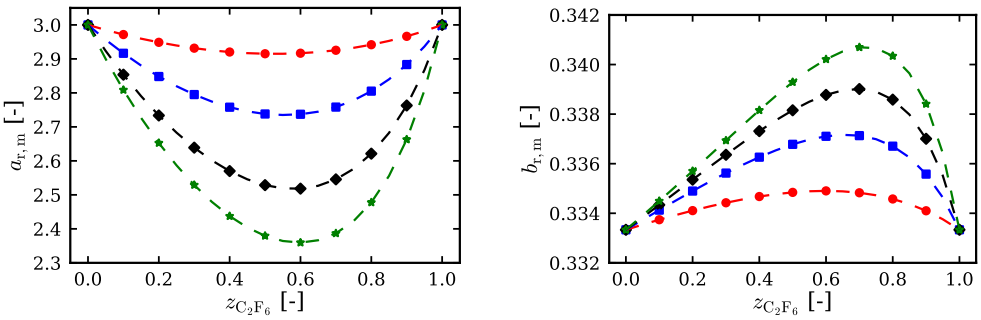

Figure 3.8: Reduced form of attractive ($a_{r,m}$) and repulsive ($b_{r,m}$) mixture parameters from the van der Waals equation of state for mixtures with $k_{ij} = 0$ and $l_{ij} = 0$. Evaluated for binary mixture combinations of C_2F_6 with C_3F_8 (●), C_4F_{10} (■), C_5F_{12} (♦), and C_6F_{14} (★) and compositions varying from $z_{C_2F_6} = 0...1$.

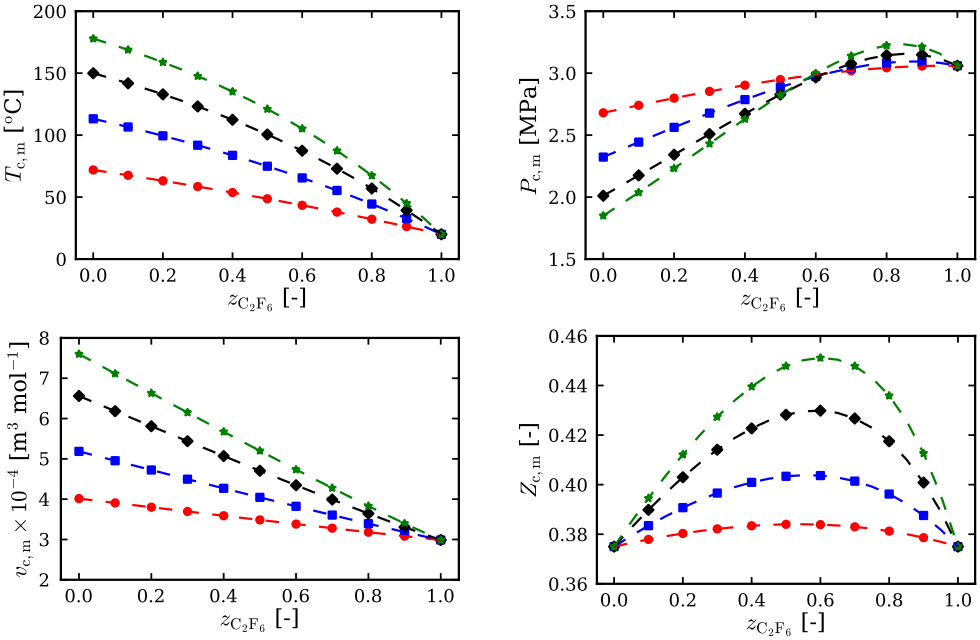

Figure 3.9: Critical properties, temperature T_c, pressure P_c, specific volume v_c and compressibility factor Z_c. Evaluated for binary mixture combinations of C_2F_6 with C_3F_8 (●), C_4F_{10} (■), C_5F_{12} (♦), and C_6F_{14} (★) and compositions varying from $z_{C_2F_6} = 0...1$. Calculated with the van der Waals equation of state for mixtures with $k_{ij} = 0$ and $l_{ij} = 0$.

Table 3.3: Perfluorocarbons properties from REFPROP [11]. Critical temperature T_c and pressure P_c, molecular weight M, active degrees of freedom N determined by evaluating the ideal gas isochoric specific heat at the critical temperature $N = 2c_v^o(T_c)/R$, and van der Waals coefficients, attractive a_{mol} and repulsive b_{mol}.

Fluid	Chemical Formula	T_c °C	P_c MPa	M g mol^{-1}	N -	a_{mol} Pa m^6 mol^{-2}	b_{mol} m^3 mol^{-1}	Ref.
Perfluoroethane	C_2F_6	19.88	3.05	138.01	23.33	0.82	$1.00 \cdot 10^{-4}$	[16]
Perfluoropropane	C_3F_8	71.87	2.64	188.02	36.75	1.30	$1.34 \cdot 10^{-4}$	[16]
Perfluorobutane	C_4F_{10}	113.18	2.32	238.03	51.97	1.87	$1.73 \cdot 10^{-4}$	[17]
Perfluoropentane	C_5F_{12}	147.85	2.06	288.03	65.26	2.60	$2.19 \cdot 10^{-4}$	[17]
Perfluorohexane	C_6F_{14}	174.85	1.74	338.04	79.73	3.21	$2.53 \cdot 10^{-4}$	[17]

The critical properties for the binary mixtures of perfluorocarbons are shown in Fig. 3.9. Non-linear behavior is observed for the critical temperature with increasing non-linearity for increasing molecular complexity difference between the pure components. For the case of perfluorocarbons binary mixtures non-monotonic behavior is also observed for the critical pressure, which differs from the critical pressure of linear siloxanes where non-linear behavior is observed. The critical compressibility factor exhibits again an increasing non-monotonic behavior upon mixing as is also observed for the linear siloxanes.

3.4.2 Speed of sound properties perfluorocarbon mixtures

The reduced speed of sound and contributions calculated at the mixture critical point are shown in Fig. 3.10. The reduced speed of sound has a non-monotonic behavior with changing composition. The ideal gas contribution scales with $[1+2/N_m]$ which decreases with increasing molecular complexity and only depends on the linear relation of the active degrees of freedom in Eq. (2.33). Due to the smaller difference in active degrees of freedom, the ideal gas contribution is larger for the perfluorocarbons due to the scaling $[1+2/N_m]$.

The repulsive contribution depends on the ideal gas contribution and the repulsive force $b_{r,m}$. The repulsive contribution is shifted, showing a non-monotonic increase close to the lower complex fluid in the mixture. This shift is comparable to the shift of the critical pressures non-monotonic behavior.

The attractive contribution is a combination of the reduced attractive parameter and the compressibility factor. This combination causes a non-monotonic increase of the attractive speed of sound contribution.

Adding the contributions show that the attractive contribution has the largest effect on the increasing non-monotonic behavior of the mixture. The repulsive contribution causes an increase in speed of sound closer to the less molecular complex component. The larger effect of the ideal gas contribution causes a decrease of the non-monotonic behavior of the mixture, causing a larger difference between the pure

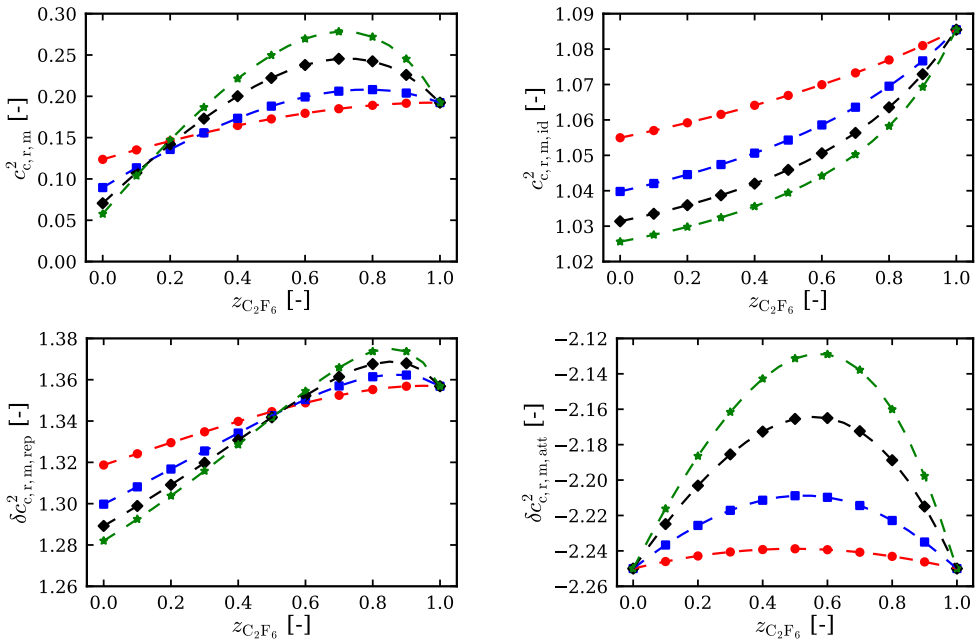

Figure 3.10: Reduced speed of sound with ideal gas, repulsive and attractive contribution evaluated at the critical point. Evaluated for binary mixture combinations of C_2F_6 with C_3F_8 (●), C_4F_{10} (■), C_5F_{12} (◆), and C_6F_{14} (★) and compositions varying from $z_{C_2F_6} = 0...1$. Calculated with the van der Waals equation of state for mixtures with $k_{ij} = 0$ and $l_{ij} = 0$.

components reduced speed of sound. This shows that the non-monotonicity is mostly due to the attractive contribution which is directly related to the critical compressibility factor, $Z_{c,m}$, and attractive contribution, $a_{r,m}$.

Fig. 3.11 presents the percentage contribution of the ideal gas, repulsive, and attractive force contribution to the overall speed of sound of perfluorocarbon mixtures. In the case of perfluorocarbon mixtures the large influence of the attractive contribution on the speed of sound is also clearly visible, around 48%. The ideal gas and repulsive force contribution are around 23% and 29% respectively. This shows again that the large non-monotonicity is mostly due to the attractive contribution also in the case of perfluorocarbon mixtures.

3.5 Speed of sound for binary mixtures using Helmholtz energy multiparameter model

The speed of sound is calculated with the Helmholtz energy multiparameter equation of state of REFPROP [11] for binary mixtures of linear siloxanes and perfluorocar-

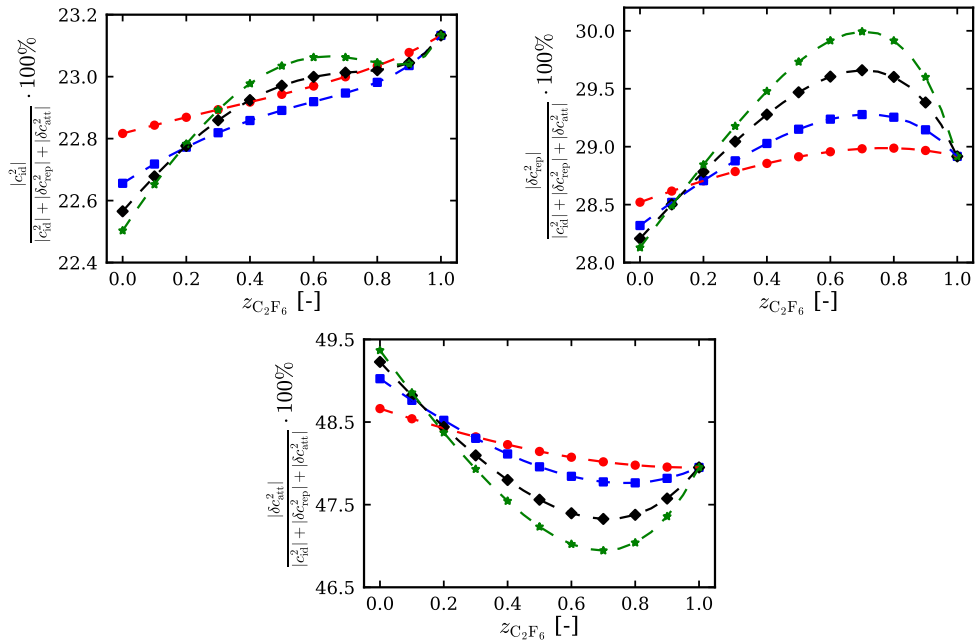

Figure 3.11: Percentage contribution of the ideal gas, repulsive, and attractive contributions on the speed of sound at the critical point. Evaluated for binary mixture combinations of C_2F_6 with C_3F_8 (●), C_4F_{10} (■), C_5F_{12} (◆), and C_6F_{14} (★) and compositions varying from $z_{C_2F_6} = 0...1$. Calculated with the van der Waals equation of state for mixtures with $k_{ij} = 0$ and $l_{ij} = 0$.

bons. The speed of sound is investigated at the critical point to compare and verify the results with the polytropic van der Waals model.

3.5.1 Linear Siloxanes

Binary mixtures of MM with MDM, MD_2M, MD_3M, and MD_4M are investigated (MD_5M and MD_6M are not present for the Helmholtz energy equation of state). The state-of-the-art coefficients for the Helmholtz energy equation of state for MM, MDM, and MD_2M are defined by Thol et al. [12] and Thol et al. [13], the state-of-the-art coefficients for MD_3M and MD_4M are derived by König et al. [14]. The applied mixture model is the GERG-2008 mixture formulation [18] with estimated mixing parameters.

The mixture critical properties of the Helmholtz energy multiparameter model are shown in Fig. 3.12. The critical properties show a similar behavior as the van der Waals model in Section 3.3.3, with larger non-linear behavior for the critical temperature. Except for the critical pressure which shows a non-monotonic behavior for mixtures with a high MM composition. The non-monotonic behavior of the

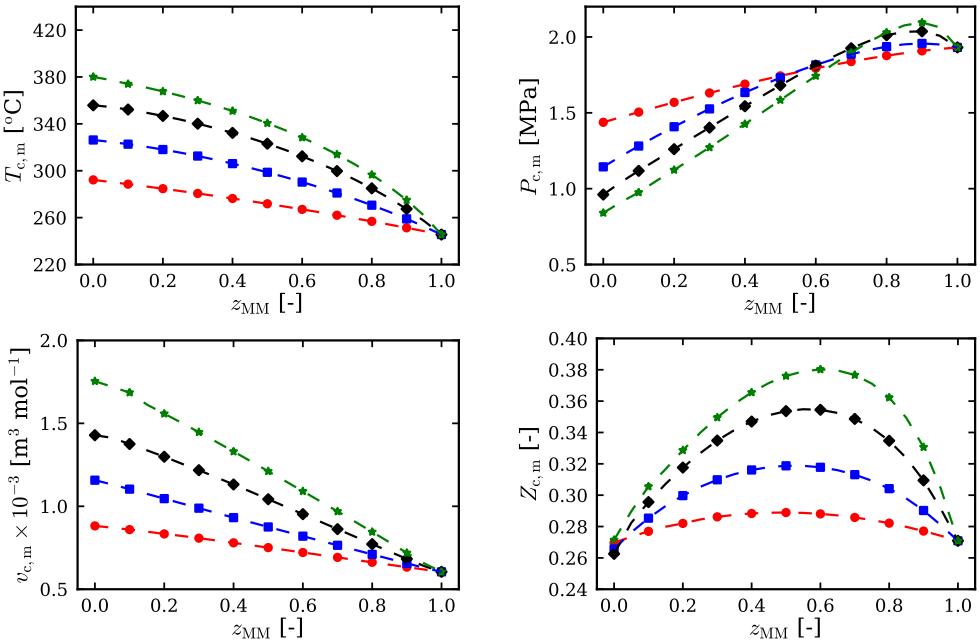

Figure 3.12: Critical properties, temperature T_c, pressure P_c, specific volume v_c and compressibility factor Z_c. Evaluated for binary mixture combinations of MM with MDM (●), MD_2M (■), MD_3M (◆), and MD_4M (★) and compositions varying from $z_{MM} = 0...1$. Calculated with the Helmholtz energy equation of state with estimated mixture parameters [11].

critical pressure is an interesting behavior, because the VdW-EOS does not show a non-monotonic behavior of the critical pressure. The difference in the critical pressure indicates a difference in the qualitative results of the thermodynamic models. This difference should be investigated in more detail in future research to exclude any errors in the equations of state and obtain a better understanding of the mixing rules. The critical compressibility factor shows again an increasing non-monotonic parabolic behavior. The maximum critical compressibility factor is again observed for a combination of the pure components with the largest critical compressibility factor obtained for the mixture with the largest difference between the pure components molecular complexity. This verifies the behavior of the critical compressibility factor from the van der Waals model.

The reduced speed of sound for linear siloxane mixtures is shown in Fig. 3.13. As seen in Section 3.3.4 for the van der Waals model, the speed of sound of the Helmholtz energy model shows a non-monotonic behavior between the pure components of the mixture. Verifying that the non-monotonic behavior of the mixture's critical speed of sound can be directly related to the non-monotonic behavior of the critical compressibility factor for linear siloxanes. The largest speed of sound is again obtained for the mixture with the largest difference between molecular complexity of

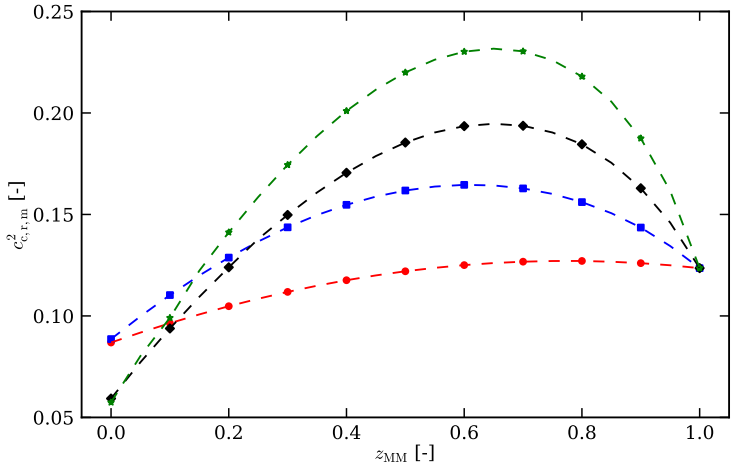

Figure 3.13: Reduced speed of sound calculated at the critical point. Evaluated for binary mixture combinations of MM with MDM (●), MD_2M (■), MD_3M (♦), and MD_4M (★) and compositions varying from $z_{MM} = 0...1$. Calculated with Helmholtz energy equation of state with estimated mixture parameters [11].

the pure components. The value of the critical speed of sound of the Helmholtz energy equation of state is larger then the van der Waals model, because the van der Waals model is not as accurate and underestimates the speed of sound.

3.5.2 Perfluorocarbons

The speed of sound and critical properties for binary mixtures of perfluorocarbons are investigated using the Helmholtz energy model. The state-of-the-art coefficients for the Helmholtz energy equation of state for C_2F_6 and C_3F_8 are defined by Lemmon et al. [16], the state-of-the-art coefficients for C_4F_{10}, C_5F_{12}, and C_6F_{14} are derived by Gao et al. but not yet published. The applied mixture model is the GERG-2008 mixture formulation [18] with estimated mixing parameters.

The mixture critical properties of the Helmholtz energy multiparameter model for binary mixtures of C_2F_6 with C_3F_8, C_4F_{10}, C_5F_{12}, and C_6F_{14} are shown in Fig. 3.14. The critical temperature and specific volume show an increase in non-ideal behavior in comparison with van der Waals model. A small non-monotonic behavior for the critical specific volume is observed for the mixture C_2F_6–C_6F_{14}. The critical pressure and compressibility factor show a larger non-monotonic behavior than the van der Waals model. The largest non-linear and non-monotonic behavior is again obtained for the mixture with the largest difference between molecular complexity of the pure components.

The reduced speed of sound of the Helmholtz energy model at the mixture's critical point is shown in Fig. 3.15. As seen in Section 3.3.4 for the van der Waals model,

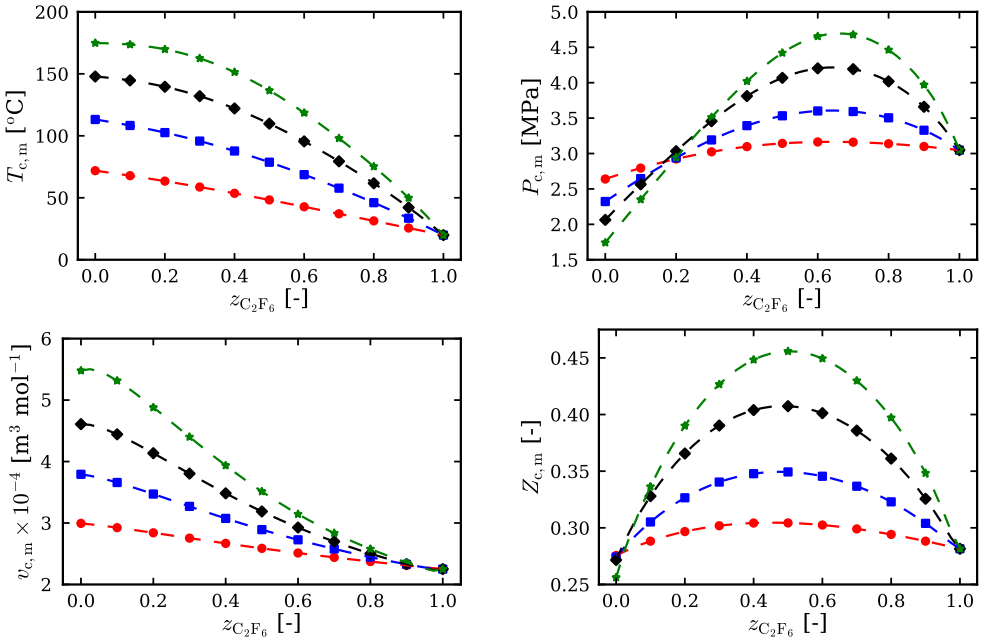

Figure 3.14: Critical properties, temperature T_c, pressure P_c, specific volume v_c and compressibility factor Z_c. Evaluated for binary mixture combinations of C_2F_6 with C_3F_8 (●), C_4F_{10} (■), C_5F_{12} (♦), and C_6F_{14} (★) and compositions varying from $z_{C_2F_6} = 0...1$. Calculated with the Helmholtz energy equation of state with estimated mixture parameters [11].

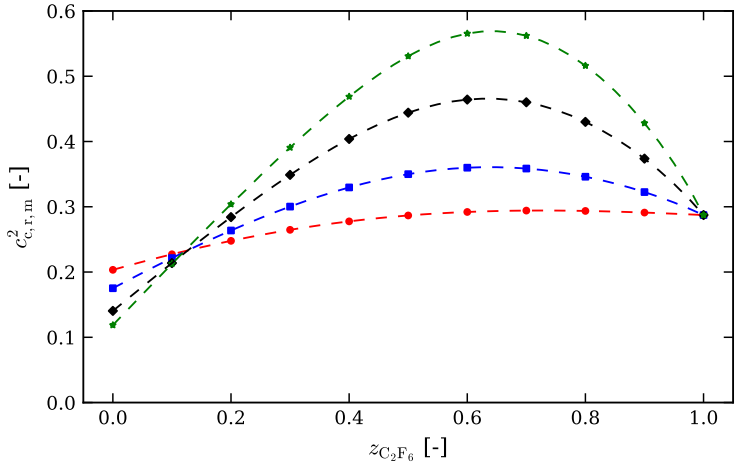

Figure 3.15: Reduced speed of sound calculated at the critical point. Evaluated for binary mixture combinations of C_2F_6 with C_3F_8 (●), C_4F_{10} (■), C_5F_{12} (♦), and C_6F_{14} (★) and compositions varying from $z_{C_2F_6} = 0...1$. Calculated with Helmholtz energy equation of state with estimated mixture parameters [11].

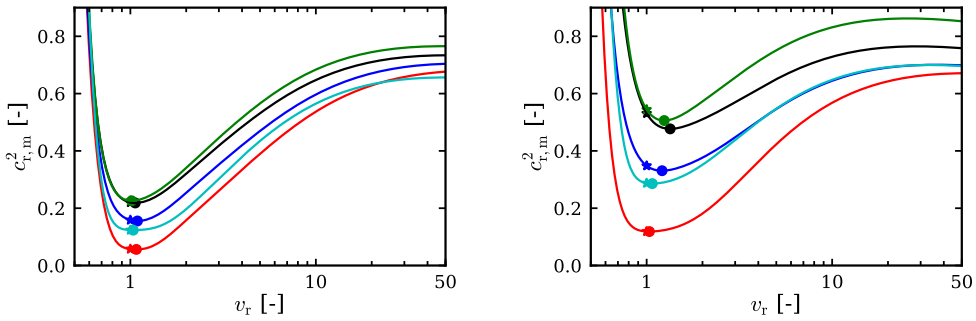

Figure 3.16: Speed of sound along saturation curve with solid lines indicating the composition z_1 = 0.0 (–), 0.25 (–), 0.50 (–), 0.75 (–), and 1.0 (–). With critical point (★) and minimum speed of sound (●). Calculated with Helmholtz energy equation of state with estimated mixture parameters [11]. Left) Binary mixture of MM–MD_4M. Right) Binary mixture of C_2F_6–C_6F_{14}.

the speed of sound of the Helmholtz energy model shows a non-monotonic behavior between the pure components of the mixture. The non-monotonic behavior of the Helmholtz model is increased in comparison with the van der Waals model. The largest speed of sound is again obtained for the mixture with the largest difference between molecular complexity of the pure components. Also for perfluorocarbons, the value of the critical speed of sound of the Helmholtz energy equation of state is larger then the van der Waals model, because the van der Waals model underestimates the speed of sound.

3.6 Speed of sound along dew curve and critical isotherm for binary mixtures

The speed of sound behavior along the saturation curve and critical isotherm is analyzed for binary mixtures of linear siloxanes and perfluorocarbons. The speed of sound along the saturation curve and critical isotherm is investigated to see the change in speed of sound behavior in other thermodynamic regions. The calculations are performed using the Helmholtz energy model implemented in REFPROP [11] with estimated mixture parameters.

3.6.1 Dew curve

The speed of sound along the saturation curve is shown in Fig. 3.16 for binary mixtures of linear siloxanes MM–MD_4M and perfluorocarbons C_2F_6–C_6F_{14} for varying composition of the first component z_1 = 0.0, 0.25, 0.50, 0.75, and 1.0. As is seen the speed of sound for the binary mixture of MM–MD_4M has a local minimum close to

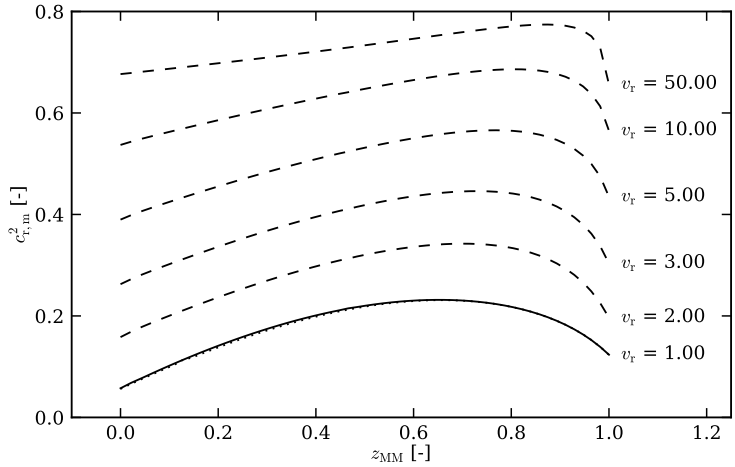

Figure 3.17: Speed of sound along dew line for MM–MD_4M with compositions varying from $z_{\mathrm{MM}} = 0...1$. The pressure is varied from $v_\mathrm{r} = 1$ to $v_\mathrm{r} = 50$ and indicated by the black dashed line (– –), minimum speed of sound along dew line ($\cdots$), and speed of sound at critical point (–). Calculated with Helmholtz energy equation of state with estimated mixture parameters [11].

the critical point and a non-monotonic behavior with changing composition as mentioned before. For the binary mixture of C_2F_6–C_6F_{14} the local minimum of the speed of sound along the saturation curve moves away from the critical point with changing composition.

Fig. 3.17 shows the speed of sound along the dew curve for binary mixture of MM–MD_4M with varying composition. The reduced specific volume is varied for each mixture with $v_\mathrm{r} = 1$ to $v_\mathrm{r} = 50$. The non-monotonic behavior of the speed of sound upon mixing is also observed along the dew curve and the maximum value for varying composition is shifted to the less molecular complex component in this case MM. This shows that the non-monotonic behavior of the speed of sound is not only occurring at the critical point but also in other thermodynamic regions.

The change of thermodynamic properties along the dew curve for the binary linear siloxane mixture MM–MD_4M with varying composition is shown in Fig. 3.18. The non-linear behavior of the temperature along the dew curve increases in comparison with the critical point temperature upon mixing. The non-monotonic behavior of the pressure decreases along the dew curve with increasing specific volume. The pressure moves to more ideal mixing for varying composition with decrease of pressure along the dew curve. The non-monotonic behavior of the compressibility factor decreases while moving along the dew curve. The compressibility factor is increasing along the dew curve, meaning the fluid is moving towards more ideal mixing, this explains the decrease of non-monotonic behavior of the compressibility factor. Though the non-monotonic behavior of the compressibility factor decreases, the speed of

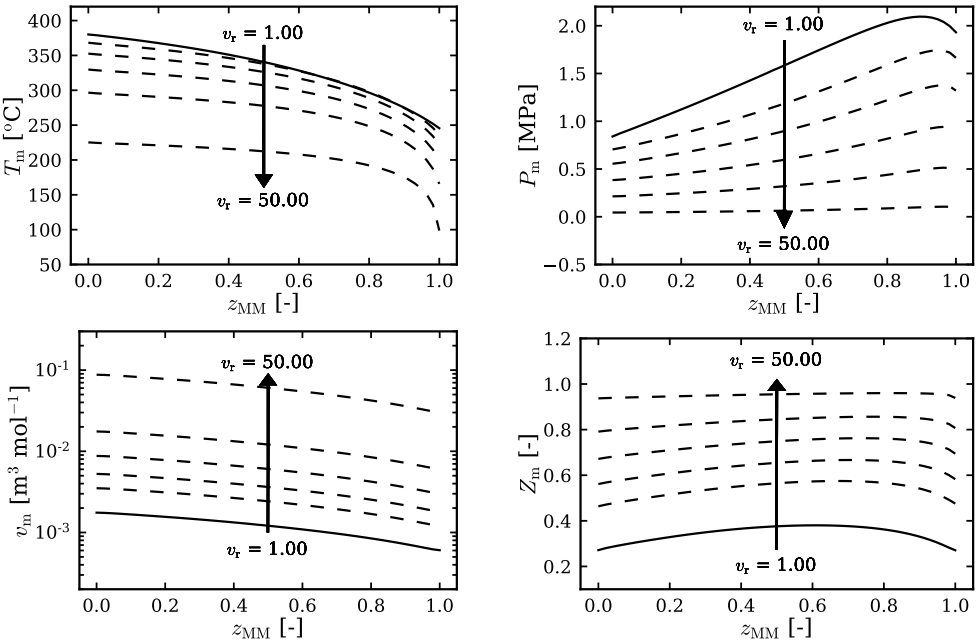

Figure 3.18: Thermodynamic properties temperature T, pressure P, specific volume v, and compressibility factor Z along dew line for MM–MD$_4$M with pressure varying from $v_r = 1$ to $v_r = 50$ (– –) and compositions varying from $z_{MM} = 0...1$. Critical point properties are shown by the solid black line (–). Calculated with Helmholtz energy equation of state with estimated mixture parameters [11].

sound still exhibits non-monotonic behavior along the dew curve.

The speed of sound along the dew curve for binary perfluorocarbon mixture C_2F_6–C_6F_{14} with varying composition is also analyzed and shown in Fig. 3.19 for varying reduced specific volume v_r = 1 to 50. As is observed in Fig. 3.16 the difference between the minimum speed of sound along the dew curve and the critical point speed of sound upon mixing increases, as is shown in Fig. 3.19 where the minimum speed of sound is the red line and the critical speed of sound the solid black line. The speed of sound non-monotonic behavior for varying composition increases and the maximum value for varying composition is shifted to the less molecular complex component in this case C_2F_6 for decreasing reduced specific volume. This verifies that the non-monotone behavior of the speed of sound can be observed in other thermodynamic regions and is not only observed at the critical point.

Fig. 3.20 shows the change of thermodynamic properties along the dew curve of C_2F_6–C_6F_{14} for varying composition. The non-linearity of the temperature increases when moving away from the critical point along the dew curve. On the other hand the non-monotonic behavior of the pressure decreases with varying composition and the same occurs for the critical compressibility factor. For the binary mixture of C_2F_6–

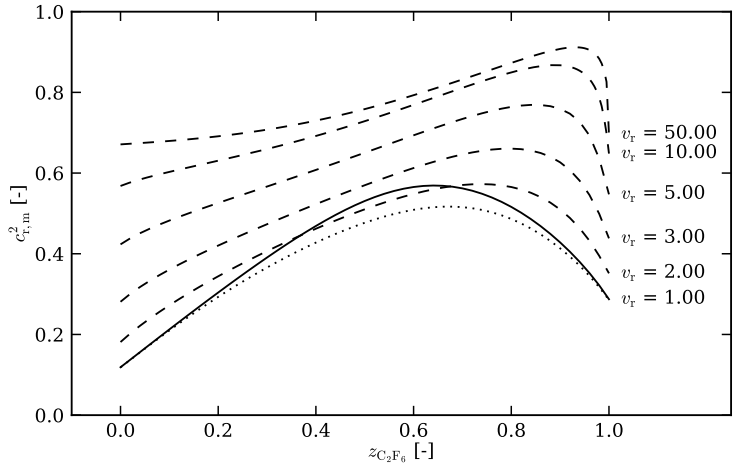

Figure 3.19: Speed of sound along dew line for C_2F_6–C_6F_{14} with pressure varying from $v_r = 1$ to $v_r = 50$ and compositions varying from $z_{C_2F_6} = 0...1$ (– –), minimum speed of sound along dew line (⋯) and speed of sound at critical point (–). Calculated with Helmholtz energy equation of state with estimated mixture parameters [11].

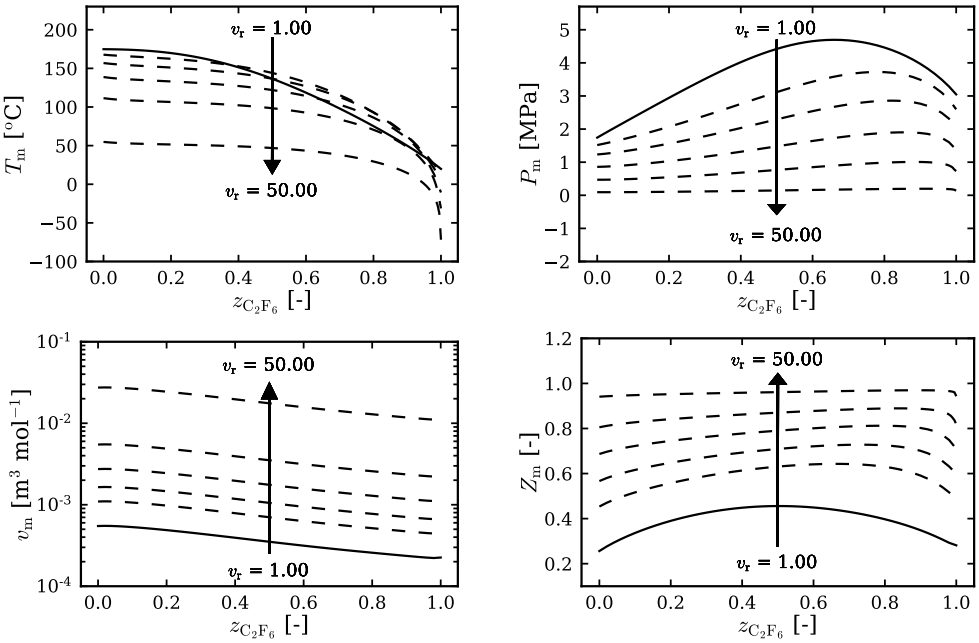

Figure 3.20: Thermodynamic properties temperature T, pressure P, specific volume v, and compressibility factor Z along dew line for C_2F_6–C_6F_{14} with pressure varying from $v_r = 1$ to $v_r = 50$ (– –) and compositions varying from $z_{C_2F_6} = 0...1$. Critical point value (–). Calculated with Helmholtz energy equation of state with estimated mixture parameters [11].

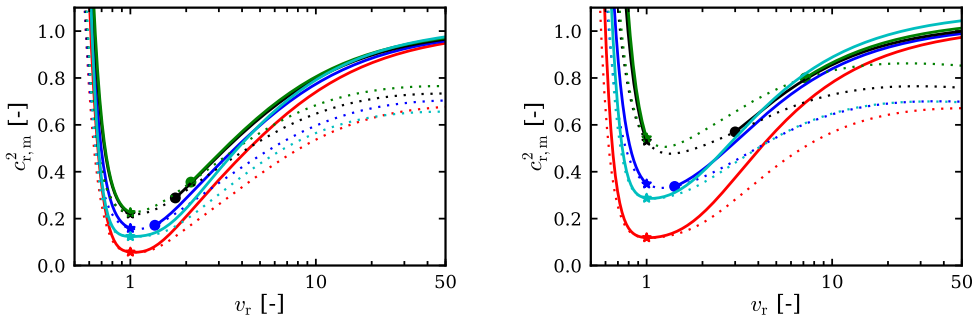

Figure 3.21: Speed of sound along critical isotherm with solid line indicating critical isotherm with composition z_1 = 0.0 (–), 0.25 (–), 0.50 (–), 0.75 (–), and 1.0 (–). Saturation curve (···), critical point (★), and critical isotherm crossing dew line (●). Calculated with Helmholtz energy equation of state with estimated mixture parameters [11]. Left) Binary mixture of MM–MD_4M. Right) Binary mixture of C_2F_6–C_6F_{14}.

C_6F_{14} the compressibility factor increases and moving to ideal mixing, as is the case for MM–MD_4M in Fig. 3.18.

3.6.2 Critical Isotherm

The speed of sound is analyzed along the critical isotherm for binary mixtures of linear siloxanes and perfluorocarbons. The speed of sound along the critical isotherm is shown in Fig. 3.21 for MM–MD_4M and C_2F_6–C_6F_{14} with varying composition of the first component z_1 = 0.0, 0.25, 0.50, 0.75, and 1.0. In the case of a mixture the critical isotherm passes through the two-phase region as is shown in Section 2.2, in this case the speed of sound in the two-phase region is not taken into consideration. Fig. 3.21 shows that moving along the critical isotherm with increasing specific volume the speed of sound increases and moves to the ideal speed of sound for both binary mixtures MM–MD_4M and C_2F_6–C_6F_{14}.

This increase in speed of sound is also observed in Fig. 3.22 for the binary mixtures of MM–MD_4M and C_2F_6–C_6F_{14}. In Fig. 3.22 the speed of sound along the critical isotherm is plotted for varying composition and reduced specific volume increase from v_r 1 to 50. For both binary mixtures the speed of sound increases along the critical isotherm, moving away from the critical point. Also the non-monotonic behavior of the speed of sound decreases with varying composition showing more ideal mixing, as is expected because the critical isotherm moves towards the ideal gas region when the specific volume is increased.

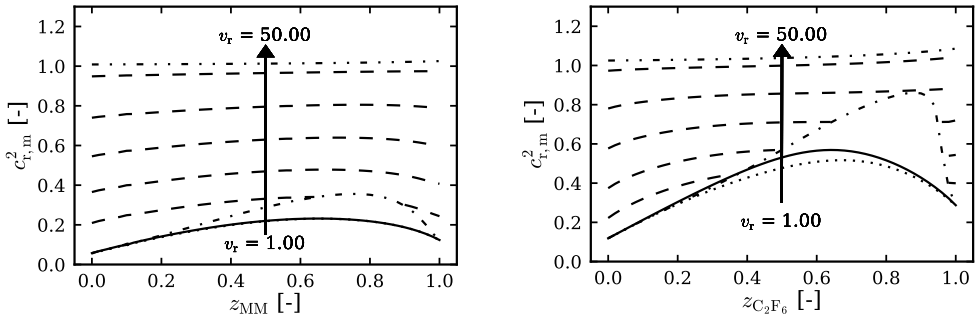

Figure 3.22: Speed of sound along critical isotherm with pressure varying from $v_r = 1$ to $v_r = 50$ and compositions varying from $z_1 = 0...1$ (– –), minimum speed of sound along dew line ($\cdots$), speed of sound at critical point (–), the critical isotherm crossing the two phase region dashed dot line (-.), and the ideal gas speed of sound dotted line (-..). Left) Binary mixture of MM–MD_4M. Right) Binary mixture of C_2F_6–C_6F_{14}.

3.7 Fundamental derivative of gas dynamics for binary mixtures

The estimation of the value of the fundamental derivative of gas dynamics Γ is of interest for fluids operating in the non-ideal thermodynamic region to indicate non-ideal compressible fluid effects as is explained in Section 1.3. The fundamental derivative of gas dynamics has special interest in the case of molecular complex fluids (e.g. siloxanes, perfluorocarbons), because of the ability to exhibit non-ideal fluid dynamics effects when Γ is smaller than one ($\Gamma < 1$). Some of these molecular complex fluids, the so-called Bethe-Zel'dovich-Thompson (BZT) fluids, can exhibit non-classical gas dynamic effects when Γ is smaller than zero ($\Gamma < 0$). The fundamental derivative of gas dynamics is defined as [19]

$$\Gamma = 1 - \frac{v}{c}\left(\frac{\partial c}{\partial v}\right)_s = \frac{v^3}{2c^2}\left(\frac{\partial^2 P}{\partial v^2}\right)_s, \tag{3.19}$$

where v is the specific volume, c the speed of sound, s the specific entropy, and P the pressure. Γ is expressed as the nonlinear variation of the speed of sound with isentropic density changes in non-dimensional form. Γ is therefore a direct derivate of the speed of sound and non-ideal or non-monotonic behavior of the speed of sound directly affects Γ. The thermodynamic definition of Γ can be rewritten so it can be obtained from a thermodynamic model being a function of the temperature and specific volume (e.g. van der Waals and Helmholtz energy model). The above formulation of Γ has to be reformulated using thermodynamic relations. After the reformulation the

following thermodynamic function of Γ follows,

$$\Gamma = \frac{v^3}{2c^2}\left\{\left(\frac{\partial^2 P}{\partial v^2}\right)_T - 3\frac{T}{c_v}\left(\frac{\partial P}{\partial T}\right)_v\left(\frac{\partial^2 P}{\partial v \partial T}\right) + \left[\frac{T}{c_v}\left(\frac{\partial P}{\partial T}\right)_v\right]^2 \times \left[3\left(\frac{\partial^2 P}{\partial T^2}\right)_v + \frac{1}{T}\left(\frac{\partial P}{\partial T}\right)_v (1 - \frac{T}{c_v}\left(\frac{\partial c_v}{\partial T}\right)_v)\right]\right\}, \tag{3.20}$$

where c_v is the isochoric specific heat and T the temperature. Each of the thermodynamics function can be obtained from a thermodynamic model using standard mathematical operations.

The first research on the effect of mixtures on the fundamental derivative of gas dynamics is conducted by Colonna et al. [20]. More recently non-classical gas dynamics of binary mixtures of organic fluids in the vapor phase is investigated by Guardone et al. [2], here the non-monotonic behavior of the fundamental derivative upon mixing is raised.

Fig. 3.23 presents the calculation of the fundamental derivative of gas dynamics along the dew curve for a mixture of MM and MD_4M with the compositions z_{MM} = 0.0, 0.25, 0.5, 0.75, and 1.0, as predicted by the Helmholtz energy model [11]. An important value of the fundamental derivative of gas dynamics is the minimum value along the dew curve or saturated vapor curve Γ_{min}, which is the smallest possible value of Γ in the vapor region. Γ_{min} indicates if a fluid can exhibit non-ideal fluid ($\Gamma_{min} < 1$) and non-classical fluid dynamic effects ($\Gamma_{min} < 0$). Γ_{min} also defines if a fluid is a BZT fluid. Fluids can also exhibit a minimum value of Γ smaller than one or zero in the two-phase region, but the two-phase region [21] is not taken into account in this research.

As is seen in Fig. 3.23 the value of Γ_{min} increases non-monotonic by mixing due to the effect of intermolecular interaction between the pure components. The maximum value of Γ_{min} in this case is given for the mixture composition of z_{MM} = 0.75. This non-monotonic behavior is similar to what is observed for the speed of sound upon mixing two components in the previous sections. This indicates the relation between the non-monotonic behavior of the speed of sound and the fundamental derivative of gas dynamics, as is expected because Γ is a direct derivative of the speed of sound. Together with the increase of the value of Γ_{min}, the region where the fluid can exhibit non-ideal and non-classical gas dynamic effects also decreases for specific compositions [22]. This increase of the value of Γ_{min} can cause a mixture of two BZT fluids to not have a negative Γ region and not classify as a BZT fluid mixtures. The increase of Γ_{min} upon mixing is important to take into, if a fluid decomposes or impurities are present in the fluid the mixture can cause an increase in Γ_{min} and a decrease of the non-ideal and non-classical gas dynamic effects region.

Fig. 3.24 presents the calculations of the fundamental derivative of gas dynamics region where Γ is smaller than one for a mixture of MM and MD_4M with compositions z_{MM} = 0.0, 0.25, 0.75, and 1.0 in the specific volume – pressure diagram. The

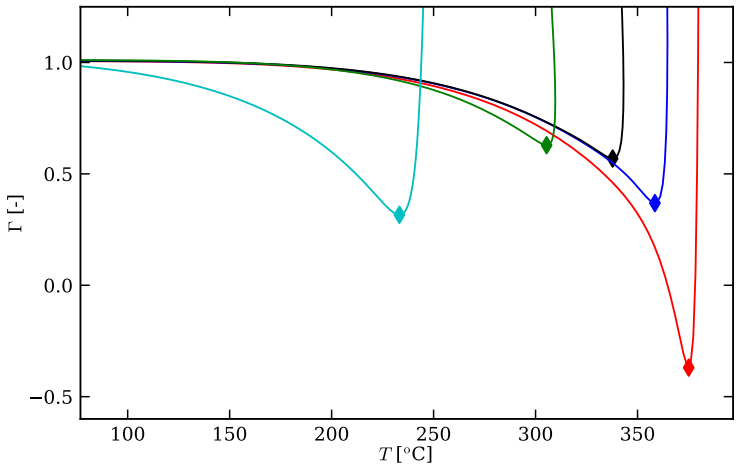

Figure 3.23: Γ as a function of temperature along the saturated vapor curve for binary mixture of MM–MD$_4$M with compositions z_{MM} = 0.0 (–), 0.25 (–), 0.50 (–), 0.75 (–), and 1.0 (–). The diamond (⧫) indicates the minimum value of Γ_{min} along the saturation curve.

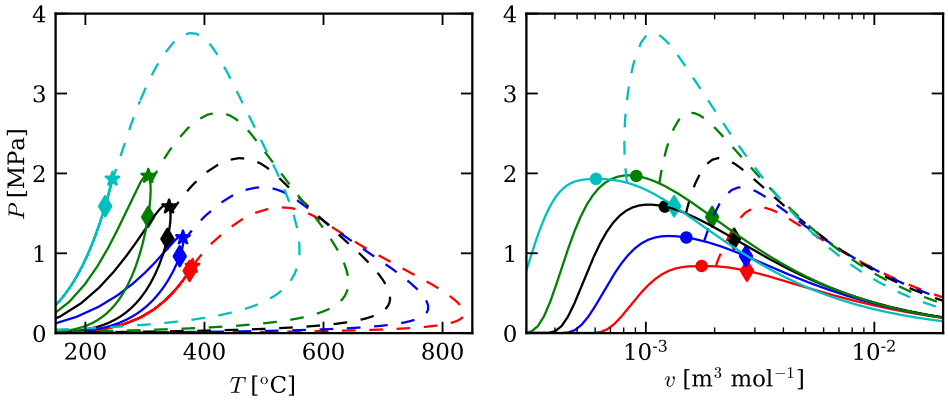

Figure 3.24: Γ = 1 curves for binary mixture MM–MD$_4$M with composition z_{MM} = 0.0 (–), 0.25 (–), 0.50 (–), 0.75 (–), and 1.0 (–). The minimum value Γ_{min} is indicated by the diamond (⧫). Left) *P*–*T* thermodynamic plane. Right) *P*–*v* thermodynamic plane.

saturation curve, the critical point, and the point of minimal Γ_{min} are also indicated in Fig. 3.24. It is observed that the position of Γ_{min} with respect to temperature, pressure, and specific volume also shifts with changing composition. The Γ smaller than one region is also shifted with changing composition.

In the next following, the non-monotonic behavior of the fundamental derivative of gas dynamics for binary mixtures of linear siloxanes and perfluorocarbons will be investigated. The research will be limited to the investigation of the minimum value of Γ along the dew curve, because the minimum value directly indicates if a fluid

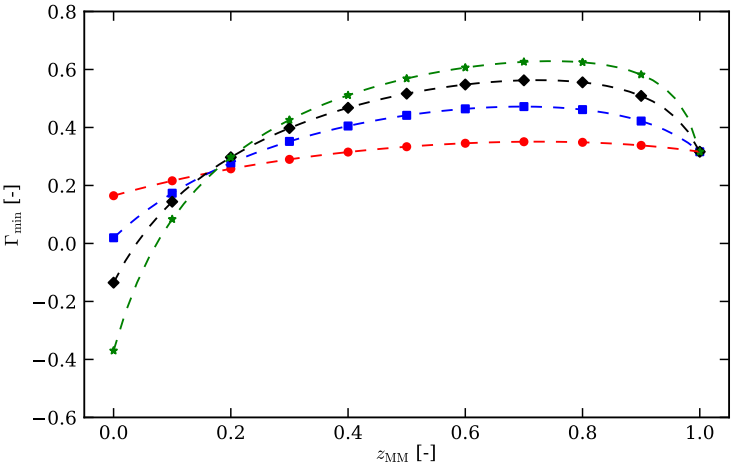

Figure 3.25: Γ_{min} evaluated along the dew curve. Evaluated for selected binary mixture combinations of MM with MDM (●), MD_2M (■), MD_3M (◆), and MD_4M (★), with compositions varying from $z_{MM} = 0...1$. Calculated with Helmholtz energy equation of state [11].

exhibits non-ideal and non-classical gas dynamic effects.

The minimum value of Γ is calculated for binary mixture of MM with MDM, MD_2M, MD_3M, and MD_4M with varying compositions. Γ is calculated with the Helmholtz energy model implemented in REFPROP [11]. Fig. 3.25 shows that the value of Γ_{min} increases non-monotonic with changing composition. The non- monotonic behavior also increases with increasing molecular complexity between the pure components in the mixtures, with the largest non-monotonic behavior for the binary mixture MM–MD_4M. Due to the non - monotonic behavior the largest value of Γ_{min} is obtained by a mixture of MM–MD_4M around $z_{MM} \approx 0.8$. The variation of Γ_{min} with the mole fraction of a binary mixture, for any given composition, is always larger than the molar fraction-averaged value of Γ_{min} of the two pure components.

Fig. 3.26 presents the reduced speed of sound and compressibility factor at Γ_{min}. The speed of sound and compressibility factor also exhibit non-monotonic behavior, similar to the value of Γ_{min}. This non-monotonic behavior of the speed of sound and compressibility factor also occurs at the critical point and along the dew curve as is shown in Sections 3.6 and 3.6.1. This shows the relation between the non-monotonic behavior of the critical point speed of sound and critical compressibility factor and the value of Γ_{min}. This can also be seen in Fig. 3.24 where the saturation curve and consequently the position of Γ_{min} in the v-P and T-P diagram is shifted upon mixing. The temperature, pressure and specific volume at the point Γ_{min} are shown in Fig. 3.26. The temperature follows a non-ideal behavior for varying composition, similar to the critical point speed of sound. The temperature shows a small non-monotonic behavior close to the less complex component, MM, in the mixture. The specific volume follows non-linear behavior for MM with MDM, MD_2M, and

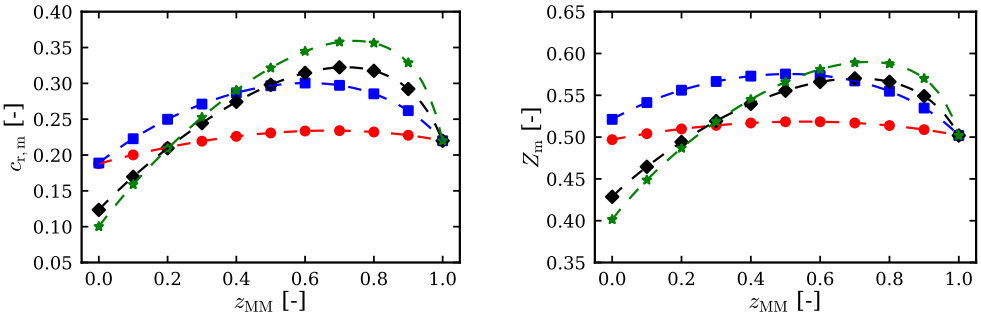

Figure 3.26: Reduced speed of sound and compressibility factor at the minimum value Γ_{min} along the dew curve. Evaluated for selected binary mixture combinations of MM with MDM (●), MD_2M (■), MD_3M (♦), and MD_4M (★), with compositions varying from $z_{MM} = 0...1$. Calculated with Helmholtz energy equation of state [11].

MD_3M, small non-monotonic behavior is observed for MM with MD_4M. Notable is the behavior of MM with MD_2M and the specific volume of pure MD_2M, which is larger than the specific volume of pure MD_3M. This notable behavior is also observed in Fig. 3.26 for the speed of sound and critical compressibility factor, where the value of pure MD_2M is larger than for pure MDM. This has to be examined in more detail to exclude a possible error in the equation of state used for the calculation of pure MD_2M. The same results for the non-monotonic behavior of Γ_{min} and thermodynamic properties at Γ_{min} are obtained for perfluorocarbons and alkanes, using the Helmholtz energy model.

3.8 Conclusion

In this chapter the speed of sound of binary mixtures composed of linear siloxanes and perfluorocarbons were investigated. The polytropic van der Waals model with one fluid mixing rules was used to explore the qualitative effect of molecular forces on the speed of sound of linear siloxane and perfluorocarbon binary mixtures. The influence of attractive forces, repulsive forces, molecular complexity, and critical properties of the mixture on the speed of sound were thoroughly analyzed.

Varying composition causes a non-monotonic behavior of the speed of sound with a parabolic behavior, meaning a maximum of the speed of sound was observed for a mixture of the pure components. This shows that the interaction between the components in the binary mixture influences the speed of sound behavior and a mixture has a larger speed of sound than the less complex pure fluid of the mixture. Increasing the molecular complexity difference between the pure components increases the non-monotonic behavior of the speed of sound.

The effect of the interaction between the pure components was clearly observed in the attractive and repulsive forces. With varying composition the reduced attrac-

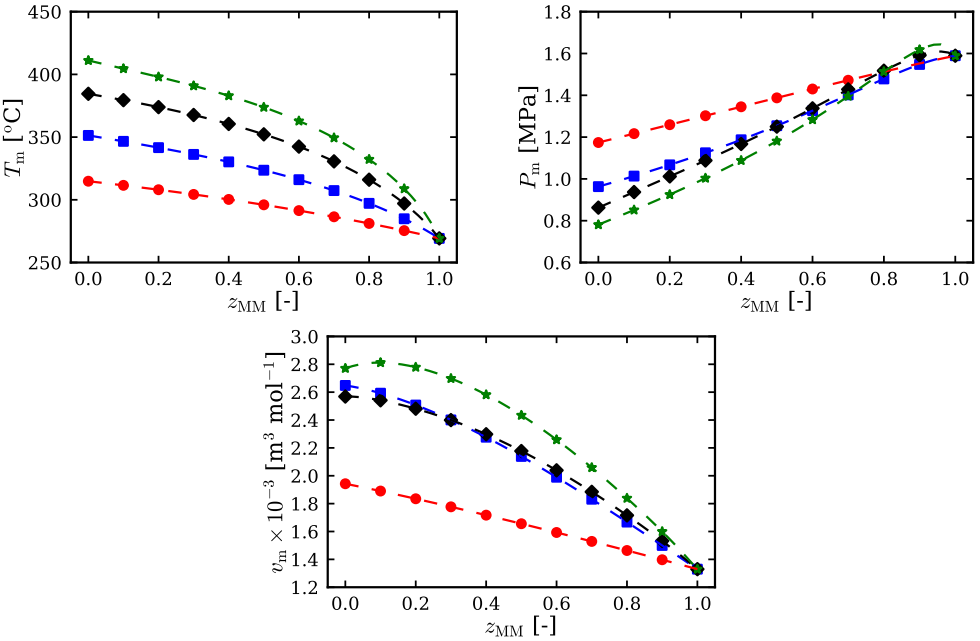

Figure 3.27: Thermodynamic properties, temperature T, pressure P, and specific volume v at minimum value Γ_{min} along the dew curve. Evaluated for selected binary mixture combinations of MM with MDM (●), MD_2M (■), MD_3M (◆), and MD_4M (★), with compositions varying from $z_{MM} = 0...1$. Calculated with Helmholtz energy equation of state [11].

tive and repulsive forces decreased, following a parabolic behavior with a minimum at different compositions. This directly relates to the attractive and repulsive speed of sound contributions. The attractive contribution has the largest influence on the non-monotonic behavior of the speed of sound and is directly related to the critical compressibility factor. It is shown that the non-monotonic behavior of the mixtures speed of sound depends mostly on the critical compressibility factor. Combining fluids decreases the attractive forces between the molecules in the siloxane mixture, which resulted in an increase of the critical compressibility factor of the mixture to unity and ideal gas behavior and therefore the speed of sound. This means that the variation of the critical compressibility factor with changing composition of the mixture gives a direct indication of the mixtures speed of sound behavior. For binary mixtures of linear siloxanes the attractive force decrease and the critical compressibility factor increase, causing the increase of the speed of sound upon mixing. This showed that the molecules are acting more repulsively which decrease the compression of the molecules and increase the speed of sound. This indicates that combining components with increasing attractive forces between the molecules upon mixing can decrease the speed of sound.

A notable behavior between the binary mixtures of linear siloxanes and perfluo-

rocarbons was observed. The critical pressure of the linear siloxane mixtures show a non-linear behavior and for the perfluorocarbon mixtures a non-monotonic behavior. Also, the repulsive mixture parameters show opposite trends between linear siloxanes and perfluorocarbons, which directly affects the repulsive force contribution of the speed of sound. This difference should be investigated in more detail in future research to obtain a better understanding of the mixing rules and the combining of different fluids within a mixture.

The van der Waals model with one fluid mixing rules is not accurate in the non-ideal gas region and it underestimates the value of the speed of sound. The van der Waals model gives only a qualitative reasonable approximation of the thermodynamic properties. The accurate and state-of-the-art Helmholtz energy equation of state was used to verify the non-monotonic speed of sound behavior for binary mixtures of linear siloxanes and perfluorocarbons. The non-monotonic behavior of the critical compressibility factor was also verified by the Helmholtz energy equation of state. The other critical properties also show qualitative good agreement with the van der Waals model, except for the critical pressure of the linear siloxanes which exhibits a non-monotonic behavior for the Helmholtz energy equation of state which is not observed with the van der Waals model. This difference between the Helmholtz energy model and van der Waals model should be investigated in more detail in future research. A more in depth research would allow for a better understanding of the influence of other molecular characteristics (e.g. polarity, acentricity, etc.) and thermodynamic models on the mixture thermodynamic properties.

Finally, the effect of non-ideal mixing on the fundamental derivative of gas dynamics was investigated using the Helmholtz energy equation of state. The behavior of Γ was analyzed for binary mixtures of linear siloxanes. The increasing non-monotonic behavior by varying the composition of the mixtures is also occurring for Γ. The dependence of the minimum value Γ_{min} was investigated with varying composition. The non-monotonic behavior of Γ_{min} also increases with increasing molecular complexity between the components in the mixtures. Furthermore, the speed of sound and compressibility factor also exhibit increasing non-monotonic behavior at the position of Γ_{min}. The value of Γ_{min} of the mixture is always greater than the value of Γ_{min} of the most complex molecule in the mixture. This increasing non-monotonic behavior is similar to the behavior of the speed of sound and compressibility factor at the critical point. This shows that the change in critical properties upon mixing directly relates to Γ and the capability of the fluid to exhibit non-ideal fluid dynamic effects or non-classical gas dynamics effects. The same behavior was observed for binary mixtures of perfluorocarbons and alkanes, indicating that the value of Γ_{min} always increases for mixtures of the same family.

References

[1] E. W. Lemmon, M. O. McLinden, and W. Wagner. "Thermodynamic Properties of Propane. III. A Reference Equation of State for Temperatures from the Melting Line to 650 K and Pressures up to 1000 MPa". In: *Journal of Chemical & Engineering Data* 54.12 (2009), pp. 3141–3180. DOI: 10.1021/je900217v.

[2] A. Guardone, P. Colonna, E. Casati, and E. Rinaldi. "Non-classical gas dynamics of vapour mixtures". In: *J. Fluid Mech.* 741 (2014), pp. 681–701. DOI: https://dx.doi.org/10.1017/jfm.2013.13.

[3] P. Colonna, A. Guardone, and N. R. Nannan. "Siloxanes: A new class of candidate Bethe-Zel'dovich-Thompson fluids". In: *Phys. Fluids* 19.8 (2007), p. 086102. DOI: 10.1063/1.2759533.

[4] P. Colonna and A. Guardone. "Molecular interpretation of nonclassical gas dynamics of dense vapors under the van der Waals model". In: *Phys. Fluids* 18.5, 056101 (2006). DOI: https://dx.doi.org/10.1063/1.2196095.

[5] P. Colonna and T. P. van der Stelt. *Fluidprop: A program for estimation of thermophysical properties of fluids*. Software. 2004. URL: http://www.FluidProp.com.

[6] N. R. Nannan, C. Sirianni, T. Mathijssen, A. Guardone, and P. Colonna. "The admissibility domain of rarefaction shock waves in the near-critical vapour–liquid equilibrium region of pure typical fluids". In: *J. Fluid Mech.* 795 (2016), pp. 241–261. DOI: 10.1017/jfm.2016.197.

[7] P. A. Thompson and K. C. Lambrakis. "Negative shock waves". In: *J. Fluid Mech.* 60.1 (1973), pp. 187–208. DOI: 10.1017/S002211207300011X.

[8] P. Colonna and A. Guardone. "Molecular interpretation of nonclassical gas dynamics of dense vapors under the van der Waals model". In: *Phys. Fluids* 18.5, 056101 (2006). DOI: 10.1063/1.2196095.

[9] R. A. Heidemann and A. M. Khalil. "The Calculation of Critical Points". In: *AIChE J.* 26.5 (1980), pp. 769–779. ISSN: 1547-5905. DOI: 10.1002/aic.690260510.

[10] T. Y. Kwak and G. A. Mansoori. "Van der waals mixing rules for cubic equations of state. Applications for supercritical fluid extraction modelling". In: *Chem. Eng. Sci.* 41.5 (1986), pp. 1303–1309. ISSN: 0009-2509. DOI: 10.1016/0009-2509(86)87103-2.

[11] E. W. Lemmon, I. H. Bell, M. L. Huber, and M. O. McLinden. *NIST Standard Reference Database 23: Reference Fluid Thermodynamic and Transport Properties - REFPROP, Version 10*. 2018.

[12] M. Thol, F. Dubberke, G. Rutkai, T. Windmann, A. Köster, R. Span, and J. Vrabec. "Fundamental equation of state correlation for hexamethyldisiloxane based on experimental and molecular simulation data". In: *Fluid Phase Equilib.* 418.Supplement C (2016). Special Issue covering the Nineteenth Symposium on Thermophysical Properties, pp. 133–151. ISSN: 0378-3812. DOI: 10.1016/j.fluid.2015.09.047.

[13] M. Thol, F. H. Dubberke, E. Baumhögger, J. Vrabec, and R. Span. "Speed of Sound Measurements and Fundamental Equations of State for Octamethyltrisiloxane and Decamethyltetrasiloxane". In: *Journal of Chemical & Engineering Data* 62.9 (2017), pp. 2633–2648. DOI: 10.1021/acs.jced.7b00092.

[14] König and M. Thol. "Helmholtz equation of state for Dodecamethylpentasiloxane (MD_3M) and Tetradecamethylhexasiloxane (MD_4M)". To be published. 2017.

[15] D. Ambrose, C. Tsonopoulos, and E. D. Nikitin. “Vapor Liquid Critical Properties of Elements and Compounds. 11. Organic Compounds Containing B + O; Halogens + N, + O, + O + S, + S, + Si; N + O; and O + S, + Si”. In: *Journal of Chemical & Engineering Data* 54.3 (2009), pp. 669–689. DOI: 10.1021/je800580z.

[16] E. W. Lemmon and R. Span. “Short Fundamental Equations of State for 20 Industrial Fluids”. In: *Journal of Chemical & Engineering Data* 51.3 (2006), pp. 785–850. DOI: 10.1021/je050186n.

[17] K. Gao, J. Wu, and E. W. Lemmon. Helmholtz equation of state for perfluorobutane, perfluoropentane, and perfluorohexane, to be published. 2017.

[18] O. Kunz and W. Wagner. “The GERG-2008 Wide-Range Equation of State for Natural Gases and Other Mixtures: An Expansion of GERG-2004”. In: *Journal of Chemical & Engineering Data* 57.11 (2012), pp. 3032–3091. DOI: 10.1021/je300655b.

[19] W. D. Hayes. *Gasdynamic Discontinuities*. Princeton University Press, 1960. URL: http://www.jstor.org/stable/j.ctt183pmwn.

[20] P. Colonna and P. Silva. “Dense Gas Thermodynamic Properties of Single and Multicomponent Fluids for Fluid Dynamics Simulations”. In: *J. Fluids Eng* 125.3 (2003), pp. 414–427. DOI: https://dx.doi.org/10.1115/1.1567306.

[21] N. R. Nannan. “Advancements in Nonclassical Gas Dynamics”. PhD thesis. Delft University of Technology, 2009.

[22] A. Guardone and B. M. Argrow. “Nonclassical gasdynamic region of selected fluorocarbons”. In: *Phys. Fluids* 17.11 (2005), p. 116102. DOI: 10.1063/1.2131922.

CHAPTER 4

BUBBLE-POINT MEASUREMENTS AND MODELING OF LINEAR SILOXANES BINARY MIXTURES

The content of this chapter is in preparation for publication:

L. Keulen, E. Mansfield, I. H. Bell, A. Spinelli, and A. Guardone. "Bubble-point measurements and modeling of linear siloxanes binary mixtures". In preparation for submission to: *Journal of Chemical and Engineering Data*. 2018.

4.1 Introduction

The need for high quality thermophysical property data with thoroughly assessed sources of uncertainty is of great importance [1]. The data measured are important for the development of high accuracy equations of state for the prediction of the thermophysical properties of a fluid over large ranges of temperature and pressure. In turn, the predicted properties can be used for efficient design of power cycles as well as other industrial processes like chemical manufacturing and air conditioning. For the development of a reliable equation of state, vapor-liquid equilibrium (VLE) and homogeneous density data are required. To obtain well established calculation of caloric properties, isobaric heat capacity, and speed of sound data are required.

As mentioned VLE is a key thermophysical property and accurate VLE data is necessary for model development of equations of state to predict thermophysical properties. Knowledge about the phase change of pure fluids and mixtures is of paramount importance for the design and operation of industrial and research applications. Knowing the temperature and pressure at which these changes take place allow for more efficient use of the fluid. To determine phase behavior of pure fluids, temperature and pressure need to be measured, for mixtures it is also necessary to know the composition of the mixture. The two main methods to determine VLE for mixtures are the analytical and the synthetic method. They differ on how the composition of the equilibrium phases are determined. The analytical method involves the analytical determination of the composition of the coexisting phases. In the analytical method it is not necessary to exactly know the overall composition of the mixture when the fluid is loaded into the equilibrium cell. The composition of the coexisting phases of the mixture is analyzed with sampling using chemical analysis or without sampling by using physiochemical methods of analysis inside the equilibrium cell. For the synthetic method, the mixture is prepared with a precisely known composition and then the prepared mixture is loaded into the equilibrium cell and the properties are measured in the equilibrium state. An extensive review about the analytical and synthetic methods for the measurements of VLE data is given by Fonseca et al. [2].

The equipment for the bubble-point measurements used in this work is based on the synthetic method, where a precisely known mixture composition is made gravimetrically offline. The synthetic method yields pressure, temperature, and liquid composition data. Which in comparison with analytical instrumentation returns pressure, temperature, liquid and vapor composition data. The synthetic methods allows for more simplistic equipment design because the composition does not have to be determined. Simpler equipment allows for the sources of uncertainty to be identified and accounted for in a way that analytical methods do not. By eliminating sampling valves and composition determining instrumentation (e.g. gas chromatography), which most analytical methods use [2, 3], the uncertainty in potential composition changes that occur when volume is removed from the system are eliminated.

In addition, a double substitution weighing design to determine composition ensures that the composition of the mixture is well known, extreme care in calibration of pressure transducers is accomplished with a dead weight pressure balance, and temperatures are calibrated using a three point calibration for highest precision [4]. These measures ensure that the sources of uncertainty are well characterized.

In this work bubble-point pressure measurements of binary mixtures of linear siloxane fluids are conducted. The obtained bubble-point pressure data are used to improve the current equation of state for the binary mixtures of linear siloxanes by modeling new mixture parameters. The measurements and modeling are performed at the National Institute of Standards and Technology. Pure siloxane working fluids are already prominent, successful working fluids for instance Organic Rankine Cycles (ORCs). Mixtures of siloxanes are promising working fluids for ORCs [5]. The use of ORCs as power cycles has increased significantly the last few decades and is now a widely used technology for small to medium power generation. They are used in many different applications, from industrial waste heat recovery to renewable energy application, such as solar, biomass and geothermal energy [6–9]. For binary mixtures of linear siloxane only one data set exists, which is conducted by Abbas [10], and no binary mixture parameters have been modeled for these mixtures so far, prompting the need for additional measurements and mixture modeling.

The structure of this work is as follows. Firstly, Section 4.2 describes the linear siloxane fluids measured and modeled in this work. In Section 4.3 the details of the bubble-point pressure measurement equipment are given, describing the various components of the apparatus and their specifications. Subsequently the mixture preparation is elaborated as well as the procedure for the measurement of the bubble-point pressure in Section 4.4. The data analysis consisting of the analysis of the vapor quality in the equilibrium cell and the thorough uncertainty analysis is discussed in Section 4.5. The results and discussion of the bubble-point measurements are presented in Section 4.6 and in addition an analysis of the impact of air impurity on the bubble-point pressure is conducted. Section 4.7 treads the modeling of new binary interaction parameters for the Helmholtz energy model employing the measured bubble-point pressures. Finally, in Section 4.8 concluding remarks and recommendations for future research are given.

4.2 Materials

The fluids were obtained from commercial sources and used without further purification, the stated manufacturer purity is listed in Table 4.1. The purity of the fluids were measured through chemical analysis and these purities are reported in Table 4.1.

The purity of the fluids were determined through in house laboratory chemical analysis; for this purpose samples were taken and analyzed by High resolution gas chromatography (HRGC) by using a gas chromatograph equipped with capillary columns attached to a mass spectrometer (MS). Spectral peaks were interpreted

Table 4.1: Measured and manufacturer determined purity of the components.

Chemical	Chemical formula	CAS number	Manufacturer	GC-MS
MM	$C_6H_{18}OSi_2$	107-46-0	$>$ 99.4%	99.75 %
MDM	$C_8H_{24}O_2Si_3$	107-51-7	$>$ 99.7%	99.97 %
MD_2M	$C_{10}H_{30}O_3Si_4$	141-62-8	$>$ 99.3%	99.81 %
MD_3M	$C_{12}H_{36}O_4Si_5$	141-63-9	$>$ 98.0%	99.80 %

with guidance from the NIST/EPA/NIH Mass Spectral Database [11] and the Wiley Registry of Mass Spectral Data [12]. The area of the spectral peaks with respect to the largest area peak is obtained and the relative peak percentage is calculated to determine the purity. Because the chemical analysis purities are given in relative percentage between the detected components, this percentage does not correspond to the molar or mass fraction of each component. The chemical analysis allowed for the quali-quantitative analysis of the fluids purity. More details about the apparatuses used for the chemical analysis are given in Section 5.3.4.

4.3 Experimental apparatus

The schematic design of the experimental apparatus is shown in Fig. 4.1. The apparatus design is based on an previous apparatus at the National Institute of Standards and Technology [13]. The heart of the apparatus is the equilibrium cell constructed of stainless steel and is of high thermal mass to maintain stable temperature control for the duration of the measurement. Temperature is measured using a standard platinum resistance thermometer (SPRT) and pressure is measured using a calibrated oscillating quartz pressure transducer maintained at a constant temperature of 313 K.

Heating and cooling is achieved through a two-stage system; the first stage is formed by a copper sleeve immediately around the equilibrium cell providing direct heat to the cell during the temperature ramp and trim heating once at the equilibrium temperature up to 380 K. The second stage of the thermostat region consists of a copper box around the equilibrium cell and also contains the majority of the valves and tubing. The copper box provides consistent heating throughout the measurement to ensure temperature effects from the room do not influence the cell during the measurement. Cooling also occurs at the copper box by circulating cooling fluid from the circulator system to reach temperatures down to 265 K.

4.3.1 Equilibrium cell

The cylindrical equilibrium cell houses the fluid undergoing the testing. The cell is constructed from 316 stainless steel with an internal diameter of 22.2 mm, outer diameter of 62.8 mm, and an internal length of 76.2 mm; the internal volume is

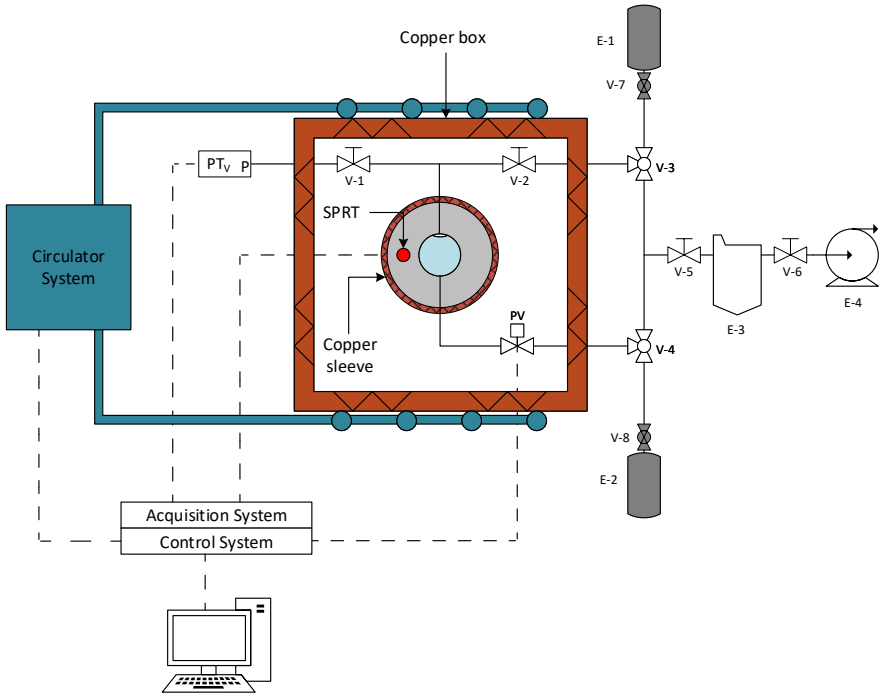

Figure 4.1: Schematic diagram of the Vapor-Liquid equilibrium experimental apparatus: pressure transducer vapor side (PT_V), standard platinum resistance thermometer (SPRT), valves (V), pneumatic valve (PV), sample vessel (E-1), waste vessel (E-2), cold trap (E-3), vacuum pump (E-4).

approximately 30 ml. At each end, the cell has sapphire windows with a thickness of 12.8 mm and diameter of 31.6 mm so that the liquid level in the cell can be observed and controlled as shown in Fig. 4.3. The windows are held in place by bolted flanges and sealed with fiberglass impregnated polytetrafloroethylene (PTFE) gaskets on both sides of the windows. The cell has four ports for 3.175 mm outer diameter tubing connections to valves and the rest of the system.

4.3.2 Thermostat system

The first stage in the thermostat system is a 5.0 mm thick copper sleeve immediately around the equilibrium cell. Flexible heaters on the copper sleeve allow for indirect heating of the equilibrium cell. The copper sleeve is maintained at the equilibrium set point temperature of the equilibrium cell.

The second stage in the thermostat system region is a copper box. The box is centered around the equilibrium cell and has an overall dimensions of 216.0 mm $\times$ 178.0

Figure 4.2: Vapor-liquid equilibrium apparatus.

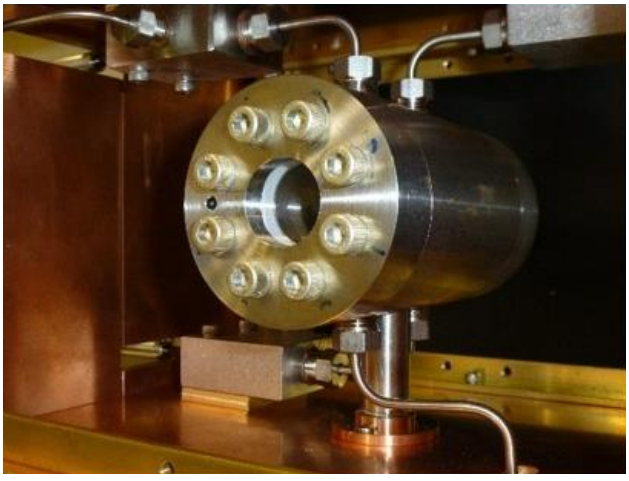

Figure 4.3: Equilibrium cell.

Figure 4.4: Thermostat system.

mm × 140.0 mm and a wall thickness of 6.35 mm. The box is fitted with flexible heaters as well as cooling coils for temperature control of the system. These heaters are heated by providing electrical power during the heating phase and are controlled to trim heating during the equilibrium phase to maintain a constant temperature.

For cooling, 9.5 mm outer diameter copper tubing has been brazed to the top and bottom of the box in a serpentine configuration for circulation of cooling fluid when the system is running at sub-ambient temperatures. The cooling fluid is a mixture propylene glycol and water and is circulated by a pump embedded in the thermal bath.

The copper box is contained in a framed aluminum box. Both the inside of the copper box and the area between the copper and aluminum boxes are filled with mineral wool insulation. The thermostat system is capable of maintaining the equilibrium set-point temperature (as measured by the main SPRT) within ±5 mK.

4.3.3 Temperature system

Temperature is measured in the wall of the equilibrium cell using a SPRT. The SPRT was calibrated using the fixed-point cells and the procedures outlined by Preston-Thomas [4]. Calibration points are a gallium melting point cell (302.9146 K) and the freezing point cell of indium (429.7485 K), each kept in their own thermostat or furnace. A water triple-point cell (273.16 K) was used as the final temperature calibration. The uncertainty for the temperature standards ranges from 0.2 mK K to 2 mK. All calibration points were measured using the multimeter used within the VLE

apparatus. The copper box is maintained at ± 3 K below the equilibrium set-point temperature of the equilibrium cell. Because an accurate temperature measurement is not necessary for the copper box, the temperature is monitored with a ceramic resistance temperature detector (RTD) fitted to the inner portion of the copper box and recorded using a multimeter equipped with a scanning card.

4.3.4 Pressure system

The pressure of the system is measured by using an oscillating quartz-crystal pressure transducer (PT) in the vapor phase in the equilibrium cell. The PT has a range up to 700 kPa and is located outside the copper box 50 mm above the center of the equilibrium in an aluminum housing. The PT is calibrated with a NIST-traceable dead-weight pressure gauge at 313 K. The manufacturer stated the uncertainty as 0.01% of full range, equating to 0.07 kPa. However, with regular calibration and maintaining the PT at a constant temperature (313 K) during pressure measurements, the uncertainty can be reduced to 0.005% of the full range, equating to 0.035 kPa. As a conservative estimate of pressure uncertainty, the manufacturer's recommendation of 0.01% of the full range is used. The pressure was monitored using transducer readouts coupled with the acquisition system and computer.

The PT is kept at a constant temperature of 313 K during all pressure measurements of the experiment. The heating of the PT is done via flexible heaters on the aluminum box housing the PT. The temperature control of the aluminum housing is achieved with a commercially available controller that monitors the temperature using a type K thermocouple.

4.3.5 Additional equipment

All tubing between the equilibrium cell, valves, and pressure transducer is 3.2 mm outer diameter stainless steel tubing. The sample is loaded into the equilibrium cell from the stainless steel sample cylinder E-1 of 300 ml coupled to the apparatus. The three-way valve V-3 was placed between the sample loading tube and the system in order to be able to isolate the loading area and evacuate all the tubing and the equilibrium cell. The valve V-2 between the three-way valve V-3 and the equilibrium cell is used to load the sample through the top port of the equilibrium cell. The port on the bottom of the equilibrium cell is coupled to a pneumatic valve PV. The pneumatic valve PV is used to evacuate fluid from the equilibrium cell, to regulate the liquid level, and acts as a safety mechanism to prevent over-pressurizing the system. The pneumatic valve PV is controlled via the computer and the opening time of the pneumatic valve PV can be varied. The outlet of the pneumatic valve PV is connected to a three-way valve V-4 which is then connected to a stainless steel cylinder for waste collection E-2 and the vacuum system consisting of the cold trap E-3 and vacuum pump E-4. The system can be isolated from the vacuum system through valve V-

8. The vapor phase pressure transducer PT_v is connected with the equilibrium cell through valve V-1.

All tubing and connections are verified to be sealed with pressurized helium and under vacuum. The vacuum pump equipped with a cold trap is used to evacuate the entire system, including the equilibrium cell, tubing and waste cylinder prior to loading the sample.

4.3.6 Electronics and acquisition system

The apparatus data acquisition program monitors the temperature and pressure, controls the power supply for heating, the circulator for cooling, and the pneumatic valve. The program runs an automated loop of a temperature queue set for the test.

Below 300 K, the temperature control program turns on and set the temperature of the the circulatro, and the heating system is used to shim the temperature and provide stability. Above 300 K, the equilibrium cell is heated by the heating system. The temperature control program is a Proportional-Integral-Derivative (PID) routine. Two independent PID controllers are used for controlling the two heating stages, i.e. the copper sleeve and the copper box. In a feedback loop, the PID controller determines the necessary voltage to reach and then maintain the set-point temperature. The voltage information is transmitted via an IEEE 488 interface to programmable power supplies that power the heaters of the copper sleeve and copper box.

The pressure transducer data is monitored through an USB-to-Serial connection. Calibrations are used to update the pressure transducer coefficients prior to utilizing the pressure transducer in the equilibrium apparatus. The SPRT and RTD are monitored using a multimeter with a scanning card. Temperature and pressure measurements are recorded every 90 seconds.

Equilibrium in the cell is determined by monitoring the temperature. Once sufficient stability is achieved, as defined by tunable convergence criteria, the system is maintained at the equilibrium temperature for 8 hours to ensure equilibrium between the liquid and gas phase is achieved. After the 8 hours equilibrium hold the bubble-point pressure and temperature data is collected for 15 minutes. The collected 15 minutes of bubble-point pressure and temperature data are averaged and recorded as one equilibrium point. After the data collection is completed the software sets the next set-point temperature in the queue and starts heating and the measurement process starts again.

Several safety checks for the system are incorporated into the software. Temperature and pressure limits are set to initiate a safety stop on the system if the system temperature exceeds 410 K or if the pressure reaches 670 kPa; pressures above 670 kPa can damage the pressure transducer. If the safety limits are reached, all heating of the system is stopped. The system could potentially over-pressurize if the vapor phase bubble disappears and a compressed liquid is formed inside the equilibrium cell. If this happens, the pressure rise will trigger the program to open the pneumatic

valve and release a small volume of sample into the waste line. If the pneumatic valve cannot compensate the pressure increase by releasing liquid, a safety stop is initiated and all heating ceases. The pneumatic valve can also be triggered manually through the software to control the bubble size.

4.4 Measurement procedure

The measurement procedure is divided into two parts: the preparation of the mixture sample and the bubble point measurement.

4.4.1 Mixture preparation

The mixtures are prepared gravimetrically in sealed 300 ml stainless steel cylinders. Mixtures are prepared with the goal of filling the sample cylinder with approximately 280 ml of liquid at the target composition, at ambient temperature. After the weighing of the empty cylinder, the first component is added to the cylinder. In this work MM is always loaded as the first component. After the first component is loaded, the vessel is closed and the vapor space is degassed by freezing the fluid in liquid nitrogen and evacuating the head space. After evacuation, the cylinder is heated to drive impurities in the liquid into the vapor space. This cycle of freezing/evacuating/heating/thawing is repeated at least three times and a maximum of fifteen times, depending on each sample to allow for a complete degassing of the sample. After completion of degassing the cylinder is weighted to determine the amount of fluid of the first component. Next, the second component is added into the vessel and the cycle of freezing/evacuating/heating/thawing is repeated and the completed mixture is weighted to determine the total amount of the second component.

The weighing of the sample cylinder is conducted following the double substitution weighing design of Harris et al. [14]. A balance with a precision of 0.1 mg is used in the preparation of the mixture. Measurement of the mass of the empty cylinder and each component consists of weighing four masses: (1) a reference cylinder of approximately the same mass and volume as the empty sample cylinder, (2) the sample cylinder, (3) the sample cylinder plus a 20 g sensitivity weight, and (4) the reference cylinder plus the 20 g sensitivity weight. This weighing sequence is repeated four times for each mass determination. The density of ambient air is calculated based on measurements of temperature, pressure, and relative humidity, and the weighings are corrected for the effects of air buoyancy [15]. The uncertainty of the measured mixture composition is discussed in detail in Section 4.5.2.

4.4.2 Bubble-Point measurement

The system is evacuated and then cooled to 265 K. The sample cylinder is heated for 15 minutes to an estimated temperature of 313 K. The heating is performed to pro-

mote convection mixing in the vessel and ensure the sample is adequately mixed and homogenized prior to loading into the equilibrium cell which is under vacuum. The sample is loaded by opening the sample valve and allowing the liquid mixture sample to flow gravimetrically and by the temperature difference into the the equilibrium cell. Because the loading volume is very limited and the linear siloxanes mixtures have a very low vapor pressure, the sample remains in the liquid phase during the loading procedure, in this way bubble point measurements on a sample of fixed composition are obtained. The equilibrium cell is filled completely, with the exception of a small vapor space called the "bubble" at the top of the cell. The bubble is kept as small as possible to ensure the vapor composition and bulk liquid composition are equivalent when the system reaches equilibrium. Prior to loading, the vacuum pressure is recorded and measured pressures have been adjusted to reflect any offset. Due to the low vapor pressure of siloxanes, a small contamination of air can have a large impact on the measurement as elaborated in Section 4.6.1. If necessary, the fluid can be degassed in situ by applying vacuum to the vapor phase of the equilibrium cell. The change in composition of the mixtures by applying vacuum to the vapor space is elaborated in Section 4.6.2.

Pressure measurements are recorded in the range between 270 K and 380 K, with increments of $\Delta T = 5$ K or $\Delta T = 10$ K. As the cell temperature is increased the liquid inside expands and it is necessary to periodically release a small amount of liquid via the pneumatic valve to maintain a vapor space on the top of the cell. When and in what amount liquid needs to be released depends on the sample and it is monitored and determined by the operator by checking the vapor space after every temperature increase.

Under this measurement protocol, attempts are made to ensure that the most accurate bubble points of the sample are measured, though several assumptions are made. These assumptions include: (i) the liquid composition in the cell is equal to the bulk composition of the mixture in the sample bottle and no composition change occurs during filling [13], (ii) during degassing of the equilibrium cell vapor space no change of the liquid bulk composition occurs, and (iii) by loading the equilibrium almost full of liquid, leaving only a very small vapor space, the pressure of the vapor phase equals the bubble-point pressure of the liquid composition at a given temperature; this is analyzed in Section 4.5.1.

4.5 Data Analysis

All processing of the data and uncertainty calculations are performed using an in-house analysis software. Modeling of the data analysis is performed using the thermodynamic model implemented in computer program REFPROP [16]. Due to the absence of binary interaction parameters for the Helmholtz energy equation of state for the mixture measured in this work the Peng-Robinson equation of state from REFPROP is used for the data analysis.

Figure 4.5: Vapor bubble and liquid phase inside equilibrium cell.

4.5.1 Vapor quality equilibrium cell

The vapor quality in the equilibrium cell is determined by an analysis of the vapor bubble and the use of the void fraction ε to characterize the two-phase regions. The analysis is carried out in order to justify the assumption that the measurements are performed at the bubble point. This analysis provides an indication of the change in vapor quality with vapor bubble size and temperature increase through estimated properties using the thermodynamic model.

A cross section area of the equilibrium cell is shown in Fig. 4.6, here the dark gray area A_v represents the vapor bubble within the cell. The cross-section void fraction is defined as [17]

$$\varepsilon = \frac{A_\mathrm{v}}{A_\mathrm{v} + A_\mathrm{l}}, \tag{4.1}$$

where A_v is the cross-sectional area of the cell occupied by the vapor phase and A_l the area of the liquid phase. The areas of the vapor and liquid phase are calculated through trigonometry. The geometric parameters are defined as

$$r = h + t \qquad\qquad s = r\theta, \tag{4.2}$$

$$t = \frac{1}{2}\sqrt{4r^2 - a^2} \qquad\qquad a = 2\sqrt{h(2r-h)}, \tag{4.3}$$

where r is the radius of the cell, a the chord length, s the arc length, h the height of the vapor bubble and r the height of the triangular portion. From this the angle θ can be calculated from

$$\theta = 2\sin^{-1}\left(\frac{a}{2r}\right). \tag{4.4}$$

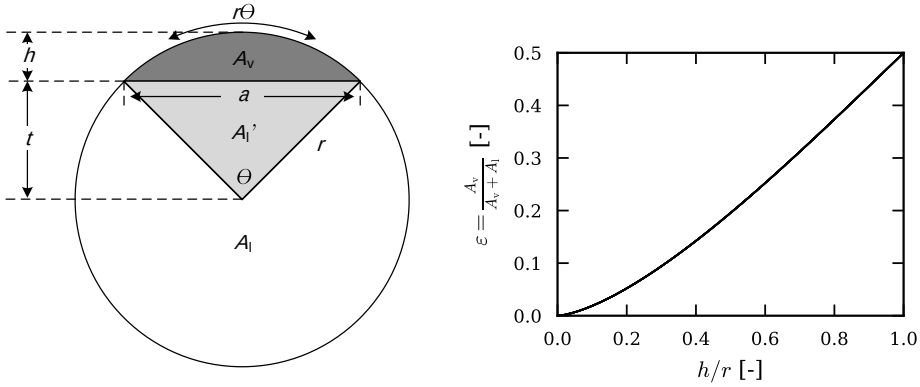

Figure 4.6: Geometric evaluation void fraction of the equilibrium cell. ε is the void fraction, A_v is the cross-sectional area of the cell occupied by the vapor phase, A_l the area of the liquid phase, r the radius of the cell, a the chord length, s the arc length, h the height of the vapor phase, and t the height of the triangular portion. Left) Schematic cross-section of the equilibrium cell. The dark gray area represents the vapor phase within the equilibrium cell. Right) Void fraction vs. height vapor phase over equilibrium cell radius.

The area of the light gray triangle A_l' and the dark gray vapor bubble sector A_v is

$$A_\mathrm{sector} = \frac{1}{2} r^2 \theta. \tag{4.5}$$

Subtracting the light gray triangle from the total area sector gives the area of the vapor phase; the area of the liquid phase is then calculated by subtracting the vapor phase area from the total cell area

$$A_\mathrm{v} = A_\mathrm{sector} - \frac{1}{2} a t, \tag{4.6}$$

$$A_\mathrm{l} = A_\mathrm{cell} - A_\mathrm{v}. \tag{4.7}$$

With the area of the vapor and liquid phase determined, the void fraction can be calculated and the void fraction versus the vapor bubble height over the cell radius is shown in Fig. 4.6. This calculation of the quality using the void fraction is purely geometric in nature.

When the void fraction is known, the vapor quality, q, can be calculated as follows

$$q = \frac{\varepsilon \rho_\mathrm{v}}{\rho_\mathrm{l}(1-\varepsilon) + \rho_\mathrm{v}\varepsilon}, \tag{4.8}$$

$$\rho_\mathrm{l} = \rho\left(T, \quad q = 0, \quad \bar{z} = \bar{z}_\mathrm{bulk}\right), \tag{4.9}$$

$$\rho_\mathrm{v} = \rho\left(T, \quad q = 0, \quad \bar{z} = \bar{z}_\mathrm{bulk}\right), \tag{4.10}$$

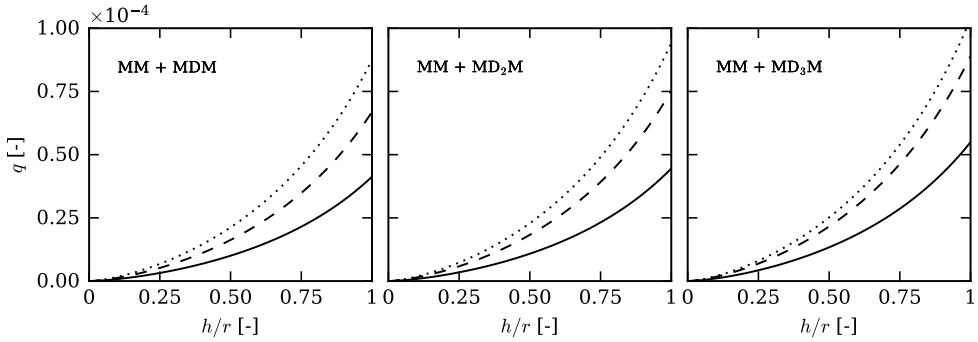

Figure 4.7: Vapor quality plotted against vapor bubble height over cell radius at T = 270 K for three compositions of each mixture of MM with MDM, MD_2M, and MD_3M. The figures show three different compositions for each mixture, mole fractions of MM is shown respectively by the solid line 25 mol% (−), dashed line 50 mol% (−−), and dotted line 75 mol% (···).

here ρ_v and ρ_l are the vapor and liquid density of the mixture respectively and $\bar{z}_{bulk}$ the bulk composition of the mixture. As an assumption, the densities of the liquid and vapor phases are calculated using the thermodynamic model at the bubble-point; because the fluid is close to the bubble-point this assumption is reasonable.

The change in vapor quality with increasing vapor bubble size is shown in Fig. 4.7 for mixtures of MM with MDM, MD_2M, and MD_3M. The vapor quality increases with larger vapor bubble size; mixtures with a larger fraction of MM show a steeper increase of the vapor quality. The vapor quality increase is very small; for all mixtures the vapor quality is less than 1×10^{-4} when the vapor phase occupies half of the cell.

The average height h of the vapor bubble is estimated by observation of the vapor bubble in the equilibrium cell after loading the mixture in the system as shown in Fig. 4.5, the average height of the vapor bubble is set at h = 3 mm. Fig. 4.8 presents the calculated vapor quality for mixtures of MM with MDM, MD_2M, and MD_3M and height h = 3 mm at the temperature range used for the measurements of the bubble-points. The vapor quality increases with increasing temperature and again the mixture with a larger fraction of MM shows a steeper increase. For all temperatures and mixtures the vapor quality remains below $q = 8 \times 10^{-4}$.

As shown in Figs. 4.7 and 4.8 the vapor quality increase for larger bubble sizes and increasing temperature is small and the assumption is plausible that, by keeping the vapor bubble small, the bubble point of the mixture is measured.

4.5.2 Uncertainty analysis

The uncertainty is calculated by standardized measurement uncertainty principles [18]. The expanded uncertainty for the bubble-point measurements is calculated by the root-sum-of-squares method [19], taking into account five principle sources of

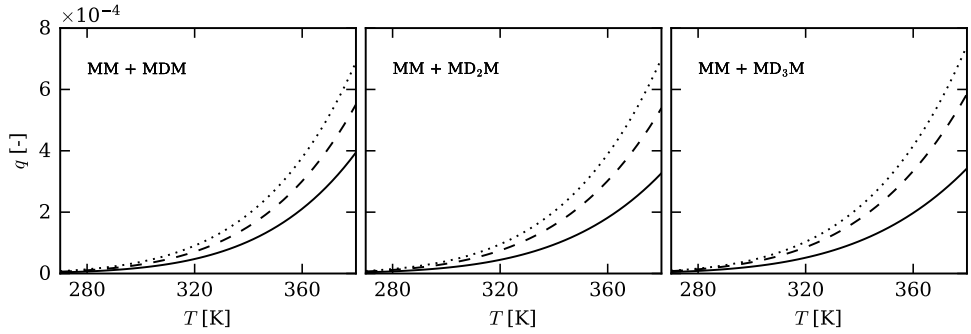

Figure 4.8: Vapor quality plotted against temperature at cell radius r = 11.1 mm and vapor bubble height h = 3.0 mm for three compositions of each mixture of MM with MDM, MD_2M, and MD_3M. The figures show three different compositions for each mixture, mole fractions of MM is shown respectively by the solid line 25 mol% (−), dashed line 50 mol% (−−), and dotted line 75 mol% (···).

uncertainty: (i) temperature, (ii) pressure, (iii) sample composition, (iv) loading correction and (v) measurement repeatability.

(i) *Temperature correction:* The standard platinum resistance thermometer (SPRT) is calibrated regularly. The SPRT was calibrated against the triple points of mercury and water and the freezing point of indium. The standard combined uncertainty in the temperature measurements is determined from the uncertainties in the SPRT, the multimeter to read the SPRT, the calibration, and the possible temperature gradient between the equilibrium cell and the SPRT. The total uncertainty from all sources is estimated to be 0.03 K. A pressure difference is calculated using the thermodynamic model and estimated at the bubble point ($q = 0$) between the experimental measured temperature and 0.03 K from the experimental measured temperature. This pressure difference is taken into account as the temperature uncertainty

$$\begin{aligned} u_T = P_{\text{calc}}\left(T = T_{\text{exp}},\, q = 0,\, \bar{z} = \bar{z}_{\text{bulk}}\right) - \\ P_{\text{calc}}\left(T = T_{\text{exp}} + 0.03\text{ K},\, q = 0,\, \bar{z} = \bar{z}_{\text{bulk}}\right). \end{aligned} \tag{4.11}$$

(ii) *Pressure transducer:* The quartz-crystal pressure transducer (PT) was calibrated with a NIST-traceable piston gauge. The manufacturer stated uncertainty of the PT is 0.01% of the 700 kPa full range. Through regular calibration and temperature control uncertainties of better than those stated by the manufacturer can be achieved. However, a conservative estimate of the pressure uncertainty is used in the overall pressure uncertainty of the bubble-point pressure reported here, namely

$$u_{\text{PT}} = 0.07\text{ kPa}. \tag{4.12}$$

(iii) *Sample composition:* The uncertainty in the sample composition is two-fold. First, there is an uncertainty in the gravimetric preparation of the sample. This is reported as the uncertainty in the mole fraction of the sample components for each sample. There is also an uncertainty in the composition due to entrained air in the mixture, which can have a significant impact on the total uncertainty at low pressures. Because of the low bubble point pressure of the siloxane fluids, the air impurity was found to have a large influence on the uncertainty. To account for the possibility that the degassing of the samples was not complete, a calculation is carried out in order to approximate the air content in the sample, this procedure is described in detail in Section 4.6.1. As there are no data to represent the effect of air in these mixtures, the partial pressure of nitrogen was used to represent the uncertainty due to air impurities and is calculated as follows:

$$\rho_{N_2} = \frac{z_{N_2} \mathrm{n}_{\text{total}}}{V_{\text{vessel}}}, \tag{4.13}$$

$$u_{\text{air}} = P_{N_2}\left(T = T_{\text{exp}},\ \rho = \rho_{N_2}\right), \tag{4.14}$$

where z_{N_2} is the mole fraction of air impurity. The mole fraction is determined following the procedure in Section 4.6.1 for all samples. The maximum air impurity estimated of all samples is taken as the air impurity and set at 0.005 mol% (50 ppm). n_{total} is the total number of moles of the mixture and V_{vessel} is the volume of the sample vessel.

(iv) *Loading correction:* Typically, the equilibrium cell is loaded only one time from a gravimetrically prepared cylinder. In the case in which a second sample is loaded from the same sample vessel, a calculation is performed to account for the uncertainty in sample composition. The composition of the liquid transferred to the cell during the second loading process is calculated by determining the composition of the liquid phase in the sample bottle at ambient temperature (298 K). The difference between the calculated pressure at the reported bulk composition of the mixture and the pressure at the calculated liquid phase composition determined at the experimental temperature is considered to be the uncertainty due to the reloading procedure and given as follows:

$$\bar{x}_{\text{liquid}} = x\left(T = 298\ \text{K},\ \rho_{298\ \text{K}},\ \bar{z} = \bar{z}_{\text{bulk}}\right), \tag{4.15}$$

$$P_{\text{liquid}} = P\left(T = T_{\text{exp}},\ q = 0,\ \bar{z} = \bar{x}_{\text{liquid}}\right), \tag{4.16}$$

$$P_{\text{bulk}} = P\left(T = T_{\text{exp}},\ q = 0,\ \bar{z} = \bar{z}_{\text{bulk}}\right), \tag{4.17}$$

$$u_{\text{loading}} = P_{\text{bulk}} - P_{\text{liquid}}. \tag{4.18}$$

(v) *Repeatability:* The repeatability of the bubble-point measurement is determined as the standard error of the sample mean from the pressures measured

during the 15 minute equilibrium measurement period as described in Section 4.4. The standard error of the mean is the sample standard deviation divided by the square root of the sample size as [20].

$$u_{\text{repeatability}} = \frac{\sigma\left(P_{\text{measured}}\right)}{\sqrt{n}}. \tag{4.19}$$

The overall combined uncertainty for each point is calculated by taking the root sum of squares of the pressure equivalents of the temperature correction, pressure transducer, air impurity, loading correction, and repeatability,

$$u(P) = k\sqrt{u_T^2 + u_{\text{PT}}^2 + u_{\text{air}}^2 + u_{\text{loading}}^2 + u_{\text{repeatability}}^2}. \tag{4.20}$$

The total uncertainty is multiplied by two (coverage factor, $k = 2$) and is reported as the uncertainty in pressure as well as relative uncertainty in percentage for each bubble point measurement. The relative uncertainty is defined as the total uncertainty divided by the measured bubble-point pressure.

4.6 Experimental results and discussion

Bubble-point measurements were made on three compositions of each mixture of MM with MDM, MD_2M, and MD_3M. In all the mixtures, MM was present in approximately 25 mol%, 50 mol% and 75 mol% of the total mixture. The pressure vs. temperature data for each mixture, as well as the relative pressure uncertainty for each are given in Fig. 4.9. The tabulated results can be found in Tables 4.A.1 to 4.A.3. For all of the mixtures, the reported uncertainties are largest for the lowest temperatures (below 320 K). At the lowest temperatures, the pressures are extremely low (below 10 kPa absolute) and, in some cases, below the uncertainty limit of the pressure transducer. Although the uncertainties at low temperatures are high the data are still included here; the data will be weighted differently according to the uncertainty for the fitting of the binary interaction parameters. The only data for binary mixtures of MM + MDM from Abbas [10] is plotted as comparison and good agreement is obtained with the experimental data of this work. A detailed comparison is not possible because of the absence of an uncertainty analysis by Abbas [10].

As seen in Fig. 4.9 the uncertainties are large for low temperatures. The individual relative uncertainties for the mixture of MM 24.5 mol% + MD_3M 75.5 mol% is plotted in Fig. 4.10 as an example to observe the impact of the individual uncertainties on the combined uncertainty of Eq. (4.20). The individual uncertainties do not include the coverage factor ($k = 2$). As can be noticed in Fig. 4.10, the uncertainty of the air impurity has the largest impact, followed by the uncertainty of the pressure transducer. Because of this large effect of the air impurity a detailed discussion is given in the next section.

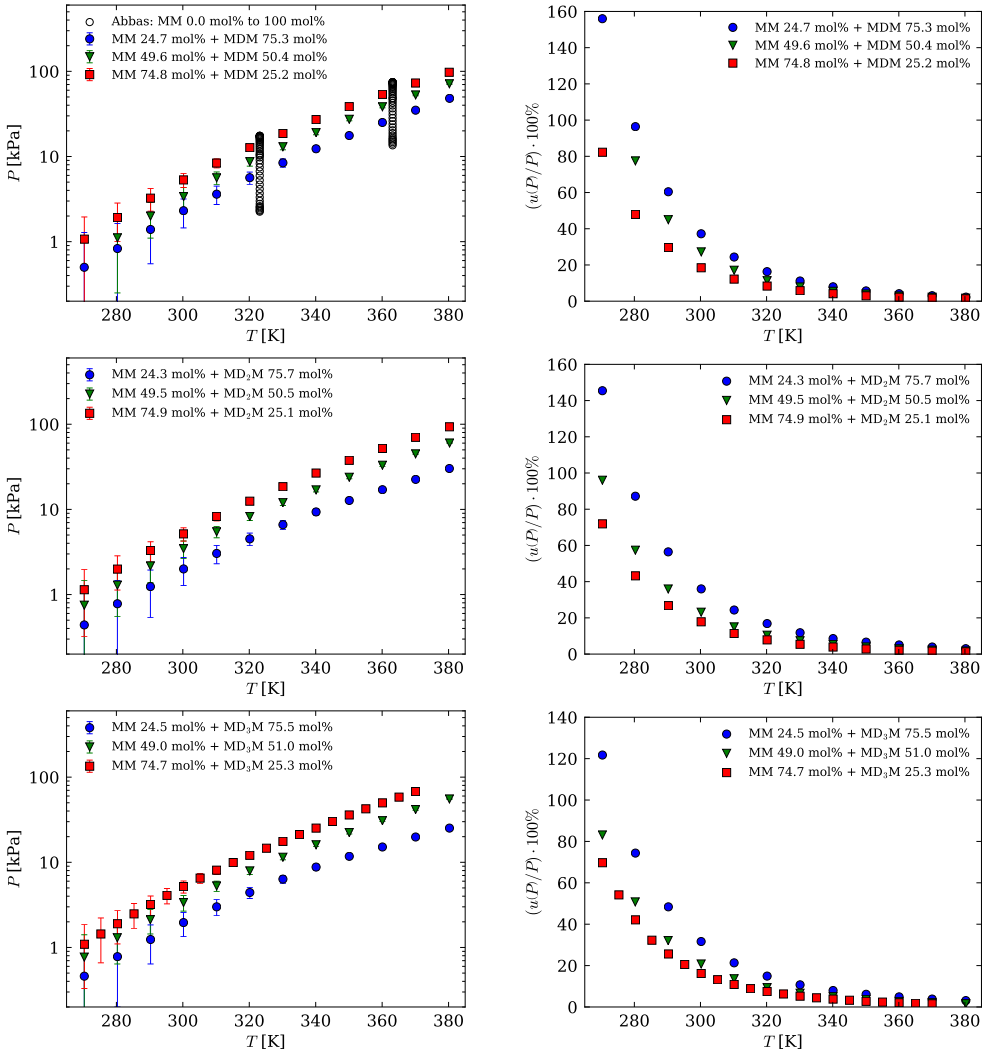

Figure 4.9: Bubble-point data for binary mixtures composed of MM with MDM, MD_2M, and MD_3M. Left) Pressure vs. temperature data for each mixture composition with experimental data (■,▼,●) and literature data from Abbas [10] (○). Right) Relative uncertainty in pressure vs. temperature.

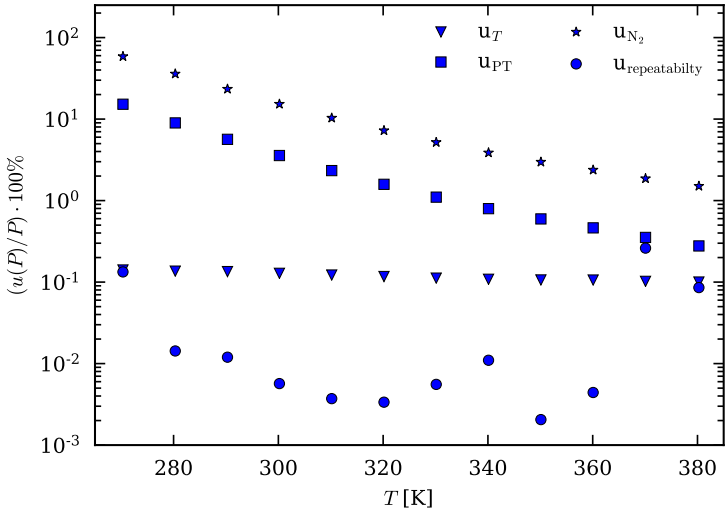

Figure 4.10: Individual relative uncertainties vs. temperature for the binary mixture MM 24.5 mol% + MD_3M 75.5 mol%.

4.6.1 Air impurity

Air impurities and non-condensable gases have a large effect on systems with a low vapor pressure and causing complication for accurate and reliable measurements. To remove air impurities and non-condensable gases the first samples of each mixture of MM with MD_3M were degassed three times, in a similar fashion to the degassing employed by Outcalt et al. [21] and Mansfield et al. [22]. The bubble-point pressures measured of the three times degassed samples show a large deviation from the predicted bubble-point pressure presented in Fig. 4.11 for a binary mixture of MM with MD_3M with approximately 25 mol%, 50 mol%, and 75 mol% of MM. The final set of samples for binary mixtures of MM and MD_3M was degassed for a minimum of fifteen times and additionally a vacuum was applied to the vapor phase in the equilibrium cell to remove impurities (see Section 4.6.2). A large decrease in pressure is obtained between degassing three and fifteen times as shown in Fig. 4.11.

The effect of air on the binary mixtures is qualitatively estimated by fitting the molar composition of nitrogen in a ternary mixture of MM, MD_3M, and N_2 to the measured bubble point pressure at 270 K using the Peng-Robinson equation of state in REFPROP [16] with $k_{ij} = 0$. The molar composition of the ternary mixture is normalized so that the sum of the molar fractions equals one. The normalized molar composition for the ternary mixture of MM, MD_3M, and N_2 is then used to calculate the bubble-point pressures over the range of measured temperatures using the Peng-Robinson equation of state with $k_{ij} = 0$; these results are plotted in Fig. 4.11. The calculated bubble-point pressures show good agreement with the measured bubble-point pressures for the samples of all three compositions. Using Peng-Robinson as an

estimate, the molar composition of nitrogen decreases by a factor of approximately two orders of magnitude between degassing three and fifteen times from the order of 100 ppm to 1 ppm.

Though this is a qualitative estimation of the amount of nitrogen in the sample, it shows the significant impact of N_2 on the bubble-point pressure of the linear siloxanes at low temperatures, which is also confirmed by the high uncertainty shown in Fig. 4.9. Great care should be taken when measuring fluids with low vapor pressure to ensure the air and non-condensable gases are removed from the system.

4.6.2 Degassing vapor phase equilibrium cell

Besides the degassing cycles described in Section 4.4.1, evacuation of the vapor phase in the equilibrium cell is also applied to ensure the removal of non-condensable impurities.

The evacuation of the vapor space is conducted by evacuating the line between valve V-2 and V-3 in Fig. 4.2 through the vacuum pump. When a vacuum is applied to the line, valve V-3 is closed; subsequently V-2 is opened to evacuate the vapor space. After the evacuation valve V-2 is closed and the evacuation cycle is repeated.

The change in composition of the mixture by evacuating the vapor space of the equilibrium cell has been analyzed using the Peng-Robinson equation of state and a ternary mixture of the binary mixture components and nitrogen. First the quality q and void fraction ε of the mixture is determined using the void fraction procedure described in Section 4.5.1. The volume of the liquid and vapor phase is estimated with the equilibrium cell volume V_{cell} and the void fraction

$$V_{\text{l}} = (1-\varepsilon)V_{\text{cell}}, \tag{4.21}$$

$$V_{\text{v}} = \varepsilon V_{\text{cell}}, \tag{4.22}$$

where V_{l} and V_{v} are the volume of the liquid and vapor phase in the equilibrium cell respectively.

Next, the liquid phase mole fraction and liquid phase density are estimated using the composition of the ternary mixture and the quality

$$\bar{x}_{\text{l}} = x(T, \quad q, \quad \bar{z}), \tag{4.23}$$

$$\rho_{\text{v}} = \rho(T, \quad q, \quad \bar{z}), \tag{4.24}$$

where T is the temperature, $\bar{z}$ the molar composition of the the ternary mixture, $\bar{x}_{\text{l}}$ the liquid phase molar composition, and ρ_{l} the molar density of the liquid phase. The total number of moles in the liquid phase is calculated with the liquid phase volume and molar density of the liquid phase

$$n_{\text{l,total}} = \rho_{\text{l}} V_{\text{l}}, \tag{4.25}$$

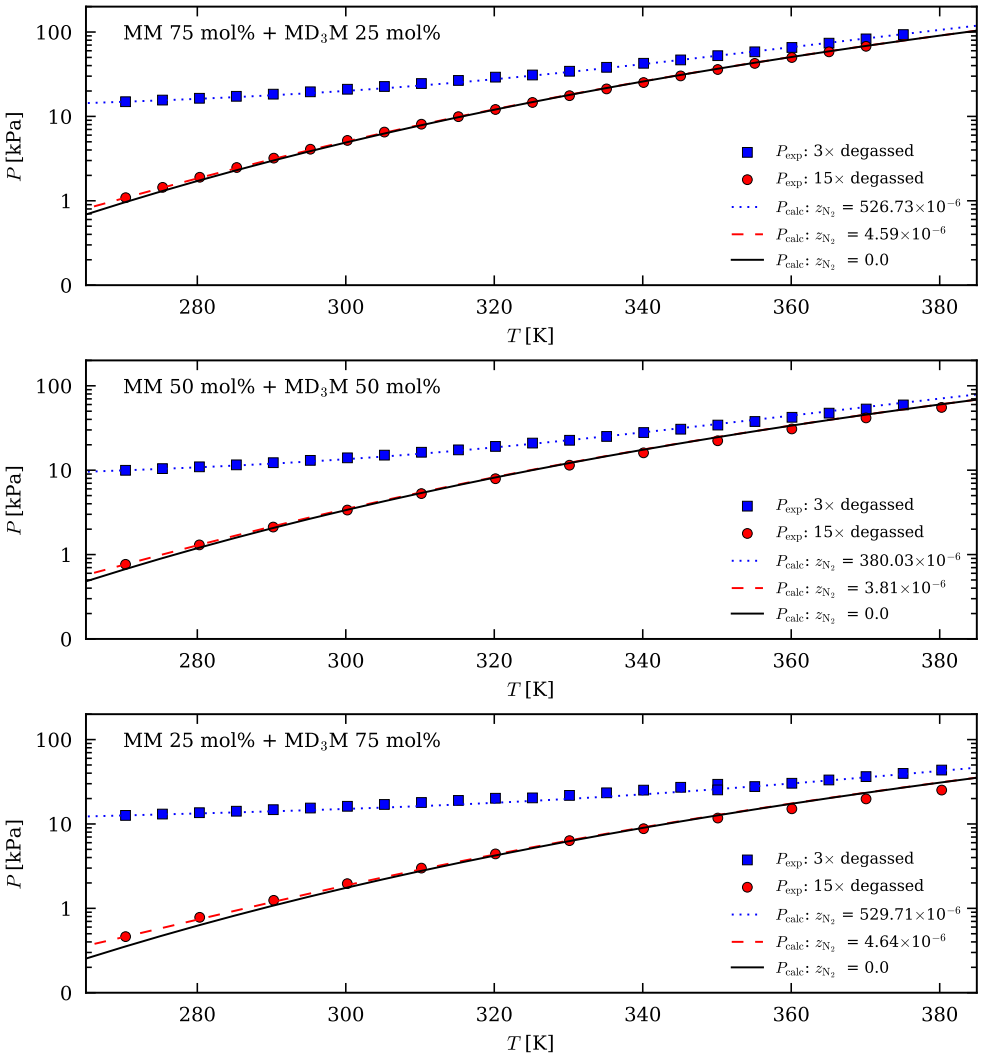

Figure 4.11: Effect of nitrogen on bubble-point pressure for preliminary experimental results of binary mixtures of MM and MD_3M for three compositions and calculated bubble-point pressures with Peng-Robinson equation of state for ternary mixtures of MM, MD_3M, and nitrogen. Three times degassed samples are shown with square blue markers (■), fifteen times degassed sampled and evacuation of the vapor space are shown with round red markers (●). The dotted blue line (···) estimates three times degassed sample, dashed red line (–) estimates fifteen times degassed sample, and full black line (–) estimates binary mixture of siloxanes without impurities.

where $n_{\mathrm{l,total}}$ is the total number of moles in the liquid phase. The number of moles of each component in the liquid phase is calculated using the liquid phase mole fraction and the total number of moles

$$n_{\mathrm{l,i}} = x_{\mathrm{l,i}} n_{\mathrm{l,total}}, \tag{4.26}$$

where $n_{\mathrm{l,i}}$ is the number of moles of component i in the ternary mixture and $x_{\mathrm{l,i}}$ the mole fraction of component i.

Assuming all the molecules in the vapor phase are evacuated from the equilibrium cell, the remaining components are in the liquid phase and the new mixture composition $z_{i,\mathrm{new}}$ is estimated as follows

$$z_{i,\mathrm{new}} = \frac{n_{\mathrm{l,i}}}{n_{\mathrm{l,total}}}. \tag{4.27}$$

By using the new mixture composition $z_{i,\mathrm{new}}$ as the ternary mixture composition $\bar{z}$ the change in composition for the following evacuation cycle can be determined by repeating the procedure described above.

An example of composition and pressure change by evacuating the vapor space is shown in Fig. 4.12 for a mixture of MM 25 mol%, MDM 75 mol%, and a nitrogen impurity taken as 50 ppm. The molar composition is normalized so the sum of the molar fractions equals one and is given as $\bar{z}_{\mathrm{ini}}$. The calculations are performed at a temperature of 270 K, a total of 16 evacuation cycles, and the equilibrium cell volume of V_{cell} = 30 ml. As seen in the figure the change in composition $\Delta z_i = z_{i,\mathrm{new}} - z_{i,\mathrm{ini}}$ is on the order of 10^{-5} for all components in the mixture which is on the same order of magnitude as the composition uncertainty of the mixture. The pressure of the mixture decreases proportional to the change of the nitrogen molar fraction and shows an exponential decay with increasing evacuation cycles.

The estimated decrease of pressure by evacuating the vapor phase in the equilibrium cell is compared with experimental data of the evacuation. The initial composition of nitrogen is estimated by fitting the molar fraction of nitrogen in the ternary mixture to the average pressure and temperature of the cell prior to the first evacuation. Following each evacuation the pressure is calculated and compared to the measured pressure. Fig. 4.13 shows the pressure decrease for the evacuation cycle of two mixtures of MM and MDM and the calculated pressure decrease. It can be observed that the measured pressure also shows an exponential decrease in pressure and qualitative agreement with the calculated pressures.

4.7 Modeling mixture parameters

The thermodynamic properties of the mixture are modeled using the the multiparameter mixture model based on the Helmholtz energy model [23]. Because it is

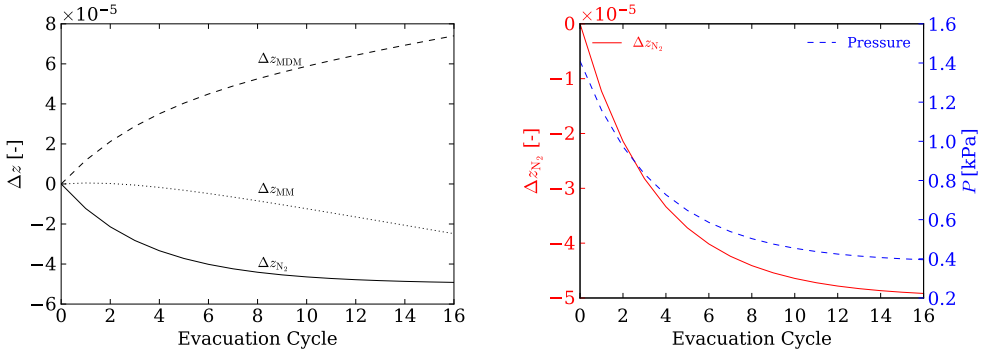

Figure 4.12: Analysis composition change by evacuating vapor space equilibrium cell. Left) Composition change for mixture of MM 25 mol%, MDM 75 mol% and nitrogen vs. evacuation cycles of the vapor phase. Right) Pressure change and nitrogen molar fraction vs. evacuation cycles of the vapor phase.

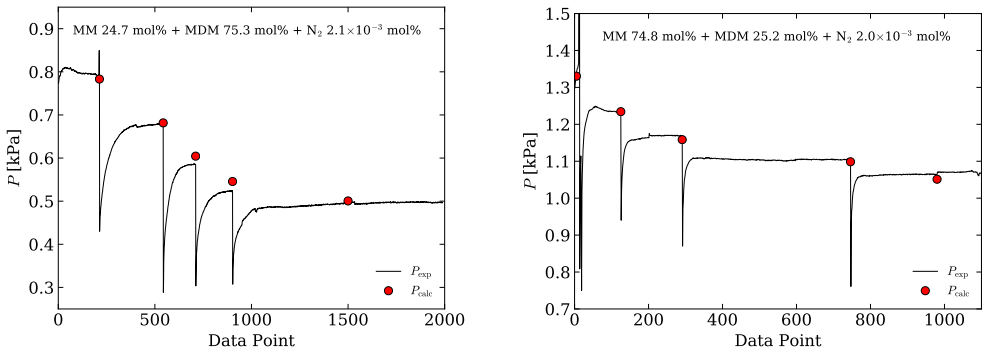

Figure 4.13: Comparison of measured pressure (P_{exp}) decrease by evacuating vapor space of the equilibrium cell (–) and calculated pressure (P_{calc}) of evacuation cycles (●) for mixtures of MM and MDM.

a Helmholtz based model all properties can be obtained from derivatives of the Helmholtz energy [24]. The pressure of the mixture can be obtained from

$$P = \rho RT \left(1 + \delta \frac{\partial \alpha^{\mathrm{r}}}{\partial \delta}(\tau, \delta, \bar{z})\right). \tag{4.28}$$

Other thermodynamic properties like, enthalpy, entropy etc., can be obtained in a similar fashion. The non-dimensional residual Helmholtz energy α^{r} is expressed in terms of the reduced density $\delta = \rho/\rho_{\mathrm{r}}(\bar{z})$ and reciprocal reduced temperature $\tau = T_{\mathrm{r}}(\bar{z})/T$ where $\bar{z}$ is the bulk composition of the mixture. The reducing parameters $\rho_{\mathrm{r}}(\bar{z})$ and $T_{\mathrm{r}}(\bar{z})$ contain the binary interaction parameters described herein and are fitted for the linear siloxane mixtures.

The binary mixture parameters of the multi-fluid Helmholtz energy equation of state are fitted using the bubble-point measurements given in Section 4.6. The critical point properties and molecular weight of the pure fluids under consideration are listed in Table 3.1. The pure fluids state-of-the-art coefficients for the Helmholtz energy equation of state for MM, MDM, and MD_2M are defined by Thol et al. [25] and Thol et al. [26], the state-of-the-art coefficients for MD_3M are derived by König et al. [27].

The reduced mixture parameters τ and δ are calculated from Eq. (2.46) through the composition-dependent reducing function for mixture density and temperature. The reducing parameters for the mixture, T_{r} and $1/\rho_{\mathrm{r}}$ can then be given in common form

$$\mathrm{Y_r}(\bar{z}) = \sum_{i=1}^{C} z_i^2 \mathrm{Y_{c,}}_i + \sum_{i=1}^{C-1} \sum_{j=i+1}^{C} 2 z_i z_j \frac{z_i + z_j}{\beta_{\mathrm{Y},ij}^2 z_i + z_j} \mathrm{Y}_{ij}, \tag{4.29}$$

where Y represents the parameter of interest, with the parameters T_{r} and $1/\rho_{\mathrm{r}}$ defined by the expressions in Table 4.2.

Table 4.2: Reducing parameters for Helmholtz energy equation of state.

$\mathrm{Y_r}$	$\mathrm{Y_{c,}}_i$	$\beta_{\mathrm{Y},ij}$	Y_{ij}
T_{r}	$T_{\mathrm{c},i}$	$\beta_{T,ij}$	$\beta_{T,ij}\gamma_{T,\mathrm{ij}} \left(T_{\mathrm{c},i} T_{\mathrm{c},j}\right)^{0.5}$
$\frac{1}{\rho_{\mathrm{r}}}$	$\frac{1}{\rho_{\mathrm{c},i}}$	$\beta_{v,ij}$	$\beta_{v,ij}\gamma_{v,ij} \frac{1}{8} \left(\frac{1}{\rho_{\mathrm{c},i}^{1/3}} + \frac{1}{\rho_{\mathrm{c},j}^{1/3}}\right)^3$

The binary mixture parameters $\beta_{v,ij}$, $\gamma_{v,ij}$, $\beta_{T,ij}$, and $\gamma_{T,ij}$ are fitted to experimental data for binary mixtures. These mixture reducing models are weighting functions of the critical properties of the pure fluids that form the mixture based on quadratic mixing rules and the combining rules of Lorentz-Berthelot [28]. The reducing parameters obey the following relations:

$$\begin{aligned} &\gamma_{v,ij} = \gamma_{v,ji}, \quad \gamma_{T,ij} = \gamma_{T,ji}, \\ &\beta_{v,ij} = 1/\beta_{v,ji}, \quad \beta_{T,ij} = 1/\beta_{T,ji}. \end{aligned} \tag{4.30}$$

The γ parameters are symmetric, while the β parameters are not symmetric, so the order of fluids in the binary pair must be handled carefully when implementing the binary interaction parameters.

The binary interaction parameters for binary mixtures of MM with MDM, MD_2M, and MD_3M are fitted. The departure function $\Delta\alpha^{\mathbf{r}}(\delta,\tau,\bar{z})$ in Eq. (2.48) is not applied, due to insufficient experimental data to use the departure function. For the fitting of the departure function a relatively large amount of accurate experimental data for thermal and caloric properties is needed (e.g. VLE, homogeneous density, isobaric specific heat, and speed of sound data)[29]. For the fitting, a total of four adjustable binary interaction parameters are considered: $\beta_{v,ij}$, $\gamma_{v,ij}$, $\beta_{T,ij}$, and $\gamma_{T,ij}$. Considering the limited data set available, the parameters fitted here are $\beta_{T,ij}$ and $\gamma_{T,ij}$ because these parameters have the strongest impact on the prediction of the bubble-points and can generally be fit with a relatively small data set. The parameters $\beta_{v,ij}$ and $\gamma_{v,ij}$ are set to unity.

The fitting algorithm developed by Bell et al. [24] together with REFPROP [16] are used for the fitting and optimization of the binary interaction parameters for the multi-fluid Helmholtz energy equation of states. To take into account the uncertainty, which is high at low temperatures as shown in Section 4.6, the algorithm of Bell et al. [24] has been adjusted by weighing the signed error vector using the relative uncertainty. The weighted error vector is calculated as

$$\vec{e}_{\mathrm{S}} = \frac{\vec{P}_{\mathrm{exp}} - \vec{P}_{\mathrm{calc}}}{\vec{P}_{\mathrm{exp}}} \cdot \frac{1}{\vec{u}_{\mathrm{rel}}(P)} \times 100\% = \frac{\vec{P}_{\mathrm{exp}} - \vec{P}_{\mathrm{calc}}}{\vec{u}_{\mathrm{exp}}(P)} \times 100\%, \tag{4.31}$$

where $\vec{P}_{\mathrm{exp}}$ is the measured bubble-point pressure, $\vec{P}_{\mathrm{calc}}$ is the calculated bubble-point pressure as a function of the given bubble-point temperature and bulk mole fraction, and $\vec{u}_{\mathrm{rel}} = \vec{u}_{\mathrm{exp}}(P)/\vec{P}_{\mathrm{exp}}$ is the uncertainty of the measured bubble-point pressure. The weighted signed error vector affects the objective function, which is being minimized to find the optimal binary interaction coefficients through the root-sum of squares error metric. By weighing the error vector with the relative uncertainty, points with high uncertainty contribute less to the overall error.

The totality of the available bubble-point data measured in this work is used to fit the binary interaction parameters with the updated optimization approach using the fitting algorithm of Bell et al. [24] and weighing the signed error vector using the relative uncertainty as shown in Eq. (4.31). The fitted binary interaction parameters for the three binary mixtures are listed in Table 4.3.

The binary interaction parameters are implemented to determine deviations of the measured bubble-point pressure from the equation of state. The results for the binary mixture of MM with MDM, MD_2M, and MD_3M are presented in Fig. 4.14, where the left figure shows the deviations with estimated parameters by REFPROP (the paramters are estimated because no binary interaction parameters are available for these mixtures) and the right figure the deviation with the newly fitted binary interaction parameters from Table 4.3.

Table 4.3: Binary interaction parameters for multi-fluid Helmholtz energy equation of state.

Mixture	$\beta_{T,ij}$	$\gamma_{T,ij}$	$\beta_{v,ij}$	$\gamma_{v,ij}$
MM + MDM	1.001960	1.007571	1.0	1.0
MM + MD_2M	1.003621	1.023157	1.0	1.0
MM + MD_3M	0.999076	1.040436	1.0	1.0

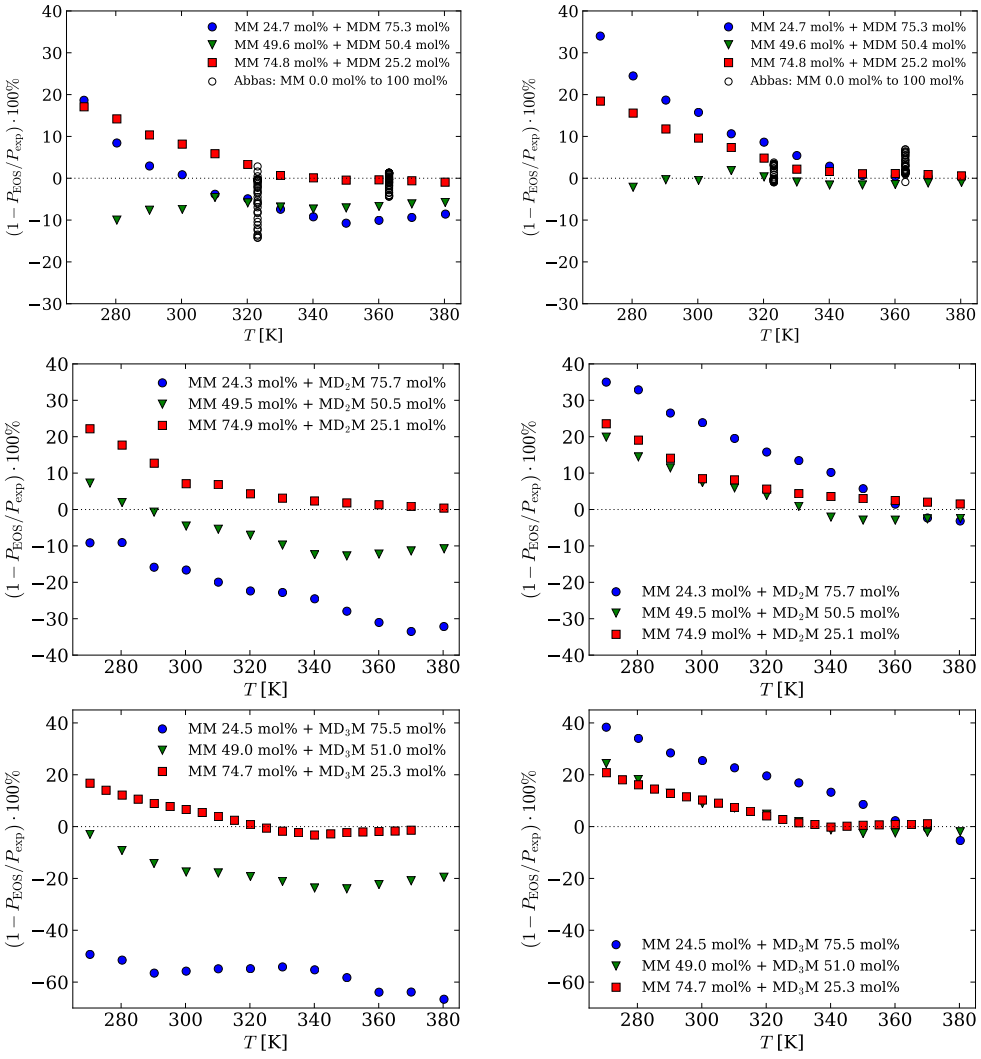

Figure 4.14: Deviation between experimental and calculated values as a function of temperature of MM with MDM, MD_2M, and MD_3M for the Helmholtz energy equation of state. Left) Estimated binary interaction parameters by REFPROP. Right) Fitted binary interaction parameters listed in Table 4.3.

Deviations from the estimated parameters by REFPROP range from as high as +20% for the low temperatures to -10% for the high temperatures for mixtures of MM and MDM. With the new binary interaction parameters the deviations increased for the low temperatures up to 35%, for high temperatures (above 320 K) the deviations drop to less than 10% for all compositions. The deviation increase at low temperatures is due to the weighing based on the uncertainty introduced in the fitting algorithm, though because of the weighing the deviation at higher temperatures is reduced.

The deviation of MM and MD_2M with the estimated parameters from REFPROP range from +25% to -30% shown in the center left figure of Fig. 4.14. The new binary interaction parameters presented in the center right figure of Fig. 4.14 causes again an increase in deviation for low temperatures, but the high temperatures (above 320 K) dropped to less than 10% for all compositions.

For MM and MD_3M the deviation with the estimated parameters are as high as -60% for the mixture with 24.5 mol% MM, the other mixtures deviations range from -20% to +20%. The new binary interaction parameters reduce the deviations for the mixture with 49.0 mol% and 74.9 mol% MM below 10% for temperatures above 320 K. The deviation of the mixture with 24.5 mol% still has a deviation above 20% at 320 K and drops below 10% at 360 K.

4.7.1 Assessment of physical and extrapolation behavior

The correct physical and extrapolation behavior of the equation of state in regions where no data are available is an essential aspect in the development. This correct behavior is important for pure fluids equation of state as well as multicomponent equations of state. This is because many application require thermodynamic properties outside of the range of validity and thermodynamic properties not investigated experimentally. The diagrams used for the evaluation of the correct physical and extrapolation behavior for the binary mixtures with the fitted binary interaction parameters from Table 4.3 are shown in Fig. 4.15 for the binary mixture MM–MDM, Figs. 4.B.1 and 4.B.2 in the appendix present the results for MM with MD_2M and MD_3M. All binary mixtures are plotted for a MM molar concentration of 50 mol%. Important for correct physical and extrapolation behavior is that no bumps are present and smooth behavior is observed in the isolines, vapor-liquid equilibrium curve, and the characteristic ideal curves.

The top left figures show the vapor-liquid equilibrium curve and isobars in the for temperature as a function of specific volume. The selected isobars are plotted from P_{min} = 0.5 MPa P_{max} = 6 MPa. The vapor-liquid equilibrium curve and isobars are smooth lines up to 800 K, which indicates good physical behavior. The top right figures show the pressure as a function of specific volume and presents the vapor-liquid equilibrium curve and selected isotherms up to T_{max} = 1500 K. Again, no bumps are visible in the isotherms and the vapor-liquid equilibrium curve for all binary mixtures

of Figs. 4.B.1, 4.B.2 and 4.15. The bottom left figures present the speed of sound as a function of temperature, including the vapor-liquid equilibrium curve and isobars from $P_{\text{min}} = 0.5$ MPa $P_{\text{max}} = 6$ MPa. The speed of sound of the bubble and dew curve need to have a negative slope and curvature in the vicinity of the critical point, which is the case for all three binary mixtures. The bubble and dew curve merge into a minimum at the critical point, which is also an indication of good physical behavior of the fitted binary interaction parameters and equation of state for the binary mixtures. Further, the isobars show smooth behavior and the extrapolated liquid phase exhibits a negative slope, also indicating good physical and extrapolation behavior. Finally, the characteristic ideal curves are plotted in the bottom right figures. The characteristic ideal curves demonstrate the extrapolation behavior of the equation of state. The characteristic ideal curves are the Ideal curve, Boyle curve, Joule-Thomson curve, and Joule-inversion curve, for more details and definition see Span [23], Lemmon et al. [30], and Span et al. [31]. The characteristic ideal curves have to be smooth without any bumps. All characteristic from Figs. 4.B.1, 4.B.2 and 4.15 for the binary mixtures show decent behavior. This indicates good extrapolation behavior of the multicomponent Helmholtz energy model with the fitted binary interaction parameters from Table 4.3.

4.7.2 Assessment of speed of sound and fundamental derivative of gas dynamics

The behavior of the critical speed of sound, critical compressibility factor and fundamental derivate of gas dynamics are assessed using the fitted binary interaction parameters from Table 4.3 for binary mixture of MM with MDM, MD_2M, and MD_3M. The reduced critical speed of sound and the critical compressibility factor are presented in Fig. 4.16. The fitted binary interaction parameters are indicated by the solid lines and the estimated parameters by REFPROP with the dotted line. Fig. 4.16 shows that the reduced speed of sound and compressibility factor at the critical point increase with a larger concentration of MM and decrease for a lower concentration of MM for all binary mixtures. The effect of the new binary interaction parameters also increases with increasing molecular complexity difference between the pure components. This can also be seen in Table 4.3, where $\gamma_{T,ij}$ differs more from unity with increasing molecular complexity between the pure components in the mixture. The non-monotonic behavior is still present as in the original thermodynamic models and slightly increased and shifted towards the less complex component in the mixture for the new binary interaction parameters.

Fig. 4.17 presents the minimum value of the fundamental derivative of gas dynamics Γ_{min} along the dew curve. Here the same behavior is observed using the fitted binary interaction parameters as for the critical speed of sound and critical compressibility factor. Fig. 4.17 shows that the value of Γ_{min} increases with a larger concentration of MM and decreases with a lower concentration of MM for all binary

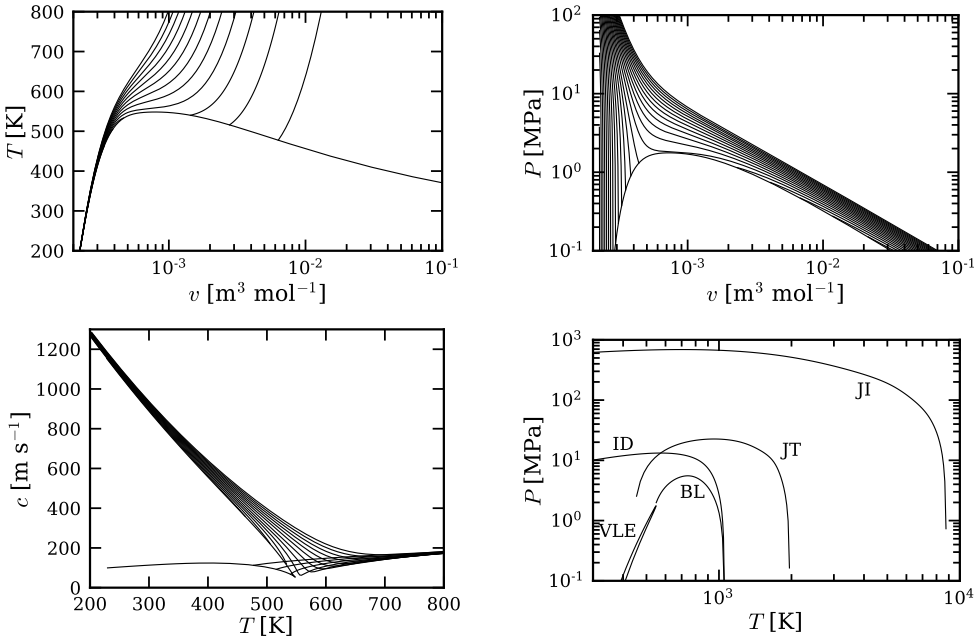

Figure 4.15: Physical and extrapolation behavior of binary mixture MM–MDM with molar concentration MM of 50 mol%. Generated with the Helmholtz energy equation of state and fitted binary interaction parameters from Table 4.3. Top left) Temperature as a function of specific volume with selected isobars. Top right) Pressure as a function of specific volume with selected isotherms. Bottom left) Speed of sound as a function of temperature with selected isobars. Bottom right) Characteristic ideal curves JI: Joule-inversion, JT: Joule-Thomson, BL: Boyle, ID: Ideal, VLE: Vapor-liquid equilibrium.

mixtures. This is the same effect as is observed for the critical speed of sound and critical compressibility factor in Fig. 4.16. The non-monotonic behavior of the value of Γ_{min} also increases with the fitted binary interaction parameters.

The fundamental derivative along the dew curve is shown in Fig. 4.18 for each mixture of MM with MDM, MD_2M, and MD_3M, with MM concentration of 25 mol%, 50 mol%, and 75 mol%. Here it is also shown that for 25 mol% MM the value of Γ_{min} decreases and increases for 75 mol% MM, small difference in the value of Γ_{min} is observed for 50 mol% MM for all mixtures. The temperature for which the value of Γ_{min} is reached is also shifted to higher temperature. The increase in temperature is the largest for MM and MD_4M with 75 mol% MM, this increase in temperature is approximately 10 K. The lowest increase in temperature is observed for MM and MDM with 25 mol% with an approximate increase in temperature of 2 K. This again shows the fitted binary interaction coefficients have the largest impact on the binary mixture with the largest molecular complexity difference between the

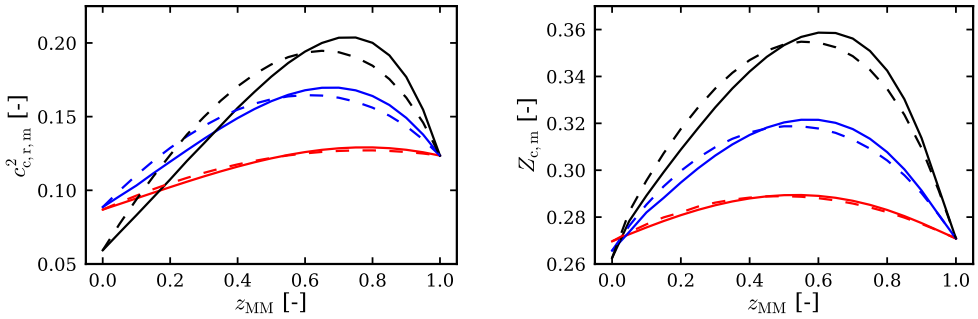

Figure 4.16: Assessment of estimated and fitted binary interaction parameters for the reduced speed of sound and compressibility factor at critical point. Binary mixtures MM with MDM (–), MD_2M (–), and MD_3M (–) are evaluated at composition varying from z_{MM} = 0...1. The dashed lines present the estimated binary interaction parameters by REFPROP and the solid lines present the fitted binary interaction parameters from Table 4.3 for the Helmholtz energy equation of state [16].

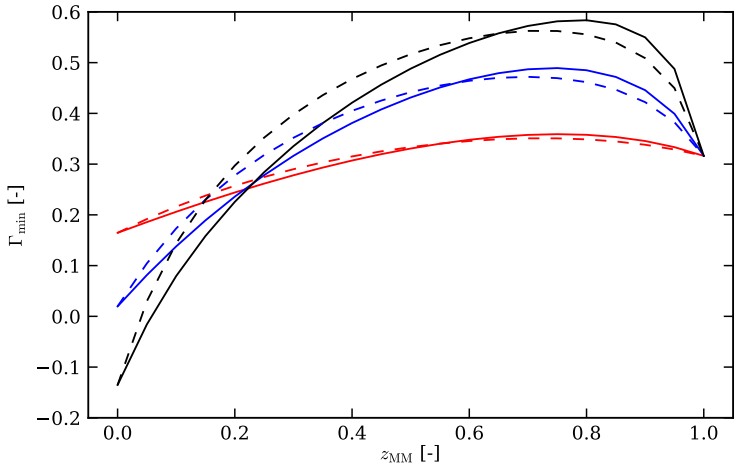

Figure 4.17: Assessment of estimated and fitted binary interaction parameters for the minimum value of the fundamental derivative of gas dynamics Γ_{min}. Binary mixtures MM with MDM (–), MD_2M (–), and MD_3M (–) are evaluated at composition varying from z_{MM} = 0...1. The dashed lines present the estimated binary interaction parameters by REFPROP and the solid lines present the fitted binary interaction parameters from Table 4.3 for the Helmholtz energy equation of state [16].

pure components and the lowest concentration of MM.

4.8 Conclusion

Bubble-point pressures were measured for three binary mixtures of MM with MDM, MD_2M, and MD_3M. For each mixture three compositions were measured with a MM presence in all mixtures of approximately 25 mol%, 50 mol%, and 75 mol% of the total mixture. The bubble-point pressures were measured at temperatures from 270 K to 380 K and the pressure ranged from 0.46 kPa to 97.45 kPa for all samples. Large uncertainties are observed for the lowest temperatures (below 320 K) for all binary mixture pairs, as data at these temperatures have very low bubble-point pressures. Though the pressure is below the uncertainty limit of the pressure transducer, the large uncertainty is mostly due to the effect of non-condensable gases in the mixture.

The effect of non-condensable gases was analyzed to determine the impact on the measurements. The analysis was carried out by comparing the bubble-point pressure measurement of a samples degassed for three freezing/evacuating/heating/thawing cycles and samples degassed for fifteen cycles and evacuation of the vapor phase in the equilibrium cell. By estimating the effect of non-condensable gases by fitting a ternary mixture with nitrogen employing the Peng-Robinson equation of state a decrease by a factor of approximately 100 between degassing three and fifteen times is observed from the order 100 ppm to 1 ppm. Though this is a qualitative estimation of the amount of non-condensable gases in the sample, it shows the significant impact of nitrogen on the bubble-point pressure of the linear siloxanes at low temperatures, which is also confirmed by the high uncertainty due to air impurities. This also shows the large impact of small amounts of non-condensable gas impurities on fluids with low bubble-point pressure which can affect the thermodynamic properties of the fluid and consequently influence the predicted efficiency and performance of ORCs as well as other processes.

For each binary mixture new binary interaction parameters were fitted for the multi-fluid Helmholtz energy model using the obtained bubble-point pressure data. The fitting was done by weighing the bubble-point pressure data point by the relative uncertainty, which ensures that data points with high uncertainty contribute less to the overall fitting of the binary interaction parameter. At higher temperatures (above 320 K) the new binary interaction parameters represent the experimental bubble-point pressures to within 10% deviation, where previous deviations using estimated binary interaction parameters where of the order of 20%. With exception for binary mixture pair MM–MD_3M with approximately 25 mol% of MM, here deviations up to 20% are observed for temperatures above 320 K. For temperatures below 320 K, the deviations overall increases, which is due to the weighing based on the relative uncertainty introduced in the fitting algorithm. Furthermore, good physical and extrapolation behavior of the binary mixtures with fitted binary interaction parameters is observed.

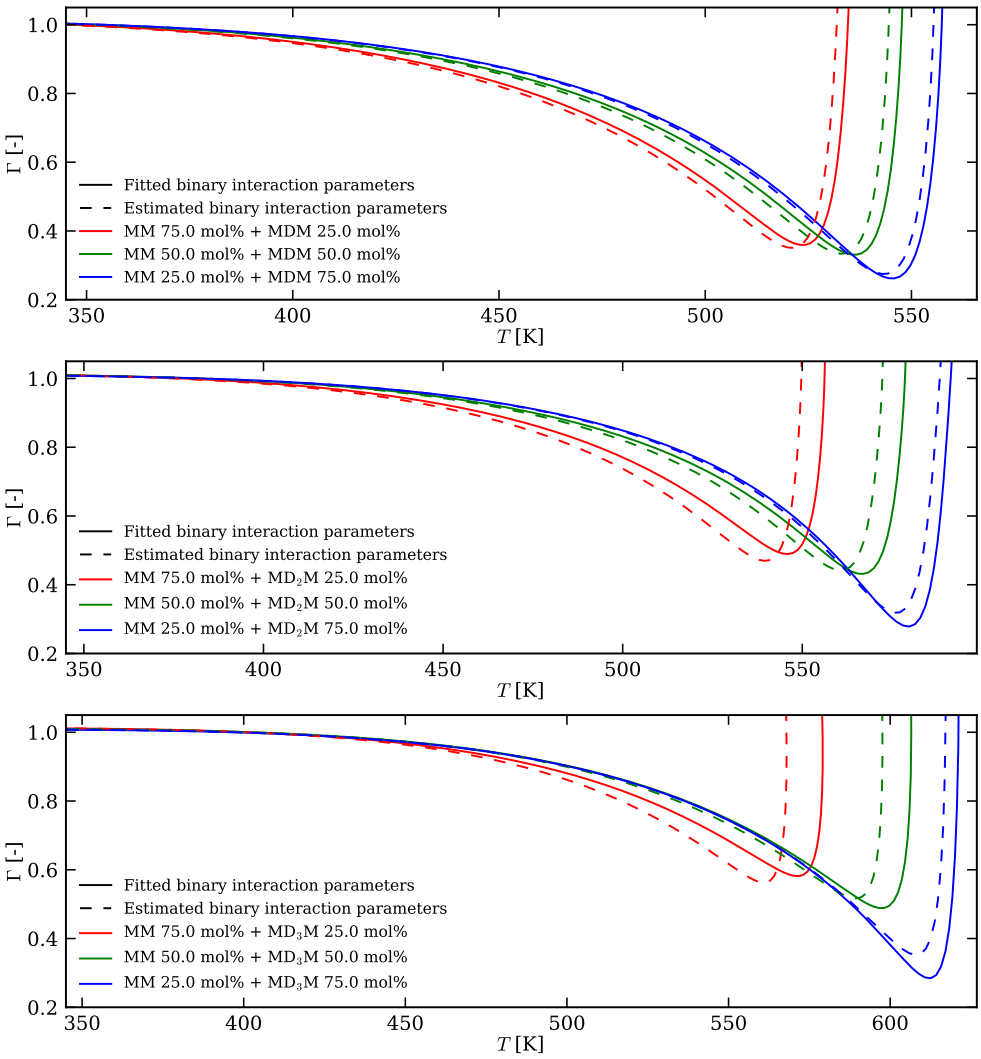

Figure 4.18: Assessment of estimated and fitted binary interaction parameters for the minimum value of the fundamental derivative of gas dynamics as a function of temperature evaluated along the dew curve. Binary mixtures of MM with MDM (top), MD_2M (center), and MD_3M (bottom). The dashed lines present the estimated binary interaction parameters by REFPROP and the solid lines present the fitted binary interaction parameters from Table 4.3 for the Helmholtz energy equation of state [16].

Finally, the affect of the fitted binary interaction parameters on the speed of sound and fundamental derivative of gas dynamics is assessed. The fitted binary interaction parameters increase the non-monotonic behavior of the critical speed of sound, critical compressibility, and the minimum value of Γ for all binary mixtures. The thermodynamic properties are also slightly shifted to the less molecular complex component in the mixture. The value of Γ_{min} also decreased for the binary mixture with higher concentrations of MDM, MD_2M, and MD_3M which increases the region for which the mixtures can exhibit non-ideal fluid dynamic effects. On the other side, for the binary mixtures with higher concentrations of MM the value of Γ_{min} increased. For all binary mixtures the temperature for Γ_{min} increased with the fitted binary interaction parameters.

Appendix

4.A Tables of bubble-point measurements

Table 4.A.1: Bubble-point pressure measurement MM–MDM 25-50-75 mol%.

z_1	$u(z_1) \times 10^{-5}$	T	P	$u(P)$	$\left(\frac{u(P)}{P}\right) \times 100\%$	$\left(1 - \frac{P_{\text{EOS}}}{P_{\text{exp}}}\right) \times 100\%$
-	-	K	kPa	kPa	%	%
0.247	3.351	270.32	0.50	0.78	156.00	23.57
0.247	3.351	280.32	0.83	0.80	96.39	14.26
0.247	3.351	290.27	1.39	0.84	60.43	9.28
0.247	3.351	300.21	2.31	0.86	37.23	7.39
0.247	3.351	310.19	3.61	0.88	24.38	3.02
0.247	3.351	320.15	5.64	0.92	16.31	1.94
0.247	3.351	330.13	8.43	0.94	11.15	-0.51
0.247	3.351	340.11	12.33	0.98	7.95	-2.35
0.247	3.351	350.09	17.62	1.00	5.68	-3.97
0.247	3.351	360.08	25.09	1.04	4.15	-3.54
0.247	3.351	370.07	34.97	1.06	3.03	-3.13
0.247	3.351	380.31	48.18	1.08	2.24	-2.65
0.496	1.416	280.32	1.11	0.86	77.48	-10.49
0.496	1.416	290.27	2.00	0.90	45.00	-6.90
0.496	1.416	300.24	3.38	0.92	27.22	-5.74
0.496	1.416	310.19	5.62	0.96	17.08	-2.26
0.496	1.416	320.16	8.68	0.98	11.29	-2.97
0.496	1.416	330.13	13.01	1.02	7.84	-3.56
0.496	1.416	340.11	19.04	1.04	5.46	-3.76
0.496	1.416	350.10	27.34	1.08	3.95	-3.34
0.496	1.416	360.09	38.36	1.10	2.87	-2.94
0.496	1.416	370.09	52.82	1.14	2.16	-2.36
0.496	1.416	380.24	71.45	1.18	1.65	-2.11
0.748	1.048	270.34	1.07	0.88	82.24	10.75
0.748	1.048	280.32	1.92	0.92	47.92	9.43
0.748	1.048	290.30	3.24	0.96	29.63	6.88
0.748	1.048	300.22	5.31	0.98	18.46	5.81
0.748	1.048	310.18	8.37	1.02	12.19	4.46
0.748	1.048	320.16	12.70	1.06	8.35	2.67
0.748	1.048	330.13	18.63	1.08	5.80	0.62
0.748	1.048	340.11	27.13	1.12	4.13	0.55
0.748	1.048	350.10	38.48	1.14	2.96	0.35
0.748	1.048	360.09	53.62	1.18	2.20	0.65
0.748	1.048	370.08	72.91	1.22	1.67	0.56
0.748	1.048	380.20	97.45	1.26	1.29	0.28

Table 4.A.2: Bubble-point pressure measurement MM + MD_2M 25-50-75 mol%.

z_1	$u(z_1) \times 10^{-5}$	T	P	$u(P)$	$\left(\frac{u(P)}{P}\right) \times 100\%$	$\left(1 - \frac{P_{EOS}}{P_{exp}}\right) \times 100\%$
-	-	K	kPa	kPa	%	%
0.243	1.613	270.33	0.44	0.64	145.45	24.23
0.243	1.613	280.30	0.78	0.68	87.18	22.67
0.243	1.613	290.24	1.24	0.70	56.45	16.13
0.243	1.613	300.23	2.00	0.72	36.00	13.79
0.243	1.613	310.19	3.04	0.74	24.34	9.50
0.243	1.613	320.16	4.51	0.76	16.85	5.82
0.243	1.613	330.13	6.61	0.78	11.80	3.65
0.243	1.613	340.11	9.34	0.80	8.57	0.46
0.243	1.613	350.11	12.73	0.84	6.60	-4.11
0.243	1.613	360.09	17.04	0.86	5.05	-8.43
0.243	1.613	370.09	22.51	0.88	3.91	-12.25
0.243	1.613	380.24	30.20	0.90	2.98	-12.82
0.495	2.203	270.33	0.75	0.72	96.00	13.38
0.495	2.203	280.31	1.29	0.74	57.36	8.90
0.495	2.203	290.24	2.17	0.78	35.94	6.78
0.495	2.203	300.21	3.46	0.80	23.12	3.41
0.495	2.203	310.18	5.46	0.82	15.02	2.60
0.495	2.203	320.16	8.26	0.86	10.41	0.99
0.495	2.203	330.13	11.99	0.88	7.34	-1.71
0.495	2.203	340.11	16.94	0.90	5.31	-4.46
0.495	2.203	350.10	23.83	0.94	3.94	-5.12
0.495	2.203	360.08	32.99	0.96	2.91	-5.05
0.495	2.203	370.07	44.89	0.98	2.18	-4.66
0.495	2.203	380.31	60.19	1.02	1.69	-4.57
0.749	0.811	270.33	1.14	0.82	71.93	16.89
0.749	0.811	280.31	1.99	0.86	43.22	13.66
0.749	0.811	290.29	3.29	0.88	26.75	9.76
0.749	0.811	300.21	5.16	0.92	17.83	5.03
0.749	0.811	310.18	8.27	0.94	11.37	5.63
0.749	0.811	320.16	12.48	0.98	7.85	3.76
0.749	0.811	330.13	18.48	1.00	5.41	3.06
0.749	0.811	340.11	26.71	1.04	3.89	2.66
0.749	0.811	350.10	37.70	1.06	2.81	2.37
0.749	0.811	360.08	51.97	1.10	2.12	2.02
0.749	0.811	370.08	70.19	1.14	1.62	1.65
0.749	0.811	380.24	93.35	1.16	1.24	1.16

Table 4.A.3: Bubble-point pressure measurement MM + MD_3M 25-50-75 mol%.

z_1	$u(z_1) \times 10^{-5}$	T	P	$u(P)$	$\left(\frac{u(P)}{P}\right) \times 100\%$	$\left(1 - \frac{P_{EOS}}{P_{exp}}\right) \times 100\%$
-	-	K	kPa	kPa	%	%
0.245	1.513	270.34	0.46	0.56	121.74	23.02
0.245	1.513	280.32	0.78	0.58	74.36	18.75
0.245	1.513	290.29	1.24	0.60	48.39	12.81
0.245	1.513	300.20	1.96	0.62	31.63	10.01

Table 4.A.3: Bubble-point pressure measurement MM + MD_3M 25-50-75 mol%.

z_1	$u(z_1) \times 10^{-5}$	T	P	$u(P)$	$\left(\frac{u(P)}{P}\right) \times 100\%$	$\left(1 - \frac{P_{EOS}}{P_{exp}}\right) \times 100\%$
-	-	K	kPa	kPa	%	%
0.245	1.513	310.18	3.00	0.64	21.33	7.30
0.245	1.513	320.16	4.42	0.66	14.93	4.11
0.245	1.513	330.13	6.35	0.68	10.71	1.35
0.245	1.513	340.11	8.79	0.70	7.96	-2.56
0.245	1.513	350.11	11.75	0.72	6.13	-7.78
0.245	1.513	360.09	15.13	0.74	4.89	-14.90
0.245	1.513	370.08	19.82	0.76	3.83	-18.09
0.245	1.513	380.27	25.21	0.78	3.09	-23.38
0.490	3.539	270.33	0.77	0.64	83.12	12.60
0.490	3.539	280.27	1.30	0.66	50.77	7.13
0.490	3.539	290.22	2.12	0.68	32.08	2.53
0.490	3.539	300.21	3.37	0.70	20.77	-0.76
0.490	3.539	310.18	5.28	0.72	13.64	-1.67
0.490	3.539	320.16	7.92	0.74	9.34	-3.56
0.490	3.539	330.13	11.46	0.76	6.63	-6.00
0.490	3.539	340.11	16.05	0.80	4.98	-9.07
0.490	3.539	350.10	22.32	0.82	3.67	-10.26
0.490	3.539	360.08	30.81	0.84	2.73	-9.75
0.490	3.539	370.08	41.64	0.86	2.07	-9.32
0.490	3.539	380.26	55.42	0.88	1.59	-9.05
0.747	1.219	270.35	1.09	0.76	69.72	11.30
0.747	1.219	275.33	1.44	0.78	54.17	9.23
0.747	1.219	280.33	1.90	0.80	42.11	8.00
0.747	1.219	285.31	2.48	0.80	32.26	7.02
0.747	1.219	290.30	3.20	0.82	25.62	5.92
0.747	1.219	295.23	4.09	0.84	20.54	5.23
0.747	1.219	300.22	5.19	0.84	16.18	4.53
0.747	1.219	305.20	6.52	0.86	13.19	3.80
0.747	1.219	310.19	8.08	0.88	10.89	2.60
0.747	1.219	315.17	9.93	0.88	8.86	1.44
0.747	1.219	320.16	12.08	0.90	7.45	0.04
0.747	1.219	325.15	14.63	0.92	6.29	-1.07
0.747	1.219	330.14	17.61	0.92	5.22	-2.05
0.747	1.219	335.12	21.18	0.94	4.44	-2.41
0.747	1.219	340.11	25.20	0.96	3.81	-3.21
0.747	1.219	345.10	30.19	0.98	3.25	-2.64
0.747	1.219	350.10	35.96	0.98	2.73	-2.10
0.747	1.219	355.09	42.48	1.00	2.35	-1.78
0.747	1.219	360.09	49.89	1.02	2.04	-1.52
0.747	1.219	365.09	58.24	1.02	1.75	-1.37
0.747	1.219	370.08	67.74	1.04	1.54	-1.05

4.B Assessment of physical and extrapolation behavior

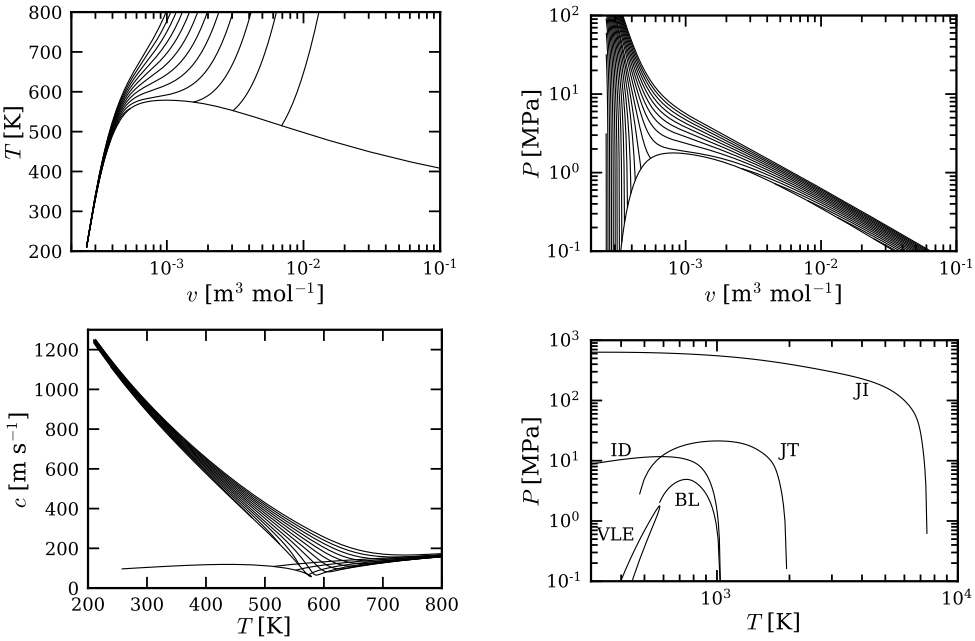

Figure 4.B.1: Physical and extrapolation behavior of binary mixture MM–MD_2M with molar concentration MM of 50 mol%. Generated with the Helmholtz energy equation of state and fitted binary interaction parameters from Table 4.3. Top left) Temperature as a function of specific volume with selected isobars. Top right) Pressure as a function of specific volume with selected isotherms Bottom left) Speed of sound as a function of temperature with selected isobars. Bottom right) Characteristic ideal curves JI: Joule-inversion, JT: Joule-Thomson, BL: Boyle, ID: Ideal, VLE: Vapor-liquid equilibrium.

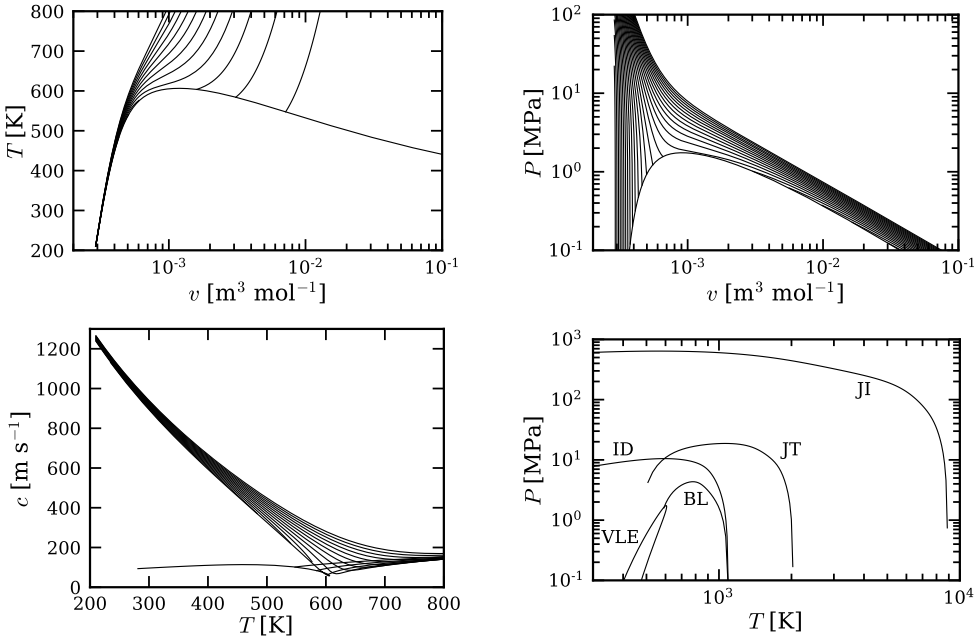

Figure 4.B.2: Physical and extrapolation behavior of binary mixture MM–MD_3M with molar concentration MM of 50 mol%. Generated with the Helmholtz energy equation of state and fitted binary interaction parameters from Table 4.3. Top left) Temperature as a function of specific volume with selected isobars. Top right) Pressure as a function of specific volume with selected isotherms. Bottom left) Speed of sound as a function of temperature with selected isobars. Bottom right) Characteristic ideal curves JI: Joule-inversion, JT: Joule-Thomson, BL: Boyle, ID: Ideal, VLE: Vapor-liquid equilibrium.

References

[1] R. D. Chirico, M. Frenkel, J. W. Magee, V. Diky, C. D. Muzny, A. F. Kazakov, K. Kroenlein, I. Abdulagatov, G. R. Hardin, W. E. Acree, J. F. Brenneke, P. L. Brown, P. T. Cummings, T. W. de Loos, D. G. Friend, A. R. H. Goodwin, L. D. Hansen, W. M. Haynes, N. Koga, A. Mandelis, K. N. Marsh, P. M. Mathias, C. McCabe, J. P. O'Connell, A. Pádua, V. Rives, C. Schick, J. P. M. Trusler, S. Vyazovkin, R. D. Weir, and J. Wu. "Improvement of Quality in Publication of Experimental Thermophysical Property Data: Challenges, Assessment Tools, Global Implementation, and Online Support". In: *Journal of Chemical & Engineering Data* 58.10 (2013), pp. 2699–2716. DOI: 10.1021/je400569s.

[2] J. M. Fonseca, R. Dohrn, and S. Peper. "High-pressure fluid-phase equilibria: Experimental methods and systems investigated (2005–2008)". In: *Fluid Phase Equilib.* 300.1 (2011), pp. 1–69. ISSN: 0378-3812. DOI: 10.1016/j.fluid.2010.09.017.

[3] C. Narasigadu, P. Naidoo, C. Coquelet, D. Richon, and D. Ramjugernath. "A novel static analytical apparatus for phase equilibrium measurements". In: *Fluid Phase Equilib.* 338 (2013), pp. 188–196. ISSN: 0378-3812. DOI: 10.1016/j.fluid.2012.11.008.

[4] H. Preston-Thomas. "The International Temperature Scale of 1990 (ITS - 90)". In: *Metrologia* 27.1 (1990), p. 3. URL: http://stacks.iop.org/0026-1394/27/i=1/a=002.

[5] P. Colonna, E. Casati, C. Trapp, T. Mathijssen, J. Larjola, T. Turunen-Saaresti, and A. Uusitalo. "Organic Rankine Cycle Power Systems: From the Concept to Current Technology, Applications, and an Outlook to the Future". In: *J. Eng. Gas Turbines Power* 137.10 (2015). DOI: 10.1115/1.4029884.

[6] M. Wang, J. Wang, Y. Zhao, P. Zhao, and Y. Dai. "Thermodynamic analysis and optimization of a solar-driven regenerative organic Rankine cycle (ORC) based on flat-plate solar collectors". In: *Appl. Therm. Eng.* 50.1 (2013), pp. 816–825. DOI: 10.1016/j.applthermaleng.2012.08.013.

[7] D. Meinel, C. Wieland, and H. Spliethoff. "Effect and comparison of different working fluids on a two-stage organic rankine cycle (ORC) concept". In: *Appl. Therm. Eng.* 63.1 (2014), pp. 246–253. DOI: 10.1016/j.applthermaleng.2013.11.016.

[8] A. Franco. "Power production from a moderate temperature geothermal resource with regenerative Organic Rankine Cycles". In: *Energy for Sustainable Development* 15.4 (2011), pp. 411–419. DOI: 10.1016/j.esd.2011.06.002.

[9] V. Minea. "Power generation with {ORC} machines using low-grade waste heat or renewable energy". In: *Appl. Therm. Eng.* 69.1-2 (2014), pp. 143–154. DOI: 10.1016/j.applthermaleng.2014.04.054.

[10] R. Abbas. "Anwendung der Gruppenbeitragszustandsgleichung VTPR für die Analyse von reinen Stoffen und Mischungen als Arbeitsmittel in technischen Kreisprozessen". PhD thesis. Technischen Universität Berlin, June 2011.

[11] S. E. Stein. *NIST/EPA/NIH Mass Spectral Library with Search Program, NIST Standard Reference Database 1A*. 1999.

[12] *Wiley Registery of Mass Spectral Data 7th Edition*. 2000. URL: https://www.wiley.com.

[13] S. L. Outcalt and B.-C. Lee. "A Small-Volume Appratus for the Measurement of Phase Equilibria". In: *J. RES. NATL. INST. STAN.* 109.6 (2004), pp. 525–531. DOI: 10.6028/jres.109.039.

[14] G. L. Harris and J. A. Torres. "NIST IR 6969 Selected Laboratory and Measurement Practices and Procedures to Support Basic Mass Calibrations". In: *National Institute of Standards and Technology* (2003).

[15] A. Picard, R. S. Davis, M. Gläser, and K. Fujii. "Revised formula for the density of moist air (CIPM-2007)". In: *Metrologia* 45.2 (2008), p. 149. URL: http://stacks.iop.org/0026-1394/45/i=2/a=004.

[16] E. W. Lemmon, I. H. Bell, M. L. Huber, and M. O. McLinden. *NIST Standard Reference Database 23: Reference Fluid Thermodynamic and Transport Properties - REFPROP, Version 10*. 2018.

[17] J. R. Thome. *Wolverine Engineering Databook III*. Wolverine Tube Inc., 2006.

[18] *JCGM 100: Evaluation of Measurement Data - Guide to the Expression of Uncertainty in Measurement*. Tech. rep. JCGM, 2008.

[19] B. N. Taylor and C. E. Kuyatt. "Guidelines for Evaluating and Expressing the Uncertainty of NIST Measurement Results". In: *NIST Technical Note; U.S. Department of Commerce: Washington, DC* (1994).

[20] B. Everitt and A. Skrondal. *The Cambridge dictionary of statistics*. English. 4th ed. Cambridge University Press Cambridge, UK ; New York, 2010, ix, 468 p. : ISBN: 9780521766999.

[21] S. L. Outcalt and E. W. Lemmon. "Bubble-Point Measurements of Eight Binary Mixtures for Organic Rankine Cycle Applications". In: *J. Chem. Eng. Data* 58.6 (2013), pp. 1853–1860. DOI: 10.1021/je400251s.

[22] E. Mansfield, I. H. Bell, and S. L. Outcalt. "Bubble-Point Measurements of n-Propane + n-Decane Binary Mixtures with Comparisons of Binary Mixture Interaction Parameters for Linear Alkanes". In: *Journal of Chemical & Engineering Data* 61.7 (2016), pp. 2573–2579. DOI: 10.1021/acs.jced.6b00258.

[23] R. Span. *Multiparameter equations of state : an accurate source of thermodynamic property data*. Berlin; New York: Springer, 2000. ISBN: 9783540673118. URL: http://www.worldcat.org/search?qt=worldcat_org_all&q=3540673113.

[24] I. H. Bell and E. W. Lemmon. "Automatic Fitting of Binary Interaction Parameters for Multi-fluid Helmholtz-Energy-Explicit Mixture Models". In: *Journal of Chemical & Engineering Data* 61.11 (2016), pp. 3752–3760. DOI: 10.1021/acs.jced.6b00257.

[25] M. Thol, F. Dubberke, G. Rutkai, T. Windmann, A. Köster, R. Span, and J. Vrabec. "Fundamental equation of state correlation for hexamethyldisiloxane based on experimental and molecular simulation data". In: *Fluid Phase Equilib.* 418.Supplement C (2016). Special Issue covering the Nineteenth Symposium on Thermophysical Properties, pp. 133–151. ISSN: 0378-3812. DOI: 10.1016/j.fluid.2015.09.047.

[26] M. Thol, F. H. Dubberke, E. Baumhögger, J. Vrabec, and R. Span. "Speed of Sound Measurements and Fundamental Equations of State for Octamethyltrisiloxane and Decamethyltetrasiloxane". In: *Journal of Chemical & Engineering Data* 62.9 (2017), pp. 2633–2648. DOI: 10.1021/acs.jced.7b00092.

[27] König and M. Thol. "Helmholtz equation of state for Dodecamethylpentasiloxane (MD_3M) and Tetradecamethylhexasiloxane (MD_4M)". To be published. 2017.

[28] T. W. Leland and P. S. Chappelear. "The Corresponding States Principle A Review of Current Theory and Practice". In: *Industrial & Engineering Chemistry* 60.7 (1968), pp. 15–43. DOI: 10.1021/ie50703a005.

[29] O. Kunz and W. Wagner. "The GERG-2008 Wide-Range Equation of State for Natural Gases and Other Mixtures: An Expansion of GERG-2004". In: *Journal of Chemical & Engineering Data* 57.11 (2012), pp. 3032–3091. DOI: 10.1021/je300655b.

[30] E. W. Lemmon and R. T. Jacobsen. “A New Functional Form and New Fitting Techniques for Equations of State with Application to Pentafluoroethane (HFC-125)”. In: *J. Phys. Chem. Ref. Data* 34.1 (2005), pp. 69–108. DOI: 10.1063/1.1797813.

[31] R. Span and W. Wagner. “On the extrapolation behavior of empirical equations of state”. In: *Int. J. Thermophys.* 18.6 (Nov. 1997), pp. 1415–1443. ISSN: 1572-9567. DOI: 10.1007/BF02575343.

CHAPTER 5

THERMAL STABILITY ANALYSIS OF HEXAMETHYLDISILOXANE AND OCTAMETHYLTRISILOXANE

Part of the contents of this chapter appeared in:

L. Keulen, C. Landolina, A. Spinelli, P. Iora, C. Invernizzi, L. Lietti, and A. Guardone. "Design and commissioning of a thermal stability test-rig for mixtures as working fluids for ORC applications". In: *Energy Procedia* 129.Supplement C (2017), pp. 176–183. ISSN: 1876-6102. DOI: 10.1016/j.egypro.2017.09.102.

The contents of this chapter is in preparation for publication:

L. Keulen, C. Landolina, A. Spinelli, P. Iora, C. Invernizzi, L. Lietti, and A. Guardone. "Thermal stability analysis of hexamethyldisiloxane and octamethyltrisiloxane". In preparation for submission to: *Energy*. 2018.

5.1 Introduction

A key aspect of the design of an ORC power plant is the selection of the working fluid. This selection depends on the source temperature and the size of the power plant. These properties are of great influence on the components within the power plant: heat exchanger, turbine, condenser and pump. The use of mixtures as working fluid can significantly increase the performance of the cycle because the mixture can be optimized so the temperature glide of the mixture matches the glide of the heat source fluid [1]. The use of a working fluid is limited by its thermal stability limit. When the thermal stability limit is exceeded the fluid undertakes a structural decomposition. This can have a large impact on the system and cause loss of power or serious malfunctions of fundamental components [2, 3]. Moderate decomposition give rise to mixtures which might modify the physical and thermodynamic properties of the working fluid and influence cycle performance, but by knowing the mixture properties the system can be adapted without loss of power or replacing the working fluid [4].

Pure siloxane working fluids are prominent, successful working fluids for ORCs and mixtures of siloxanes are promising working fluids for ORCs. Thanks to their high-temperature thermal stability range, siloxanes are of interest for higher temperature applications of ORCs [5]. Siloxane fluids can be separated into two groups, linear and cyclic polymers and composed of alternating silicon oxygen atoms with methyl groups attached to the silicon atoms [6]. In principle, these siloxanes and mixtures of siloxanes can all be used as working fluids in ORCs depending on the power level and heat source temperature [7]. For the use of siloxanes and mixtures of siloxanes, reliable data about thermal stability is necessary as highlighted by Colonna et al. [8]. Several effects can influence the thermal stability of the working fluid besides temperature: the presence of impurities, especially water and oxygen which are almost always present in an actual plant; the time span a fluid is stressed, stressing the fluid at low temperature for an extensive period of time can also cause degradation; the pressure. An expected feature of mixtures of siloxanes is that they exhibit a higher thermal stability limit than their pure components, due to the redistribution process occurring at high temperature, where more complex molecules decompose into simpler molecules, which then recombine again into the more complex molecule [9, 10]. This redistribution and therefore the possible increase of the thermal stability temperature can enhance the use of complex molecular fluids for experimental and industrial applications

Some literature data about thermal stability limits of pure siloxanes are available. Colonna et al. [11] report limits of 400 °C for siloxanes, Angelino et al. [9] provide similar results for cyclic siloxanes. An extensive research on polysiloxanes have been conducted by Dvornic [10] but without mentioning degradation temperatures. A recent study by Preißinger et al. [5] shows a thermal stability temperature of 300 °C for hexamethyldisiloxane (MM) and annual degradation rate of less than 3.5%.

No literature can be found about the influence of siloxane mixtures on the thermal stability.

The method used in this research was introduced by Blake et al. [12], who applied it to more than 100 organic fluids from 12 different chemical families, and is the first methodology that is based on the analysis of isothermal pressure deviations of fluids subjected to different thermal stress temperatures. This method was later used by Fisch et al. [13], Johns et al. [14][15], and Fabuss et al. [16]. Invernizzi developed the first method specifically for the evaluation of working fluids for ORCs based on the methodology from Blake et al. [12] and Calderazzi et al. [17]. Invernizzi introduced the comparison of the vapor pressure before and after the thermal stress to determine decomposition of the fluid. This method has proven to be more effective to determine decomposition than only analyzing the pressure during the stress test. Pressure fluctuation during the stress test indicate thermal decomposition of the fluid, but pressure fluctuation are difficult to observe and thermal decomposition can still have occurred when no pressure fluctuation have been observed.

This research focuses on the design and commissioning of an experimental test-rig to determine thermal stability of pure fluids and mixtures for ORC applications. The method and experimental apparatus in this research is based on the methodology of Calderazzi et al. [17] and Pasetti et al. [18] and uses statistical analysis to determine decomposition based on the deviation in vapor pressure introduced by Pasetti et al. [18]. The apparatus is improved so chemical analysis can be conducted on the decomposition products in the vapor and liquid phase.

The goal of this research is the design and commissioning of an experimental test-rig for the determination of the thermal stability temperature and decomposition products of pure fluids and mixtures through chemical analysis of the liquid and vapor phase. Results are obtained for pure fluids of hexamethyldisiloxane (MM) and octamethyltrisiloxane (MDM). The measurements of mixtures are left for future investigations as well as other organic fluids and effects which can influence the thermal stability limit.

5.2 Experimental apparatus

The experimental apparatus is based on the design of Pasetti et al. [18] and Calderazzi et al. [17]. The set-up is improved for measurements of siloxane fluids and chemical analysis of the liquid and vapor phase. Due to the low vapor pressures of siloxane fluids [7] at temperatures close to ambient temperature, the apparatus is designed to measure low pressures down to 2 mbar. To have the ability to measure a large range of stress temperatures and maintain a good accuracy an intermediate pressure of up to 10 bar can be measured and an upper pressure limit of 35 bar can be reached. Two thermocouples with different tolerance intervals are used to obtain the highest accuracy at each temperature level. Because of the goal to perform chemical analysis on the liquid and vapor phase, a section is added for the extraction of the vapor

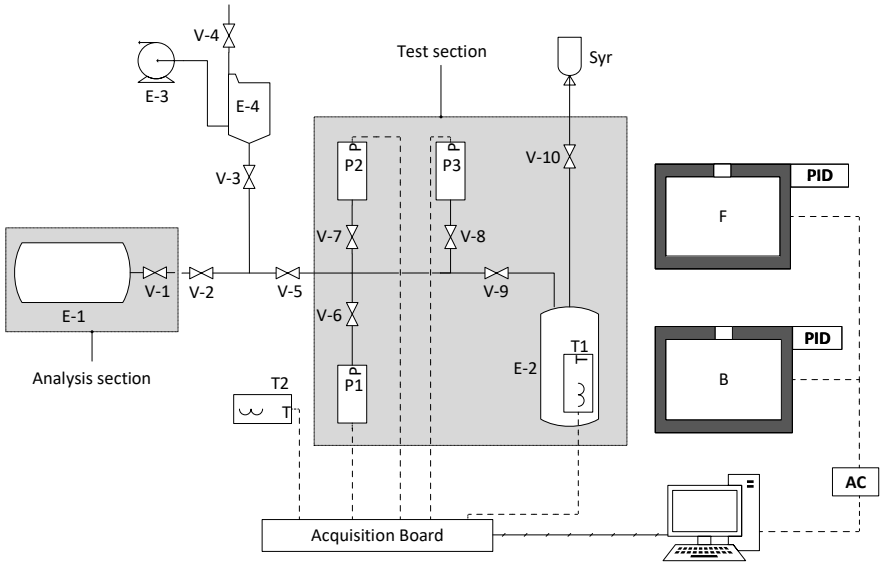

Figure 5.1: Schematic diagram of the thermal stability experimental apparatus: Temperature controlled oven (F), thermal bath (B), 150 ml vessels (E-1,2), pressure transducers (P-1,2,3), thermocouples (T-1,2), valves (V), vacuum pump (E-3), vacuum trap (E-4), loading syringe (Syr).

phase. This is done to capture the more volatile products of thermal decomposition of pure fluid and mixtures, because the vapor and liquid phase compositions can be different. As well as the study of thermal decomposition of mixtures, whose composition depends on the pressure and temperature.

The schematic design of the apparatus used for the thermal stability measurement is shown in Fig. 5.1. The apparatus and the detailed design are shown in Figs. 5.2 and 5.3. The apparatus is divided into two sections, the test section which is used for the vapor pressure measurement and thermal stress test and the analysis section which is used to collect the gas sample for chemical analysis. The vacuum pump (E-3) is used to evacuate the test and analysis section. The fluid is loaded through a syringe (Syr) connected to the test section.

The thermal bath (B) is used for the measurement of the vapor pressure. The heat transfer liquid has a temperature range of -20 °C to 180 °C. The temperature of the bath is controlled by a PID controller with a resolution of 0.1 °C and a stability of $\pm$0.02 °C. The furnace (F) is used for the thermal stress test, and the temperature can be varied from 25 °C to 1200 °C with a resolution of 1 °C and stability of $\pm$2 °C controlled by a PID controller.

The tubing, connectors, valves, and vessels in the test section are 316L stainless-steel to withstand a pressure up to 64 bar at 426 °C. The vessels (E-1,2) have a volume

of approximately 150 ml and are sealed on one end with a clean TIG weld process. The sample vessel is connected by a TIG weld to the loading tube, tube connected to the measuring section, and to the thermo-well The total volume of the circuit is determined at approximately 175 ml.

The measurement instrumentation is made up of three absolute capacitive pressure transducers (P-1,2,3) and two thermocouples (T-1,2). The pressure transducers have full scales of 1 bar, 10 bar and 35 bar and nominal accuracy of 0.05% of FS and exhibiting a linear calibration curve. Possible zero offset of the pressure readings are compensated at atmospheric conditions through a comparison with pressure measured by a high accuracy barometer of 0.15 mbar accuracy. The uncertainty is computed taking into account the contribution of the transducer and the acquisition system [19]. The transducer technical data is shown in Table 5.1. The thermocouples are a T-type for temperatures below 400 °C and K-type for temperature up to 1370 °C. The expanded uncertainty of the thermocouple is taken as 95% confidence interval of the thermocouples tolerance. The thermocouples technical data is shown in Table 5.1.

The digital samples are monitored by the national instruments acquisition system. The acquired data is processed by a model programmed in the LabVIEW® environment.

Table 5.1: Measurement instrumentation specification.

Pressure Transducer:	
Manufacturer	Setra-ASM1
Technology	Capacitance sensor
Measured quantity	Absolute Pressure
Full scale	1 bar, 10 bar, 35 bar
Expanded uncertainty	±0.05% FS

Thermocouple:	
Manufacturer	Tersid-MTS 15000
Technology	Mineral Oxide
Type T (Cu/Cu-Ni)	-133 °C to 400 °C
Type K (Ni-Cr/Ni-Al)	-270 °C to 1370 °C
Expanded uncertainty	$0.0038T$

5.3 Measurement procedure

The procedure used to determine the thermal stability and decomposition of the fluids is described in the following sections. The fluid properties are calculated with REFPROP [20].

5.3.1 Preparation of experimental apparatus

To remove all impurities, the entire test section is disassembled and all the components are immersed in acetone for 30 minutes. Subsequently all the components are baked at 80 °C, cooled down and cleaned with Nitrogen. Subsequently the test section is reassembled and evacuated, then the system is exposed to ambient air and the pressure transducers are compensated for possible zero offset with the pressure readings at atmospheric conditison through a calibration by a high accuracy barometer.

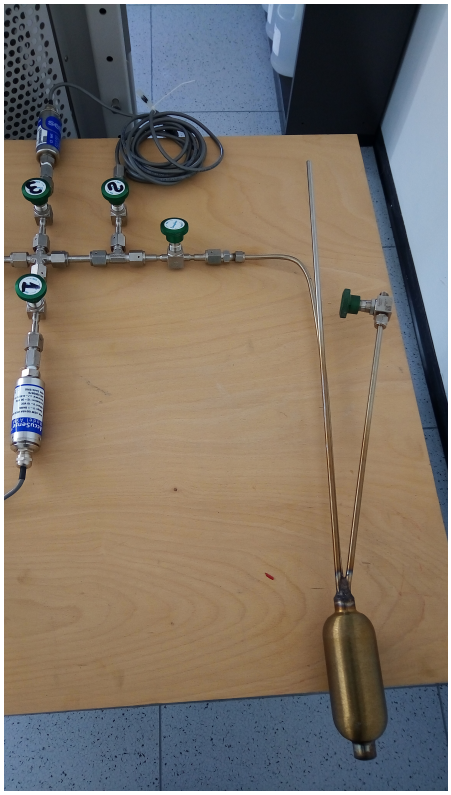

Figure 5.2: Thermal stability set-up shown are the pressure transducers, sample vessel, and loading section.

The first leakage test is performed to check if the circuit is leak proof under vacuum conditions. At ambient conditions the circuit is evacuated to 3.5 mbar, the lowest obtainable pressure with the vacuum pump. After this, the pressure and temperature are registered for ~ 65 hours. The registered pressure is compared to the reference pressure calculated from the ideal gas law to take into account temperature fluctuations during the measurement. Given the temperature $T(t)$ and pressure $P(t)$ at time instant t, the mass of the air in the system is approximated using the ideal gas law as

$$m(t) = \frac{P(t)V}{R_s T(t)}, \tag{5.1}$$

where $m(t)$ is the mass, P the pressure, T the temperature, V the total volume of the circuit given in Section 5.2, and R_s the specific gas constant of the fluid.

The pressure is normalized with respect to the reference temperature using the ideal gas law to highlight if pressure changes depend on temperature fluctuations or

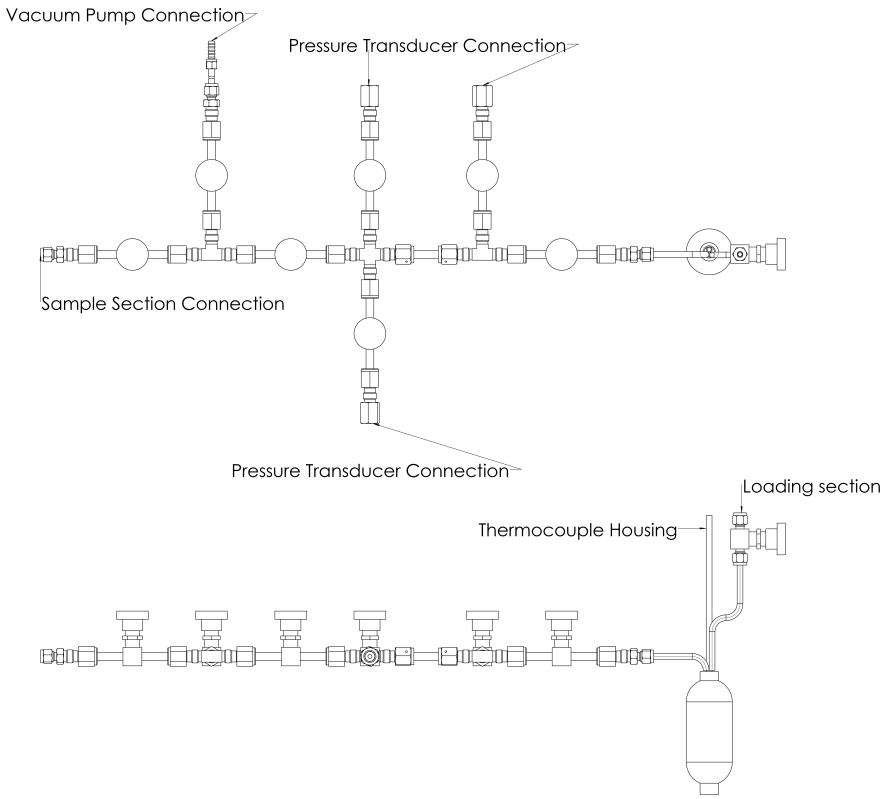

Figure 5.3: Detailed design of thermal stability set-up.

on leakage

$$\hat{P}(t) = \frac{R_s T_{ref}}{V} m(t) = \frac{R_s T_{ref}}{V} \frac{P(t)V}{R_s T(t)} = \frac{T_{ref}}{T(t)} P(t), \tag{5.2}$$

where $\hat{P}$ is the normalized pressure and $T_{ref} = 298.15K$ the reference temperature at ambient conditions. The vacuum leakage test is passed if the registered pressure does not deviate more than 0.05 kPa from the normalized pressure, the uncertainty of the 1 bar pressure transducers.

Second the pressure leakage test is performed by pressurizing the system with helium at ± 10 bar. The temperature and pressure are registered for ~ 65 hours, the registered pressure is again normalized using the ideal gas law. The pressure leakage test is passed if the normalized pressure does not deviate more than 1.75 kPa, the uncertainty of the 35 bar pressure transducer. The leakage test measurements for the test with MM and MDM are shown in Section 5.A. After the cleaning and leakage tests the circuit is set under 3.5 mbar vacuum.

5.3.2 Preparation, loading and degasification of the fluid sample

The fluid quantity to be loaded into the circuit is determined taken in consideration that (i) the pressure must not exceed the full scale of the highest pressure transducer (P_{FS} = 35 bar), (ii) during the vapor pressure measurement the fluid remains in two-phase conditions and (iii) ensure the fluid is in the vapor phase during the thermal stress tests.

To ensure the maximum pressure is not exceeded, the maximum mass that can be loaded is calculated as follows

$$m_{max} = \rho(T_{max},\ P_{FS})V_{circuit}, \tag{5.3}$$

where m_{max} is the maximum mass, ρ the density estimated at the maximum stress temperature T_{max} and pressure P_{FS}, and $V_{circuit}$ is the total volume of the circuit as stated in Section 5.2.

During the vapor pressure measurement the fluid has to remain in two-phase conditions. This is checked by estimating the saturation density of the liquid, ρ_l, and vapor, ρ_v, at the measured temperatures during the vapor pressure test. The fluid mass, m_{fluid}, is then chosen using the liquid and vapor density to ensure the fluid remains in two-phase conditions for all temperatures and checked that it does not exceed the maximum mass by

$$\rho_v(T_{vap}) < \frac{m_{fluid}}{V_{circuit}} < \rho_l(T_{vap}). \tag{5.4}$$

The specific fluid mass will be loaded into a syringe. To determine the quantity to be loaded the specific fluid volume at ambient conditions is estimated as

$$V_{fluid,amb} = \frac{\rho_{amb}(T_{amb},\ P_{amb})}{m_{fluid}}. \tag{5.5}$$

To check that the mass does not exceed the limits the syringe mass is measured before and after the loading of the fluid. The difference in mass is the fluid mass which is loaded into the circuit.

The fluid is loaded into the circuit by connecting the syringe to the test section shown in Fig. 5.1. After the loading procedure the fluid is degassed to remove air and other non-condensable gases. For degasification the circuit is put in the thermal bath at 50 °C for one hour to facilitate the gas expulsion. Subsequently the fluid is maintained at -40 °C and degassed using the vacuum pump. This procedure is repeated until the pressure after two consecutive steps returns to the same value to ensure all non-condensable gases are extracted from the system.

5.3.3 Thermal stress measurement

Vapor pressure measurement of the reference fluid: The vapor pressure of the non-stressed fluid, also called reference fluid, is measured as reference to determine decomposition by comparison with the stressed fluids vapor pressures. The temperature

range is chosen taking into account the range of the thermal bath and the accuracy of the lowest full scale pressure transducer as stated in Section 5.2 so the pressure remains above the transducers uncertainty during the vapor pressure measurement. Each pair of $P-T$ values is recorded for 10 minutes corresponding to 120 acquisition samples.

Thermal stress test: The sample vessel containing the fluid under scrutiny is placed in a vertical oven for $\sim$ 80 hours at a constant temperature (T_{stress}). During the test, pressure and temperature are monitored by the acquisition system. The fluid is in the vapor phase during all the thermal stress tests and therefore the composition is homogeneous in the system. It is possible that condensation occurs in the lines outside of the furnace, but due to the continuous flowing of gases through the system it is assumed that all the fluid is stressed equally during the 80 hours.

Vapor pressure measurement of the stressed fluid: After the thermal stress test, the vapor pressure of the stressed fluid is measured using the same experimental procedure and temperature range as for the reference fluid.

5.3.4 Fluid extraction and chemical analysis

Chemical analysis is performed at the end of the measurement campaign and when decomposition is detected by comparing the reference and stressed fluid vapor pressure, see Section 5.4 for decomposition criteria. The chemical analysis is performed using gas chromatography, flame ionization detection, thermal conductivity detection, and mass spectrometry techniques.

The gas chromatograph (GC) is a chemical analysis instrument for separating chemicals in a sample. It is composed by an inert gas carrier, that carries the sample through the column. The column is a glass or metal tube, coated with a microscopic layer of liquid or polymer on an inert solid support. The sample interacts with the coating and within the column. Since each type of molecule in the sample has its own rate of interaction with the coating, various components of the sample are separated as they progress along the column and reach the end of the column at different times.

The flame ionization detector (FID) is composed by two electrodes placed adjacent to a hydrogen/air flame. When carbon containing compounds exit the column, they are pyrolyzed by the flame. This detector works only for organic/hydrocarbon containing compounds due to the ability of the carbon to form a positively charged ion and electrons upon pyrolysis which generates a current between the electrodes. The increase in current is translated and appears as a peak in the chromatogram.

The thermal conductivity detector (TCD) relies on the thermal conductivity of the molecules in the sample passing around a Tungsten-Rhenium filament with a current traveling through it. In this set up, helium or nitrogen are used as carrier gas due to their relatively high thermal conductivity which keeps the filament cool and

maintains uniform resistivity and electrical efficiency of the filament. However, when the sample molecules elute from the column, mixed with carrier gas, the thermal conductivity decreases and this causes a detector response. The response is due to the decreased thermal conductivity causing an increase in filament temperature and resistivity resulting in fluctuations in voltage.

The mass spectrometer (MS) breaks each molecule into ionized fragments using electrons. These ions are then separated according to their mass to charge ratio. To do that ions are accelerated and deflected by a magnetic field. The deflection depends on the mass of the ions, lighter ions will deflect more, and the charge of the ions, ions with a greater charge deflect more. The ions are subsequently detected by a mechanism capable to identify charged particles. Results are displayed as spectra of the detected ions as a function of their mass to charge ratio. Each molecule has its own fragmentation pattern and so the molecules in the sample can be identified by comparing the specific fragmentation pattern with the data in chemical libraries

Both liquid and vapor phase of the stressed fluid are evaluated. If decomposition is detected, the analysis vessel, pressurized (ca. 8 bar) with a He/N_2/Ar mixture (N_2 1% v/v as internal standard), is connected to the system and the line is evacuated. Then the valve connecting the analysis vessel (E-1) shown in Fig. 5.1, previously evacuated and set under vacuum, is opened and accordingly part of the gaseous mixture flows spontaneously into the vessel to balance the pressure in the system and dilute the gases formed upon decomposition. Therefore this procedure allows the extraction of the gases formed within the sample vessel (E-2).

The analysis vessel (E-1) is eventually detached from the apparatus and the gas phase mixture sample is analyzed by GC analysis, using a micro-GC equipped with 2 capillary columns (molecular sieve and poraplot Q) in a parallel arrangement, connected to TCDs. This method allows the quali-quantitative analysis of the gaseous species formed into the sample vessel upon the thermal treatment of the fluid. The composition of the liquid of the stressed fluid is also determined; for this purpose samples are taken from the test vessel and analyzed by High Resolution GC (HRGC) by using a gas chromatograph equipped with capillary columns attached to the FID and to the MS, respectively. The area of the spectral peaks with respect to the largest area peak is obtained and the relative peak percentage is calculated to determine the composition. Because the chemical analysis compositions are given in relative percentage between the detected components, this percentage does not correspond to the molar or mass fraction of each component. The chemical analysis allowed for the quali-quantitative analysis of the fluid composition.

5.4 Data analysis

To evaluate the thermal stability and decomposition of the stressed fluid three analysis are conducted. Those consist in measuring (i) deviations of pressure during each thermal stress test, (ii) deviations of fluid vapor pressures after it has undergone each

thermal stress test, from reference fluid vapor pressures, and (iii) compositions of the finally decomposed fluid.

The analysis of the pressure deviation during the thermal stress tests is an adequate method to detect large decomposition phenomena, but often it is inadequate to identify weaker decomposition phenomena. Vapor pressure deviations are thus evaluated at low temperature because those are easier and more accurate to measure. This method allows a more sensitive evaluation of decomposition phenomena. Chemical analysis of the liquid and gas phase are finally performed to identify the decomposition products. Both phases are analyzed to take into account the different composition between the liquid and gas phase in mixtures.

5.4.1 Pressure deviation during thermal stress test

The first evaluation is the analysis of the pressure deviation during the thermal stress tests. Because of the difficulty in reproducing and maintaining exact isothermal conditions during the thermal stress, the analysis is performed by comparing the percentage deviation of pressure and temperature over time by

$$T^{\%}_{\text{stress}} = \left(\frac{T}{T_0} - 1\right) \times 100\%, \qquad P^{\%}_{\text{stress}} = \left(\frac{P}{P_0} - 1\right) \times 100\%, \tag{5.6}$$

where T_0 and P_0 are the initial pressure and temperature and $T^{\%}_{\text{stress}}$ and $P^{\%}_{\text{stress}}$ the percentage deviation of the pressure and temperature from the initial values. Any deviation in pressure that is not supported by a comparable deviation in temperature indicates possible thermal decomposition. Variation in the percentage deviation indicates fluid decomposition, but it is insufficient to exclude decomposition if no variation is observed.

5.4.2 Deviation of stressed fluid vapor pressure from reference fluid vapor pressure

The second evaluation is based on the deviation of the stressed fluids vapor pressure from the reference fluid vapor pressure as described by Pasetti et al. [18]. The purpose of the vapor pressure analysis is the identification of deviations that can not be justified by measurement uncertainties. The composition of the loaded non-stressed fluid is known for pure fluids and for the mixtures. First the vapor pressure of the non-stressed fluid is measured and the stressed fluid after every stressed test as described in Section 5.3. Every stressed fluid vapor pressure is compared to the non-stressed fluid vapor pressure. Because the stressed fluid is directly compared to the non-stressed fluid, and the same experimental measurement procedure is performed, any deviation in vapor pressure indicates a change in the composition of the pure fluid or mixture and so thermal decomposition. This method only uses the difference in vapor pressure between non-stressed and stressed fluid as indication for thermal

decomposition and can not be used for Vapor-Liquid Equilibrium measurements. For the uncertainty analysis the uncertainty in composition and air are not taken into account, because the analysis is a comparison between the reference fluid and the stressed fluid so any impurities will not affect the difference in vapor pressure.

First the vapor pressure of the non-stressed fluid, also called reference fluid, is evaluated. The vapor pressure data of the reference fluid is interpolated by means of the Clausius-Clapeyron equation [21]

$$\frac{dP_{\text{vap}}}{dT} = \frac{\Delta H_{\text{v}}}{T\Delta V_{\text{v}}} = \frac{\Delta H_{\text{v}}}{(RT^2/P_{\text{v}})\Delta Z_v}, \tag{5.7}$$

$$\frac{d\ln(P_{\text{vap}})}{d(1/T)} = -\frac{\Delta H_{\text{v}}}{R\Delta Z_{\text{v}}}, \tag{5.8}$$

where P_{vap} is the saturated vapor pressure, T the temperature, ΔH_{v} the enthalpy of evaporization, and ΔZ_{v} the differences in compressibility factor between saturated liquid and vapor. The assumption is made that $\Delta H_{\text{v}}/\Delta Z_v$ is a constant value and independent from temperature. By integrating Eq. (5.8) with the constant of integration A, the following equation is obtained which is a simplified version of the Antoine equation

$$P_{\text{vap}} = \exp\left(A - \frac{B}{T}\right), \tag{5.9}$$

where $B = \Delta H_v/(R\Delta Z_v)$. The vapor pressure data of the reference fluid will be interpolated using Eq. (5.9) to obtain an equation for the reference pressure as function of the temperature. This is a good approximation for vapor pressure over small temperature intervals and the reference pressure is defined as

$$P_{\text{ref}}(T) = \exp\left(A - \frac{B}{T}\right). \tag{5.10}$$

The total number of vapor pressure data points n taken as the arithmetic mean of the recorded P-T values of the virgin fluid are interpolated obtaining the reference vapor pressure curve. The regression analysis is performed by applying the following transformation of variables to Eq. (5.10) and given by

$$x_i = \frac{1}{T_i} \qquad y_i = \ln(P_i) \qquad i = 1 \ldots n. \tag{5.11}$$

Applying the Gram-Schmidt orthogonalization Leon et al. [22] the following equation is obtained

$$y = \tilde{\alpha}_0 + \tilde{\alpha}_1(x - \bar{x}), \tag{5.12}$$

where $\tilde{\alpha}_0$ and $\tilde{\alpha}_1$ are calculated by applying the least square method to all the n acquired vapor pressure data. Knowing $\tilde{\alpha}_0$ and $\tilde{\alpha}_1$ the interpolation coefficients A

and B of the Antoine equation are calculated as

$$A = \bar{y} - \bar{x}\frac{\sum_{i=1}^{n} y_i(x_i - \bar{x})}{\sum_{i=1}^{n}(x_i - \bar{x})^2}, \qquad B = -\frac{\sum_{i=1}^{n} y_i(x_i - \bar{x})}{\sum_{i=1}^{n}(x_i - \bar{x})^2}, \tag{5.13}$$

where the index i refers to the arithmetic mean of the measured $P - T$ values and $\bar{x}$ and $\bar{y}$ are the arithmetic means of x_i and y_i respectively

$$\bar{x} = \frac{\sum_{i=1}^{n} x_i}{n} \qquad \bar{y} = \frac{\sum_{i=1}^{n} y_i}{n}. \tag{5.14}$$

The uncertainty of y is evaluated by applying the law of propagation of uncertainty to Eq. (5.12) taking into account the variance of the regression coefficients $u^2(\tilde{\alpha}_0)$ and $u^2(\tilde{\alpha}_1)$ and the variance of the errors of the model σ_0^2 gives

$$u^2(y) = \sum_{i=0}^{1}\left[\frac{\partial y}{\partial \tilde{\alpha}_i} u(\tilde{\alpha}_i)\right]^2 + \sigma_0^2. \tag{5.15}$$

The uncertainty of the reference equation is determined using the method from Leon et al. [22] and Montgomery et al. [23] and given by

$$u^2(P_{\text{ref}}) = u^2_{\text{mod}}(P_{\text{ref}}) + u^2_{\text{ins}}(P_{\text{ref}}), \tag{5.16}$$

which is the sum of the uncertainties related to the model uncertainty $u^2_{\text{mod}}(P_{\text{ref}}(T))$ and uncertainty contribution of the measurement instruments $u^2_{\text{ins}}(P_{\text{ref}}(T))$ [18]. The uncertainty due to the model non linearity is obtained by propagating the uncertainty of y defined in Eq. (5.15) into Eq. (5.10) and taking into account the transformation of variables, giving the following model uncertainty

$$u^2_{\text{mod}}(P_{\text{ref}}) = (P_{\text{ref}}(T))^2\left[u^2(A) + \frac{u^2(B)}{T}\left(\frac{1}{T} - 2\bar{x}\right) + \sigma_0^2\right], \tag{5.17}$$

with the parameters given as

$$u^2(A) = \frac{\sigma_0^2}{n} + \bar{x}^2\frac{\sigma_0^2}{\sum_{i=1}^{n}(x_i - \bar{x})^2} \tag{5.18}$$

$$u^2(B) = \frac{\sigma_0^2}{\sum_{i=1}^{n}(x_i - \bar{x})^2}, \tag{5.19}$$

$$\sigma_0^2 = \frac{\sum_{i=1}^{n}(A - Bx_i - y_i)^2}{n-2}. \tag{5.20}$$

The uncertainty contributed by the measuring instruments is

$$u^2_{\text{ins}}(P_{\text{ref}}) = \left[\frac{\partial P_{\text{ref}}}{\partial T} u_{\text{ins}}(T)\right]^2 + u^2_{\text{ins}}(P), \tag{5.21}$$

here $u_{\text{ins}}(T)$ is the thermocouple uncertainty and $u_{\text{ins}}(P)$ the pressure transducer uncertainty stated in Section 5.2.

Subsequently the deviation is determined at temperature T, between the vapor pressure of the fluid after the thermal stress test $P_{T_{\text{stress}}}|_T$ and the reference fluid $P_{\text{ref}}(T)$ which is defined as

$$\Delta P^{\text{ref}}_{T_{\text{stress}}}|_T = P_{T_{\text{stress}}}|_T - P_{\text{ref}}(T). \tag{5.22}$$

Here the subscript T_{stress} indicates the temperature at which the fluid is stressed and T the temperature at which the vapor pressure is measured. The temperature at which the stressed fluid vapor pressure is measured is used to calculate the reference pressure $P_{\text{ref}}(T)$ using Eq. (5.10) with the coefficient obtained for the reference fluid. The uncertainty of the deviation is expressed as suggested by Hugh W. et al. [24]

$$u^2\left[\Delta P^{\text{ref}}_{T_{\text{stress}}}|_T\right] = u^2(P_{T_{\text{stress}}}|_T) + u^2_{\text{mod}}(P_{\text{ref}}), \tag{5.23}$$

where the uncertainty of the stressed fluid vapor pressure is defined as

$$u^2\left(P_{T_{\text{stress}}}|_T\right) = \left[\frac{\partial P_{\text{ref}}}{\partial T} u_T(T)\right]^2 + u^2_P(P), \tag{5.24}$$

with $u^2_T(T)$ and $u^2_P(P)$ being a combination of the measuring instrument uncertainties and variance of the measured temperature and pressure data points

$$u^2_T(T) = u^2_{\text{ins}}(T) + \frac{\sigma^2_0(T)}{m} \qquad u^2_P(P) = u^2_{\text{ins}}(P) + \frac{\sigma^2_0(P)}{m}, \tag{5.25}$$

here m is the total number of data points recorded during the vapor pressure measurement. The variances σ^2_0 of the recorded temperature and pressure data are

$$\sigma^2_0(T) = \frac{1}{m-1}\sum_{j=1}^{m}(T_j - \bar{T})^2 \qquad \sigma^2_0(P) = \frac{1}{m-1}\sum_{j=1}^{m}(P_j - \bar{P})^2, \tag{5.26}$$

where j refers to the measured data point and $\bar{T}$ and $\bar{P}$ are the arithmetic mean of the recorded temperature and vapor pressure data points respectively.

The confidence index of the vapor pressure deviation $i_C(\Delta P^{ref}_{T_s}|_T)$ is defined and evaluated, as suggested by Pasetti et al. [18]. By evaluating the confidence index a clear distinction can be made between pressure deviation related to the system uncertainty and deviation that indicate a real sign of decomposition. The confidence index is defined as

$$i_C(\Delta P^{\text{ref}}_{T_{\text{stress}}}|_T) = \frac{\Delta P^{\text{ref}}_{T_{\text{stress}}}|_T}{u\left[\Delta P^{\text{ref}}_{T_{\text{stress}}}|_T\right]}. \tag{5.27}$$

The coverage factor k_{p} is applied in order to explain deviation of the measurement procedure. The confidence index is equal to the coverage factor, from this it

follows that the larger the confidence index, the lower is the probability that the deviation from the reference value can be justified by the measurement uncertainty. The following assumptions are made with given confidence levels of $p_1 = 90\%$ and $p_2 = 99\%$ with respectively coverage factors of $k_{p_1} = 1.645$ and $k_{p_2} = 2.576$:

- $|i_C(\Delta P)| \leq k_{p_1}$, the pressure deviation can be reasonably explained by the measurement uncertainty.
- $k_{p_1} < |i_C(\Delta P)| \leq k_{p_2}$, the pressure deviation can be explained by the measurement uncertainty only by extending it to high confidence levels. This means that the measured pressure change can be attributed, with high probability, to decomposition of the fluid.
- $|i_C(\Delta P)| > k_{p_2}$: the pressure deviation can be explained by extending the measurement uncertainty over the 99% confidence levels. This means that the pressure deviation certainly represents the effect of decomposition of the fluid.

5.5 Results and discussion

The primary goal of this research was the design and commissioning of a thermal stability test-rig. The test-rig is build to determine the thermal stability and decomposition products for pure fluids and mixtures as working fluids for ORC applications. The thermal stability temperature for the fluids MM and MDM are determined, the results are elaborated in the following sections.

5.5.1 Hexamethyldisiloxane

The linear siloxane fluid MM is thermally stressed. The fluid purity of MM as stated by the supplier is larger than 99.4%, which is confirmed by chemical analysis conducted on the fluid listed in Table 4.1.

The sample of MM is tested for several temperatures following the procedure in Section 5.3. The loaded MM sample has a mass of approximately 18 grams and stressed from 200 °C to 320 °C with increments of $\Delta T = 20$ °C.

The vapor pressure is measured in the range between -20 °C and 10 °C, with increments of $\Delta T = 5$ °C. The measured vapor pressure data with uncertainties P_{vap} of the reference fluid along with the calculated reference curve P_{ref} is shown in Fig. 5.1. As seen in the picture the vapor pressure measurements stay within the limits of the reference curve uncertainties which indicate a good estimation of the reference curve.

The temperature and pressure are registered during the thermal stress test, the results are shown in Fig. 5.B.1. During the tests no pressure deviations occur, which are not relatable to temperature fluctuations, thus showing no evidence of fluid decomposition. Though large temperature fluctuations are observed during the thermal stress test, up to 5%. This can be related to ambient temperature fluctuations in the

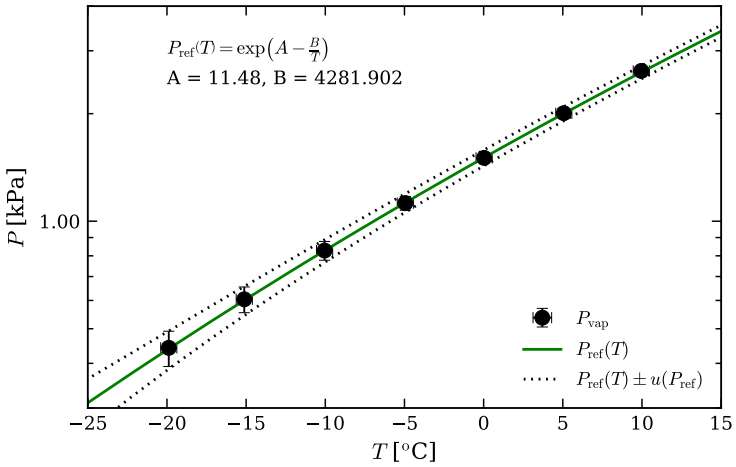

Figure 5.1: Vapor pressure of reference MM fluid. The figure shows the vapor pressure of the reference fluid (•) including uncertainties. The reference curve is given by the green line(−) and the dotted lines (···) show the reference curve including uncertainty.

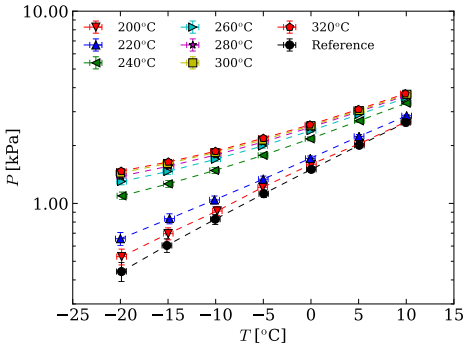

Figure 5.2: Vapor pressure measurement of MM after the various stress tests including uncertainties.

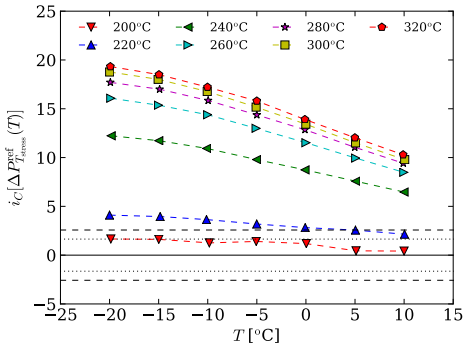

Figure 5.3: Confidence index of the vapor pressure deviation between the reference fluid and stressed MM fluid. The dashed lines (−−) represent the 99% confidence level and the dotted lines (···) the 90% confidence level.

Table 5.1: Chemical analysis results of liquid reference MM fluid and liquid and gas phase of stressed MM fluid. The results for the reference fluid and liquid phase are given in relative percentage between detected components and the vapor phase is given in μmol.

Component	Reference [Peak %]	Liquid [Peak %]
MOH	0.089	0.0903
MM	99.748	99.067
D_3	-	0.0146
D_4	0.0021	0.6834
Undefined	0.16	0.1451

Component	Vapor [μmol]
Methane	1.190
Ethylene	0.057
Ethane	0.085
CO_2	0.256

room and cooled down fluid vapor returning from the measurement section outside of the oven into the sample vessel.

Although the analysis during the thermal stress test does not reveal thermal decomposition, the vapor pressure deviations in Fig. 5.2 show deviation from the reference fluid and thus indicating thermal decomposition. The confidence analysis in Fig. 5.3 reveals already decomposition at 240 °C above the 99% level of confidence, which surely represents the effect of thermal decomposition. From 240 °C and higher the confidence index increases, indicating further decomposition.

Decomposition is also observed by chemical analysis, though the decomposition is very limited. Table 5.1 shows the decomposition of the reference MM fluid, the reference fluid and the liquid phase are given in relative percentage between the detected components, this percentage does not correspond to the molar or mass fraction of each component. The content of MM in the liquid phase decreases from 99.7481% to 99.0667%. Some components could not be verified by the database [25] and are listed as undefined. The vapor phase analysis shows that volatile gases in the order of μmol are formed due to decomposition.

5.5.2 Octamethyltrisiloxane

The linear siloxane fluid MDM is thermally stressed. The fluid purity of MDM as stated by the supplier is larger than 99.7%, which is confirmed by chemical analysis conducted on the fluid listed in Table 4.1.

Two samples of MDM were tested for several temperatures. The first sample 18 grams was stressed at 200 °C and 250 °C. Because the first sample evaporated at higher temperatures and the fluid temperature was not properly controlled, a new sample was loaded for further tests. The second sample of 9.5 grams was stressed from 260 °C to 350 °C.

The vapor pressure is measured in the range between 10 °C and 50 °C, with increments of ΔT = 10 °C [10 °C, 30 °C] and ΔT = 5 °C [30 °C, 50 °C]. The measured vapor pressure data with uncertainties P_{vap} of the reference fluid along with the calculated reference curve P_{ref} is shown in Fig. 5.1. As seen in the picture the va-

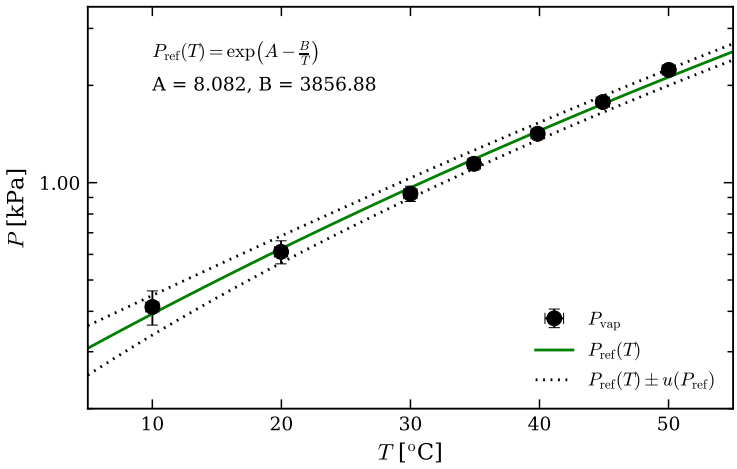

Figure 5.1: Vapor pressure of reference MDM fluid. The figure shows the vapor pressure of the reference fluid (•) including uncertainties. The reference curve is given by the green line (—). and the dotted lines (···) show the reference curve including uncertainty.

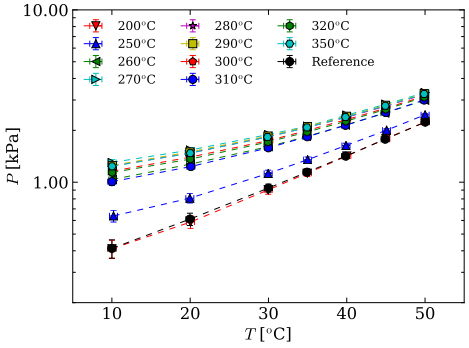

Figure 5.2: Vapor pressure measurement of MDM after the various stress tests including uncertainties.

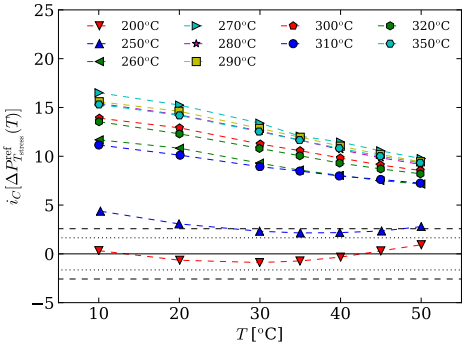

Figure 5.3: Confidence index of the vapor pressure deviation between the reference fluid and stressed MDM fluid. The dashed lines (——) represent the 99% confidence level and the dotted lines (···) the 90% confidence level.

por pressure measurements stay within the limits of the reference curve uncertainties which indicate a good estimation of the reference curve.

The temperature and pressure are registered during the thermal stress test. During the tests no pressure deviations occur, which are not relatable to temperature fluctuations, thus showing no evidence of fluid decomposition. The registered temperature and pressure are shown in Fig. 5.B.2.

Although the analysis during the thermal stress test does not reveal thermal de-

Table 5.1: Chemical analysis results of liquid reference MDM fluid and liquid and gas phase of stressed MDM fluid. The results for the reference fluid and liquid phase are given in relative percentage between detected components and the vapor phase is given in μmol.

Component	Reference [Peak %]	Liquid [Peak %]
MOH	0.0028	0.0061
MM	0.0028	0.0182
MDM	99.972	99.917
D_4	0.0117	0.0145
MD_2M	0.0039	0.0113
Undefined	0.0065	0.0287

Component	Vapor [μmol]
Methane	0.948
Ethylene	0.025
Ethane	0.050
CO_2	0.524

composition, the vapor pressure deviations in Fig. 5.2 show deviation from the reference fluid and thus indicating thermal decomposition. The confidence analysis in Fig. 5.3 reveals already decomposition at 250 °C between 90% and 99% level of confidence. For higher temperatures the confidence index increases above the 99% level of confidence, which surely represents the effect of thermal decomposition. From 260 °C and higher the confidence index stagnates, indicating no further decomposition after 260 °C.

For MDM limited decomposition is also observed by chemical analysis. Table 5.1 shows the decomposition of the reference MDM fluid. The MDM content in the liquid phase decreases from 99.972% to 99.917%. The vapor phase analysis shows that volatile gases are also formed for MDM in the order of μmol due to decomposition.

5.6 Assessment of the thermal stability on the fundamental derivative of gas dynamics

The thermal stability limit affects the capability of a fluid to exhibit non-ideal fluid dynamic effects $\Gamma < 1$ and non-classical gas dynamic effects $\Gamma < 0$. When the temperature of a fluid is above the thermal stability limit, the fluid will decompose and decomposition products will form, which changes the thermodynamic properties of the fluid. The change of thermodynamic properties due to decomposition affects Γ and so the region where $\Gamma < 1$ and $\Gamma < 0$ region.

The linear siloxanes, MM and MDM, are capable to exhibit non-ideal fluid dynamic effects when the Γ is smaller than one. MM and MDM are not capable to exhibit non-classical gas dynamic effects ($\Gamma < 0$). Fig. 5.1 shows the pressure as function of temperature and the region where $\Gamma < 1$ calculated with the Helmholtz energy model [20]. The shaded area indicates the region of temperatures from where thermal decomposition occurs. Fig. 5.1 shows that the $\Gamma < 1$ region for MM and MDM is largely at higher temperatures than the thermal stability temperature of the fluids, while the pressures are comparatively moderate. For MM the minimum value

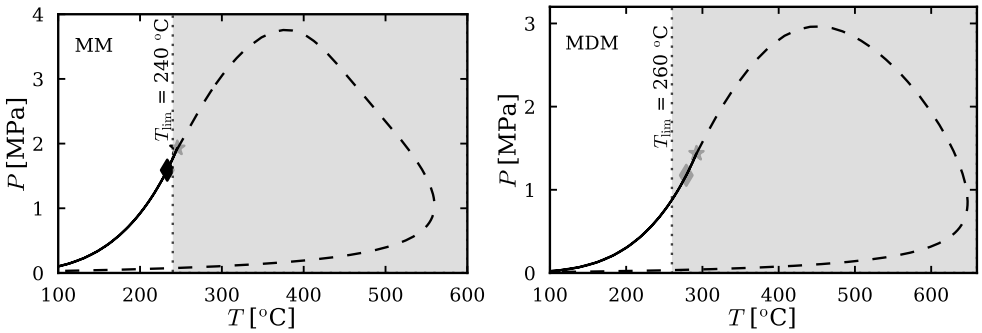

Figure 5.1: $\Gamma = 1$ curve indicated by dashed line (– –) in the *P–T* thermodynamic plane for MM (left) and MDM (right). The saturation curve is indicated by the solid line, the circle indicates the critical point and the diamond the position of Γ_{min}. The shaded area indicates the range of thermal decomposition temperatures.

of Γ_{min} is outside of the thermal stability region, where for MDM the value of Γ_{min} is within the thermal stability region. Due to the thermal stability temperature of MM and MDM there is only a small region where the fluids can exhibit non-ideal fluid dynamic effects. Thermal stability also influence other organic fluids, like more molecular complex linear siloxanes, which can exhibit non-classical gas dynamic effects. It is relevant for future research to assess the thermal stability limit for the more molecular complex organic fluids to determine the capability to reach the temperatures for which the fluid can exhibit non-classical gas dynamic effects.

5.7 Conclusion

In this work the design and methodology of an experimental test-rig for the determination of thermal stability and decomposition products for ORC systems has been presented. The test-rig is designed to determine thermal stability temperatures based on methods already used in literature. Though the novelty of the set-up is the possibility to obtain the decomposition products by chemical analysis of the liquid and vapor phase. This is an important addition to determine the decomposition products and the measurement of mixtures. Because the composition between the vapor and liquid phase can vary due to a possibly larger concentration of volatile products in the vapor phase. In this work, the thermal stability limit and decomposition products of pure fluids are determined.

Together with the description of the apparatus and test methodology, the thermal stability temperature and decomposition products of MM and MDM were determined. MM was stressed under various temperatures ranging from 200 °C to 320 °C, MDM was stressed between 200 °C and 350 °C. Both fluids were analyzed by pressure deviation during the stress test as well as vapor pressure deviations from the

reference fluid in Figs. 5.2 and 5.3 for MM and Figs. 5.2 and 5.3 for MDM. Finally chemical analysis, GC, MS and FID, were performed to determine the decomposition products.

For MM pressure deviations during the thermal stress test showed no sign of thermal decomposition. But based on the results of the deviation of the vapor pressure from the reference fluid in Fig. 5.3 it showed that appreciable decomposition of MM occurs at 240 °C and higher. Decomposition was also verified by chemical analysis of the liquid and vapor phase of the stressed fluid, though the decomposition was very limited as seen in Table 5.1. Volatile gases formed as decomposition products, these volatile gases can have a large influence on the fluid properties because of the low vapor pressure of MM in comparison with the formed volatile gases. When the fluid is stressed for a longer period more volatile gases form and the effect of these gases can have a larger impact on the behavior of the fluid.

Also for MDM pressure deviations during the thermal stress test showed no sign of thermal decomposition. But analysis of the deviation of the vapor pressure from the reference fluid showed that appreciable decomposition of MDM is occurring at 250 °C and stabilizes at 260 °C and higher. Indicating no further decomposition after 260 °C. Rearranging of molecules could occur, creating equilibrium conditions with varying compositions. Decomposition was also verified by chemical analysis of the liquid and vapor phase of the stressed fluid, though the decomposition was very limited as seen in Table 5.1. Volatile gases were also formed as decomposition products from MDM.

It can also be concluded that large temperature fluctuation occurred during the thermal stress test, which made it difficult to determine a precise thermal stability temperature. As mentioned in Section 5.5 the fluctuation in ambient temperature as well as cooled vapor returning into the sample vessel can have a large influence on the temperature. For future research the set-up, specifically the measuring section, will be updated to be more thermally isolated and kept at a constant temperature during the stress test and vapor pressure measurements of other pure fluids and mixtures. For this reason the measurements of mixtures are left for future research.

To conclude, the thermal stability temperature on the fundamental derivative of gas dynamics is assessed for MM and MDM. The region for which the fluids can exhibit non-ideal fluid dynamic effects when $\Gamma < 1$ is evaluated. For both fluids, most of the $\Gamma < 1$ region is above the decomposition temperature, therefore the fluids are only capable of exhibiting non-ideal fluid dynamic effects at the lower temperatures of the $\Gamma < 1$ region without risking decomposition and affecting the thermodynamic properties of the fluid.

Appendix

5.A Leakage test

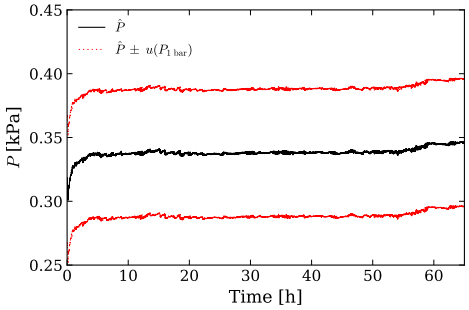

Figure 5.A.1: MDM vacuum leakage test.

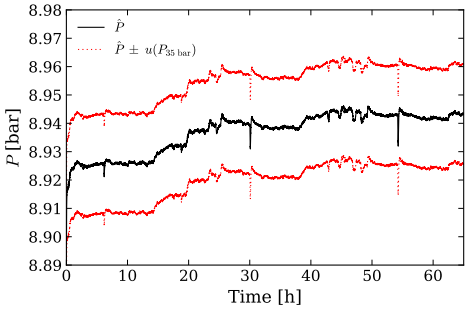

Figure 5.A.2: MDM pressure leakage test.

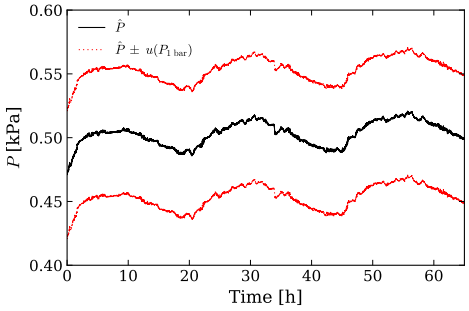

Figure 5.A.3: MM vacuum leakage test.

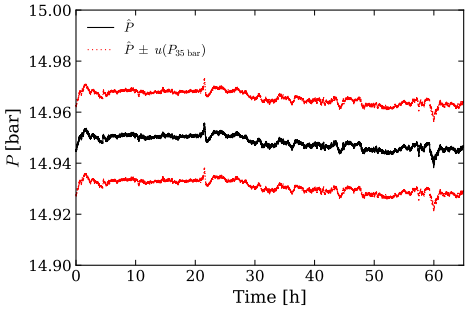

Figure 5.A.4: MM pressure leakage test.

5.B Thermal stress measurements

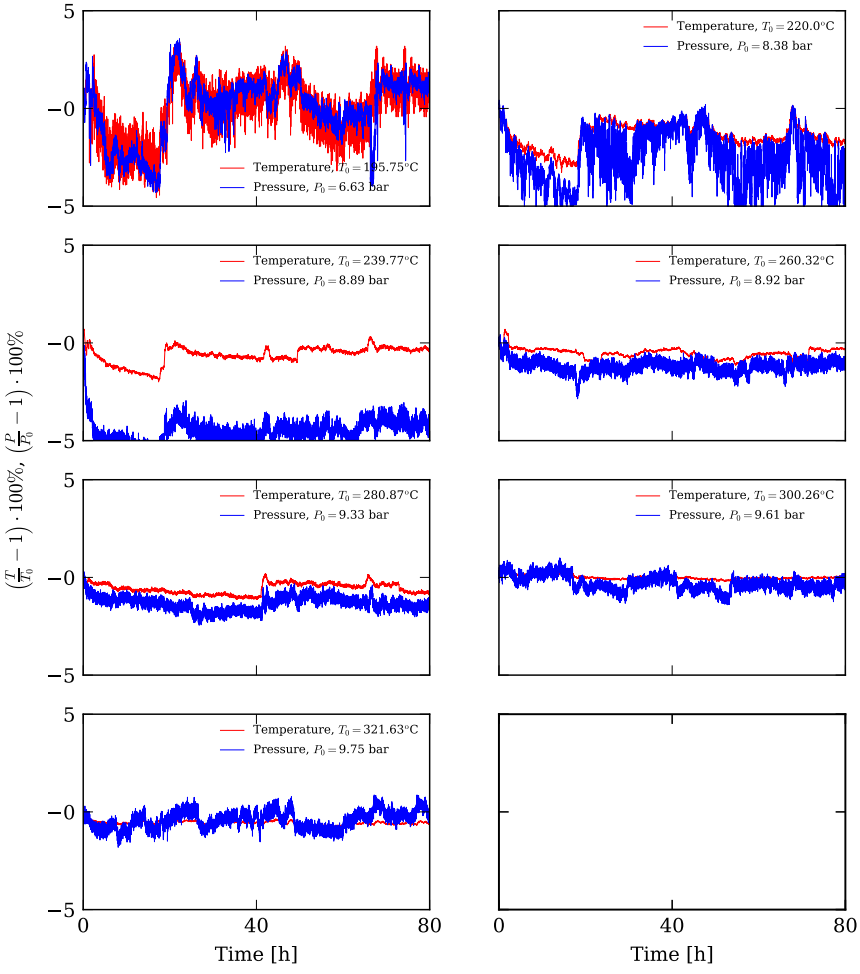

Figure 5.B.1: MM stress test.

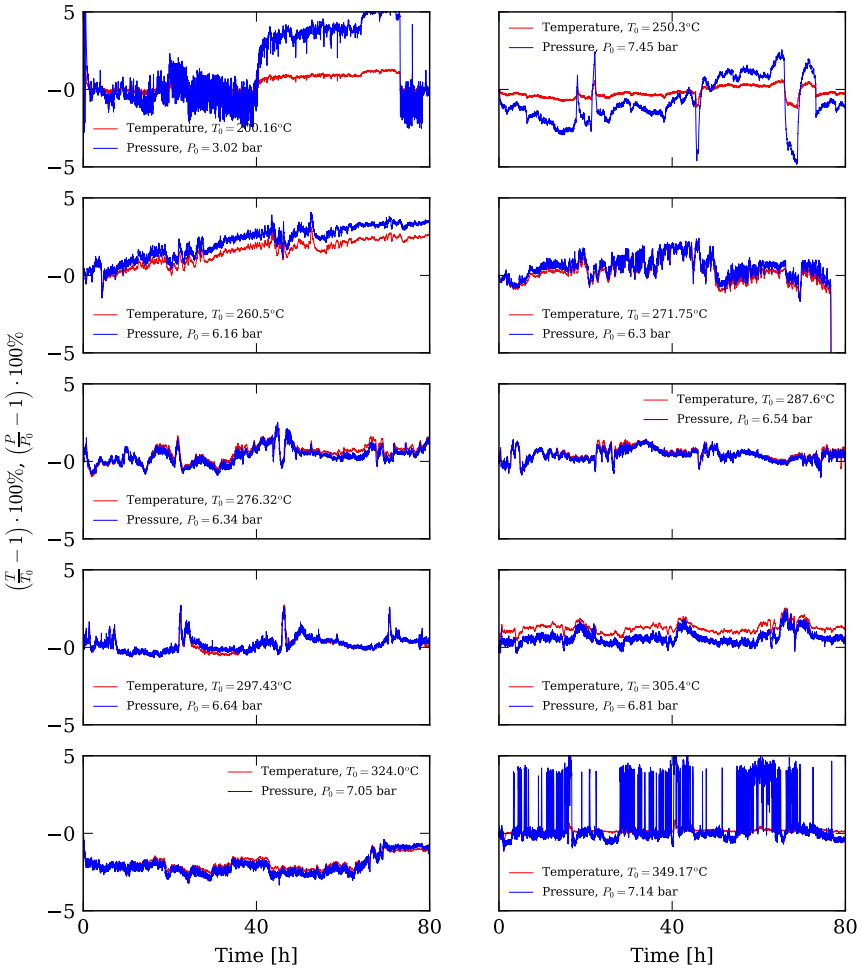

Figure 5.B.2: MDM stress test.

References

[1] G. Angelino and P. Colonna. “Multicomponent Working Fluids For Organic Rankine Cycles (ORCs)”. In: *Energy* 23.6 (1998), pp. 449–463. DOI: 10.1016/S0360-5442(98)00009-7.

[2] O. Badr, S. D. Probert, and P. W. O’Callaghan. “Selecting a working fluid for a Rankine-cycle engine”. In: *Appl. Energy* 21.1 (1985), pp. 1–42. DOI: 10.1016/0306-2619(85)90072-8.

[3] D. M. Ginosar, L. M. Petkovic, and D. P. Guillen. “Thermal Stability of Cyclopentane as an Organic Rankine Cycle Working Fluid”. In: *Energy & Fuels* 25.9 (2011), pp. 4138–4144. DOI: 10.1021/ef200639r.

[4] C. M. Invernizzi and D. Bonalumi. “5 - Thermal stability of organic fluids for Organic Rankine Cycle systems”. In: *Organic Rankine Cycle (ORC) Power Systems*. Ed. by E. Macchi and M. Astolfi. Woodhead Publishing, 2017, pp. 121–151. ISBN: 978-0-08-100510-1. DOI: 10.1016/B978-0-08-100510-1.00005-3.

[5] M. Preißinger and D. Brüggemann. “Thermal Stability of Hexamethyldisiloxane (MM) for High Temperature Organic Rankine Cycle (ORC)”. In: *Energies* 9.3 (2016).

[6] F. J. Fernández, M. M. Prieto, and I. Suárez. “Thermodynamic analysis of high - temperature regenerative organic Rankine cycles using siloxanes as working fluids”. In: *Energy* 36.8 (2011), pp. 5239–5249. DOI: 10.1016/j.energy.2011.06.028.

[7] P. Colonna, A. Guardone, and N. R. Nannan. “Siloxanes: A new class of candidate Bethe-Zel’dovich-Thompson fluids”. In: *Phys. Fluids* 19.8 (2007), p. 086102. DOI: 10.1063/1.2759533.

[8] P. Colonna, E. Casati, C. Trapp, T. Mathijssen, J. Larjola, T. Turunen-Saaresti, and A. Uusitalo. “Organic Rankine Cycle Power Systems: From the Concept to Current Technology, Applications, and an Outlook to the Future”. In: *J. Eng. Gas Turbines Power* 137.10 (2015). DOI: 10.1115/1.4029884.

[9] G. Angelino and C. Invernizzi. “Cyclic Methylsiloxanes as Working Fluids for Space Power Cycles”. In: *J. Sol. Energy Eng.* 115.3 (1993), pp. 130–137. DOI: https://dx.doi.org/10.1115/1.2930039.

[10] P. R. Dvornic. *Thermal Properties of Polysiloxanes*. Dordrecht: Springer Netherlands, 2000, pp. 185–212. ISBN: 978-94-011-3939-7. DOI: 10.1007/978-94-011-3939-7_7.

[11] P. Colonna and A. Guardone. “Molecular interpretation of nonclassical gas dynamics of dense vapors under the van der Waals model”. In: *Phys. Fluids* 18.5, 056101 (2006). DOI: https://dx.doi.org/10.1063/1.2196095.

[12] E. S. Blake, W. C. Hammann, J. W. Edwards, T. E. Reichard, and M. R. Ort. “Thermal Stability as a Function of Chemical Structure”. In: *J. Chem. Eng. Data* 6.1 (1961), pp. 87–98. DOI: 10.1021/je60009a020.

[13] K. R. Fisch and F. D. Verderame. “Automatic Recording Apparatus for Thermal Stability Determinations”. In: *J. Chem. Eng. Data* 6.1 (1961), pp. 131–134. DOI: 10.1021/je60009a027.

[14] I. B. Johns, E. A. McElhill, and J. O. Smith. “Thermal Stability of Organic Compounds”. In: *I&EC Product Research and Development* 1.1 (1962), pp. 2–6. DOI: 10.1021/i360001a001.

[15] I. B. Johns, E. A. McElhill, and J. O. Smith. “Thermal Stability of Some Organic Compounds”. In: *J. Chem. Eng. Data* 7.2 (1962), pp. 277–281. DOI: 10.1021/je60013a036.

[16] M. A. Fabuss, A. S. Borsanyi, B. M. Fabuss, and J. O. Smith. “Thermal Stability Studies of Pure Hydrocarbons in a High Pressure Isoteniscope”. In: *J. Chem. Eng. Data* 8.1 (1963), pp. 64–69. DOI: 10.1021/je60016a018.

[17] L. Calderazzi and P. Colonna. "Thermal stability of R-134a, R-141b, R-13I1, R-7146, R-125 associated with stainless steel as a containing material". In: *Int. J. Refrig* 20.6 (1997), pp. 381–389. DOI: 10.1016/S0140-7007(97)00043-1.

[18] M. Pasetti, C. M. Invernizzi, and P. Iora. "Thermal stability of working fluids for organic Rankine cycles: An improved survey method and experimental results for cyclopentane, isopentane and n-butane". In: *Appl. Therm. Eng.* 73.1 (2014), pp. 764–774. DOI: 10.1016/j.applthermaleng.2014.08.017.

[19] E. O. Doebelin. *Measurement Systems Application and Design*. 4th ed. Mcgraw-Hill College, 1989.

[20] E. W. Lemmon, I. H. Bell, M. L. Huber, and M. O. McLinden. *NIST Standard Reference Database 23: Reference Fluid Thermodynamic and Transport Properties - REFPROP, Version 10*. 2018.

[21] B. E. Poling, J. M. Prausnitz, and J. P. O'Connell. *The properties of gases and liquids*. 5th ed. New York: McGraw-Hill, 2000. ISBN: 9780070116825.

[22] S. J. Leon, Å. Björck, and W. Gander. "Gram-Schmidt orthogonalization: 100 years and more". In: *Numerical Linear Algebra with Applications* 20.3 (2013), pp. 492–532. DOI: 10.1002/nla.1839.

[23] D. C. Montgomery and G. C. Runger. *Applied Statistics and Probability for Engineers*. 6th ed. Wiley, 2013. Chap. 9.

[24] C. Hugh W. and S. W. Glenn. *Experimentation, Validation, and Uncertainty Analysis for Engineers*. 3rd ed. Wiley, 2009.

[25] *Wiley Registery of Mass Spectral Data 7th Edition*. 2000. URL: https://www.wiley.com.

CHAPTER 6

CONCLUSIONS AND OUTLOOK

6.1 Conclusions

This work presents original research in the field of non-ideal compressible fluid thermodynamics of mixtures. Three main topics are treated: (i) A fundamental research was conducted on the speed of sound of mixtures composed by linear siloxanes and perfluorocarbons, (ii) measurements on the bubble-point pressure for binary mixtures of linear siloxanes were carried out and new binary interaction parameters were determined for the Helmholtz energy equation of state for binary mixtures of linear siloxanes, (iii) a test setup was designed and commissioned to determine the thermal stability limit and decomposition products of pure fluids and mixtures. Results were obtained for the thermal stability and decomposition products of pure hexamethyldisiloxane (MM) and octamethyltrisiloxane (MDM). The general conclusions of the research topics in this work are summarized in the following.

The fundamental research on the speed of sound was performed on binary mixtures of linear siloxanes and perfluorocarbons. The polytropic van der Waals model with one fluid mixing rules was used for the exploration of qualitative effects of varying the mixture composition on the speed of sound and the relation to the pure component properties. This was done by a thorough analysis of the effect of attractive and repulsive forces, molecular complexity and critical properties of the mixtures on the speed of sound. Finally the Helmholtz energy equation of state for multicomponent fluids was used to verify the behavior of the speed of sound of binary mixtures of linear siloxanes and perfluorocarbons. The following results were obtained:

- Non-monotonic behavior of the speed of sound was observed upon varying the composition of the mixture, which leads to a maximum of the speed of sound for a mixture of the pure components. This non-monotonic behavior was caused by the interaction between the different components in the mixture and the direct influence on the speed of sound.
- In the case of linear siloxanes mixtures the reduced attractive and repulsive forces decrease with varying composition, following a parabolic behavior with minimums at different compositions. For mixtures of perfluorocarbons a non-monotonic increase with varying composition was observed for the attractive and repulsive forces, which demonstrates the effect of the interaction between the different components of the mixtures.
- The largest influence on the non-monotone behavior of the speed of sound is caused by the attractive force contribution. The attractive force contribution is directly related to the mixtures critical compressibility factor, which also exhibits a non-monotonic behavior upon mixing.
- The behavior of the mixture critical compressibility factor gives a direct indication of the mixture speed of sound behavior.

- The non-monotonic behavior of the speed of sound increases by increasing the difference in molecular complexity between the pure components of the mixture.
- The non-monotonic behavior of the speed of sound for binary mixture of linear siloxanes and perfluorocarbons was verified by the Helmholtz energy equation of state. The non-monotonic behavior of the critical compressibility factor was also observed using the Helmholtz energy equation of state.
- The effect of non-ideal mixing on the fundamental derivative of gas dynamics Γ was investigated for binary mixtures of linear siloxanes. Increasing non-monotonic behavior was also observed for Γ along the dew curve and the minimum value Γ_{min} in the vapor phase. The increasing non-monotonic behavior of Γ is similar to the behavior of the speed of sound and compressibility factor at the mixtures critical points. This shows that the change in critical properties upon mixing directly relates to Γ and the capability of the mixture to exhibit non-ideal fluid dynamic effects.

Measurements were performed to determine the bubble-point pressures for three binary mixtures of MM with MDM, MD_2M, and MD_3M. For each mixture, three compositions were measured with a MM presence in all mixtures of approximately 25 mol%, 50 mol%, and 75 mol% of the total mixture. The bubble-point pressures were measured at temperatures ranging from 270 K to 380 K in steps of 5 K or 10 K depending on the mixtures. The pressure ranged from 0.46 kPa to 97.45 kPa for all samples. For each mixture combination new binary interaction parameters were fitted for the multi-fluid Helmholtz energy model using the obtained bubble-point pressure data. The measurements and modeling were carried out at the National Institute of Standards and Technology. The following results were obtained:

- Large uncertainties were observed for the lowest temperatures (below 320 K). These large uncertainties were mostly caused by the effect of non-condensable gases.
- The effects of non-condensable gases on the bubble-point pressures were analyzed. Experimental results between mixtures degassed for three and fifteen times were compared. The non-condensable gases were estimated by fitting the nitrogen content of a ternary mixture with nitrogen to the data and a decrease by a factor of approximately 100 between degassing three and fifteen times was observed from the order 100 ppm to 1 ppm. This shows the large impact of small amount of non-condensable gas impurities on the bubble-point pressure at low temperatures, which can affect the thermodynamic properties of the fluid and consequently influence the predicted efficiency and performance of ORCs as well as other processes.
- New binary interaction parameters were fitted for multi-fluid Helmholtz energy model. For the fitting the data were weighed by the relative uncertainty, ensur-

ing that the data points with large uncertainties contribute less to the overall fitting of the binary interaction parameters.

- At higher temperatures (above 320 K) the new binary mixtures represent the experimental bubble-point pressures within 10% deviation. In comparison, deviations where previously estimated binary interaction parameters were used, were in the order of 20%. For temperatures below 320 K the deviations overall increase, which is due to the weighing based on the relative uncertainty.
- The affect of the new binary interaction parameters on the speed of sound, compressibility factor, and fundamental derivative of gas dynamics Γ was investigated. The new binary interaction parameters increase the non-monotonic behavior of the speed of sound and compressibility factor at the critical point as well as the minimum value of Γ.
- The new binary interaction parameters decrease the minimum value of Γ for binary mixtures with higher concentrations of MDM, MD_2M, and MD_3M. This leads to an increase of the region for which the mixtures can exhibit non-ideal fluid dynamic effects. At higher concentration of MM within the binary mixtures, the minimum value of Γ increases with the new binary interaction parameters.

An experimental test-rig was designed and commissioned for the determination of the thermal stability limit and decomposition productions of pure fluids and mixtures. The novelty of this setup is the capability to determine the decomposition products of the liquid and vapor phase using chemical analysis. Results were obtained for the pure fluids of MM and MDM.

- The thermal stability analysis was performed by monitoring pressure deviations during the thermal stress test, deviation of stressed fluid vapor pressure from reference fluid vapor pressure, and finally chemical analysis of the stressed fluid liquid and vapor phase.
- For MM no pressure deviations indicating thermal decomposition were observed during the thermal stress test. Nevertheless, results of the deviation of the stressed fluid vapor pressure from the reference fluid showed that at 240 °C and higher appreciable decomposition of MM occurs. The decomposition was verified by chemical analysis although the decomposition products are very limited. Interesting was the formation of volatile gases in the vapor phase of the decomposed MM.
- Similar results were obtained for MDM, again no pressure deviations during the thermal stress test showed signs of thermal decomposition. However, deviations of the stressed fluid vapor pressure from the reference fluid showed appreciable decomposition of MDM at 250 °C and stabilizes occurred at 260 °C and higher. The chemical analysis of MDM showed limited decomposition,

but also for MDM volatile gases were formed as decomposition products. The decomposition products for MDM were similar to the products of MM due to their similar structure and are constructed of the same atoms.

- The thermal stability limit for both MM and MDM is around 250 °C . The decomposition products were limited, but the formation of other linear siloxanes as decomposition products was observed. Finally the formation of volatile components can have a large influence on the fluid properties due to the low vapor pressure of MM and MDM. When the fluid is stressed for a longer period more volatile gases form and the effect of these gases can have a larger impact on the behavior of the fluid.
- The thermal stability temperature on the fundamental derivative of gas dynamics is assessed for MM and MDM. For both fluids, most of the non-ideal fluid dynamic effects region is above the decomposition temperature, therefore the fluids are only capable of exhibiting non-ideal fluid dynamic effects at the lower temperatures, without risking decomposition and affecting the thermodynamic properties of the fluid.

6.2 Outlook

The contribution of this work leads to a better knowledge of the non-ideal thermodynamic behavior of mixtures in the non-ideal compressible-fluid region and development of accurate thermodynamic models. This new knowledge is of paramount importance for the use of mixtures within experimental and industrial applications. The motivation for this research was to gain a better understanding of the behavior of mixtures in the non-ideal compressible-fluid region. These fluids, featuring high molecular complexity, were investigated because of their ability to exhibit non-ideal and non-classical gasdynamic phenomena in the non-ideal compressible-fluid region, close to liquid-vapor saturation curve. Another contribution was the better understanding and determination of the thermal stability limit and decomposition products of molecular complex fluids. To further the development of the use and understanding of molecular complex mixtures, research in the near future of the non-ideal thermodynamic region should be aimed in the following directions.

The research on the speed of sound behavior of mixtures can be used as basis for further research on the non-ideal compressible thermodynamic behavior of mixtures. A detailed research should be conducted on the notable difference in behavior of the repulsive forces as well as critical pressure between linear siloxane and perfluorocarbon binary mixtures. Also, different behavior is observed for the critical pressure of binary mixtures of linear siloxanes between the van der Waals model and Helmholtz energy model and should be investigated and entail a larger range of binary mixtures of various fluid families. Furthermore, for a better and more generalized understand-

ing of the mixture behavior, a more detailed analyses should be conducted based on molecular models and the involved molecular interaction (e.g. electrostatic interactions). This detailed analysis on microscopic properties can lead to a more general theory on the interaction of different molecules in mixtures.

Future research can also involve different mixture combinations to investigate in depth the speed of sound behavior as well as the behavior of the mixtures critical properties and their relations to the speed of sound. The investigation of highly non-ideal mixtures, composed of complex organic compounds (e.g. cyclic siloxanes, perfluorocarbons, and heavy hydrocarbons), is of great interest. As is demonstrated in this work, components of the same family show an increase of the speed of sound upon mixing. Mixing components of different families can possibly decrease the speed of sound and enhance non-ideal gas dynamic behavior.

Furthermore, a more in depth research on the fundamental derivative of gas dynamics Γ is of great interest to investigate the non-ideal and non-classical gas dynamic behavior of (highly non-ideal) mixtures. Finally, computational fluid dynamics simulations with mixtures using compressible fluid dynamic models and state-of-the-art multicomponent thermodynamic models is a naturally continuation in the research of non-ideal compressible fluid dynamics of mixtures.

A next step forward for the development of accurate thermodynamic models of linear siloxane mixtures are measurements at higher temperatures up to the thermal stability limit of the fluids. At higher temperatures the effect of non-condensable gases will be less and more accurate measurements can be obtained. Furthermore, measuring the bubble-point pressure directly within the equilibrium cell yields a great improvement in accuracy, which will take out the possible temperature difference between the pressure transducer and the equilibrium cell now present in the setup. Carrying out pressure measurements on the liquid phase additionally, within the equilibrium cell will also improve the measurement, as the pressure of the liquid and vapor phase can be compared to be sure the system is at equilibrium conditions. Measurements of other thermodynamic properties (e.g. density, speed of sound, specific heat) will greatly contribute to more accurate thermodynamic models. Speed of sound measurements can be used to verify the non-monotonic speed of sound behavior of binary mixtures observed in the fundamental research on the speed of sound. The results obtained in this research can also be used to improve other thermodynamic models, e.g. Peng-Robinson, Soave-Redlich-Kwong, and PCP-SAFT. Furthermore, research can be conducted to obtain an indication which thermodynamic model and mixing rule are most suitable for the calculation of linear siloxane mixtures.

Investigation of the effect of air on low vapor pressure fluids like siloxanes is of paramount importance. As is presented in this work, a small amount of non-condensable gases can already have a large influence on the bubble-point pressure of these mixtures especially at low temperatures. A more detailed research should be conducted on the effect of non-condensable gases on the prediction of the perfor-

mance and efficiency of ORCs using these low vapor pressure fluids. Non condensable gases can also affect the fundamental derivative of gas dynamics and changing the non-ideal gas dynamic behavior of pure fluids and mixtures. A next step is the determination of the solubility of non-condensable gases, specifically air, in linear siloxanes and other high molecularly complex fluids to determine the maximum effect these gases can have on the properties of the fluids.

To conclude, for the investigation and understanding of non-ideal compressible fluid thermodynamics, future research should be devoted to the improvement of thermodynamic models for pure fluids and (highly non-ideal) mixtures of complex organic compounds.

The experimental setup for thermal stability measurements is the basis for further measurements and research on the thermal stability limit and decomposition products of pure fluids and mixtures. The setup will be updated for future measurements to ensure a more stable temperature during the stress test and vapor pressure measurements. When the update is finished, research will entail the measurement of binary mixtures of linear siloxanes and other organic fluids. The measurements on mixtures will be conducted to prove the possible higher thermal stability temperature of linear siloxane mixtures than their pure components. This is due to the possible redistribution process occurring at high temperature, where more complex molecules decompose into simpler molecules, which then recombine again into the more complex molecule. This redistribution process can also be proven by the chemical analysis of the liquid and the vapor phase.

Furthermore, other effects, which can influence the thermal stability, can be investigated. Effects can include, the time span a fluid is stressed, the pressure at which the fluid is stressed, and impurities within the fluid (e.g. water, lubrications, and other contaminations within power cycles). Finally, the effect of the thermal stability limit and decomposition products on an ORC or other industrial or experimental process employing organic fluids should be determined. Because the decomposition products are determined, this knowledge can be used to investigate the change in thermodynamic properties of the fluid and the effect on the process.

NOMENCLATURE

Roman symbols

f	fugacity
A	Helmholtz energy
c_p	isobaric specific heat
c_v	isochoric specific heat
C	total number of components
E	internal energy
G	molar Gibbs energy
H	enthalpy
M	molecular weight
N	number of active degrees of freedom
P	pressure
R_s	specific gas constant
R	universal gas constant
S	entropy
T	temperature
V	volume
Y	reducing parameter
Z	compressibility factor
a	attractive fluid dependent parameter
b	repulsive fluid dependent parameter
c	speed of sound
$\mathfrak{L}$	critical condition determinant
$\mathfrak{M}$	critical condition determinant
e_S	weighted error vector
ΔH_v	enthalpy of evaporization
ΔZ_v	difference in compressibility factor between saturated liquid and vapor
e	specific internal energy

h	height vapor phase
i_C	confidence index
k_{ij}	binary interaction parameter
k	coverage factor
l_{ij}	binary interaction parameter
m	mass
n	total number of moles
$\mathrm{p_i}$	confidence level
q	vapor quality
s	specific entropy
t	height triangular portion
u	uncertainty
v	specific volume
x	liquid phase molar composition
y	vapor phase molar composition
z	molar composition

Greek symbols

β	binary interaction parameter Helmholtz energy model
ΔY	difference in property Y
F_{ij}	fitting factor departure function Helmholtz energy model
γ	binary interaction parameter Helmholtz energy model
Γ	fundamental derivative of gas dynamics
α^{o}	ideal part dimensionless Helmholtz energy
α^{r}	residual part dimensionless Helmholtz energy
α	dimensionless Helmholtz energy
$\tilde{\alpha}$	coefficients Gram-Schmidt orthogonalization
δ	reduced mixture density
μ	chemical potential
ω	acentric factor
ρ	density
σ_0^2	variance of the errors
σ	standard deviation
τ	reduced mixture temperature
θ	angle
ε	void fraction

Sub- and superscripts

0	initial value
FS	full scale
amb	ambient conditions
att	attractive force
calc	calculated property
c	critical property
exp	experimental property
o	ideal gas state
ig	ideal gas
i, j, k	component indices
ins	instrument
lim	thermal stability limit
liq	saturated liquid property
l	liquid phase
max	maximum value
min	minimum value
mod	model
mol	molar property
m	mixture property
ref	reference property
rel	relative property
rep	repulsive force
r	reduced property
stress	stressed property
vap	saturated vapor property
v	vapor phase

Abbriviations

Ar	Argon
JI	Boyle curve
BZT	Bethe-Zel'dovich-Thompson fluid
CFD	computational fluid dynamics
CO_2	carbon dioxide
CREA	Compressible-fluid dynamics for Renewable Energy Applications
FID	flame ionization detector
GC	gas chromatography

HEOS	Helmholtz energy equation of state
HRGC	high resolution gas chromatography
He	helium
ID	Ideal curve
JI	Joule-inversion curve
JT	Joule-Thomson curve
MD_2M	decamethyltetrasiloxane
MD_3M	dodecamethylpentasiloxane
MD_4M	tetradecamethylhexasiloxane
MD_5M	hexadecamethylheptasiloxane
MD_6M	octadecamethyloctasiloxane
MDM	octamethyltrisiloxane
MM	hexamethyldisiloxane
MS	mass spectrometry
N_2	nitrogen
NIST	National Institute of Standard and Technology
ORC	organic Rankine cycle
PID	Proportional-Integral-Derivative
PTFE	polytetrafloroethylene
PT	pressure transducer
PV	pneumatic valve
RTD	resistance temperature detector
SPRT	standard platinum resistance thermometer
TCD	thermal conductivity detectors
TROVA	Test Rig for Organic Vapors
VLE	vapor-liquid equilibrium
VdW-EOS	van der Waals equation of state

LIST OF FIGURES

LIST OF TABLES

ACKNOWLEDGMENTS

The realization of this dissertation is partly due to the enthusiastic dedication and help of many. The research described in this dissertation has been performed at the group of the Compressible fluid dynamic for Renewable Energy Applications laboratory (CREA) and the faculty of Aerospace Science and Technology at the Politecnico di Milano, Italy.

I first want to deeply thank Prof. Alberto Guardone whom I am very grateful for giving me the opportunity to start my doctoral dissertation and supervised me throughout my entire Ph.D. research. Without him, I would not have had the opportunity to follow this path and this thesis would not have become as diverse and comprehensive as it has. I feel myself very lucky for having him as my supervisor, he gave me the freedom to investigate the academic topics which interested me the most and guidance throughout the years. Finally, I am grateful for his enthusiasm, openness, and full time support in good and bad times.

Of course, many other people have contributed to this thesis. I would like to thank my co-supervisor Prof. Andrea Spinelli for his support and guidance during this research. His expertise and great knowledge in performing experiments was of invaluable value. I am also grateful to Chiara Landolina, who assisted me in building and performing experiments on the thermal stability setup. In addition I want to thank the University of Brescia, Prof. Costante Invernizzi, Prof. Paolo Iora, Modestino Savoia, and Prof. Luca Lietti for their support on making the thermal stability setup a reality. Furthermore, I would like to thank Teus van der Stelt for his continuous assistance and interest in my work. And finally Prof. Piero Colonna for introducing me to Prof. Alberto Guardone as a potential Ph.D. candidate.

Many thanks to all my colleagues and friends at the CREA laboratory and the Politecnico di Milano for their support and assistance during my Ph.D. research as well as their contribution to creating a welcoming and sociable working environment. I really appreciate the moments we shared together and getting to know their work and life experiences as well as the Italian culture. Furthermore, a big thanks also goes to all my friends and floorball team who I got to know outside of the University for a wonderful time and experience in Milan and Italy.

I also have had the opportunity to extend my research to the National Institute of Standards and Technology (NIST) in Boulder, United States. For this my deepest

thanks to my co-supervisor Elisabeth Mansfield and Ian Bell for their support, hospitality and discussions on the bubble-point measurements of linear siloxanes mixtures (which were not the most easy fluids to handle). Also many thanks to all other people at NIST and in Boulder for their support and making my stay possible. For me it has been a unique opportunity and experience to work with top researchers in the field of thermophysical properties and to experience the beautiful nature Colorado has to offer.

I acknowledge the European Research Council for its financial support that enabled this research project under the ERC Consolidator Grant 2013, project NSHOCK 617603.

I want to express my gratitude to the examination committee. I appreciate their time devoted to reviewing and evaluating this dissertation and their interest in my work.

I especially want to thank my mother, brother, sister, and family for their continuous and full support during this work and during an incredible difficult period in our lives, which will never be the same as when I started this work. Furthermore, I want to deeply thank all my close friends and girlfriend Esther for their continuous support and being a listening ear.

Finally, my deepest gratitude to my father for everything he did and was for me and anybody else in his life. There are no words to express my gratitude, admiration, and what he meant to me.

Luuc Keulen
Milan, 2018